A Comparison of the Nickel and the conventional geothermometers with respect to the Jagersfontein and the Matsoku kimberlite peridotite xenoliths

Sipho W. Mofokeng

A Comparison of the Nickel and the conventional geothermometers with respect to the Jagersfontein and the Matsoku kimberlite peridotite xenoliths

Sipho W. Mofokeng

Dissertation submitted in fulfilment of the requirements for degree of
Master of Science at the University of Cape Town

Department of Geological Sciences
December 1998

Like a comet,
blazing against
the evening sky

Gone to soon

Like a rainbow,
fading in the twinkling
of an eye

Gone too soon

Like a sunset,
dying with the rising
of the moon

Gone too soon, gone too soon

So long Mbuyiselo
(15/08/1970 – 06/02/1998)

Acknowledgements

I am indebted to my supervisors, Prof. AP le Roux and Dr M Tredoux for giving me the opportunity to do this project under their able scientific guidance. I am thankful to Prof. JJ Gurney and Dr DR Bell for sharing their broad knowledge in mantle petrology and geothermobarometry.

I also would like to thank the following people for assistance in various stages of this study:
<u>*At de Beers Geology*</u>:
Management for approving my study-leave and bursary.
Mr EMW Skinner for the major role he played in the approval of the bursary and study-leave.
Dr JV Robey for administering the bursary and for his willingness to assist at anytime.
Management and colleagues for moral support and 'checking up' on me whenever in Cape Town.
<u>*At UCT (Geological Sciences)*</u>:
David Wilson for the many, many thin sections and grain mounts required for this study.
Dr A Späth and *Dick Rickard* for assistance with, respectively, LA-ICP-MS and electron microprobe analyses.
The Kimberlite Research Group members for scientific discussions and assistance in finding useful information and references.
The *support, technical and secretarial staff* for their help in many, many ways.
<u>*At the National Accelerator Centre*</u>:
Dr W Przybylowicz for his able guidance during PIXE analyses.
The technical staff for their efficient technical support during PIXE analyses.
<u>*At the Carnegie Institute of Washington*</u>:
Dr R Carlson for the role he played in organising my visit to Carnegie and in making the stay at Carnegie and in Washington, D.C. a very pleasant one.
Drs E Hauri and *J Wang* for their guidance during the ion microprobe analysis.
Dr FR Boyd for discussions on geothermobarometry and useful papers.
The many others at CIW for their hospitality and scrumptious lunches, and for making my stay easy at Carnegie and Washington, D.C.

Last but definitely not least:
I am grateful to Neo for moral support and encouragement, all the way and always.
I thank my parents, Mtutu and the rest of our family for believing in me, for prayers throughout my education and for supporting me in whatever I undertake to do in life.
Many thanks to Fele (Dr Khoele), Mbongeni, Maanda, Benford, Buhle for being my friends and for encouraging me all the way.

Ke a Leboga.

Abstract

The accuracy of the experimental (Canil, 1994; T-Canil) and the empirical (Ryan *et al.*, 1996; T-Ryan) calibrations of the Ni geothermometer has been evaluated on two suites of geochemically and geothermobarometrically well characterised mantle xenoliths from Matsoku and Jagersfontein by comparison to the more commonly used conventional geothermometers.

The two published calibrations of the Ni geothermometer are in agreement to within ±50°C in the temperature range of ~900°C to 1200°C. Outside this temperature range, the two calibrations differ by between 75 and 150°C. The importance of the Ni geothermometer in diamond exploration and the studies of the mantle makes the resolution of this discrepancy very important.

In addition to issues of calibration, errors in the determination of trace levels of Ni abundances in garnets may affect the accuracy of the Ni geothermometer. A 'reliable' Ni in garnet dataset was, therefore, required to minimise errors associated with Ni compositions used in temperature determination by Ni geothermometry. Thus, Ni compositions of garnets determined by PIXE, LA-ICP-MS and SIMS were compared to select the most 'reliable' dataset. Four matrix-matched secondary garnet standards were developed for the cross-checking and testing of the accuracy of data. The standards were developed by multi-method analyses, which included PIXE (using both the GeoPIXE and GUPIX software programmes for data reduction), LA-ICP-MS and solution ICP-MS. PIXE and LA-ICP-MS data were found to agree to within their 2σ errors of, respectively, 2 to 10% and 4 to 12% for a concentration range of ~15 to 112 ppm Ni. However, PIXE analyses were found to be superior in terms of smaller beam width, allowing several repeat analyses, and analysis of small and altered garnets thereby producing a relatively larger dataset.

Available conventional geothermobarometers cannot all be accurate, since application of different geothermobarometers on the same rock can give significantly different results (Finnerty and Boyd, 1984). Therefore, prior to comparison with Ni geothermometry, conventional geothermometers were assessed by literature review

and evaluation of temperature estimates derived on the samples used in this study. The pyroxene solvus geothermometer of Brey and Köhler (1990), T-BK2px, was considered the most appropriate for the determination of pressure and temperature conditions of equilibration of mantle peridotite xenoliths. This geothermometer is immune to the Fe^{3+} uncertainty which, when unaccounted for, affects the accuracy of the Fe^{2+}–Mg exchange geothermometers. Moreover, T-BK2px is based on the experiments of Brey *et al.* (1990), carried out at pressures (10 to 60 kb), temperatures (900 to 1400^{0}C) and compositions ($CaO\text{-}FeO\text{-}MgO\text{-}Al_2O_3\text{-}SiO_2\text{-}Cr_3O_2\text{-}Na_2O$ system) that are applicable to natural peridotites. Other pyroxene solvus geothermometers [those of Bertrand and Mercier (1985), and of Finnerty and Boyd (1987)] generally reproduced the temperature estimates derived using T-BK2px to within $\pm 75^{0}$C. At high temperatures ($>1200^{0}$C), Fe^{2+}–Mg exchange geothermometers underestimated these temperature estimates by between 100 to 200^{0}C when significant amounts of Fe^{3+} in garnets are neglected.

The empirical calibration of the Ni geothermometer generally reproduced temperatures derived using T-BK2px to within $\pm 75^{0}$C. In contrast, the experimental calibration underestimated these temperatures at high temperatures and overestimated the temperatures at low temperatures.

The palaeogeotherm of the mantle traversed by the two kimberlites under study, derived using the geothermobarometer combination of Brey and Köhler (1990) is consistent with an 'uninflected' ~43mW/m^2 continental geotherm. The geothermobarometer combination of Ryan *et al.* (1996), i.e. a combination of the empirical Ni geothermometer and the chrome barometer of Ryan *et al.* (1996), reproduced this geotherm to within ~2mW/m^2.

The main conclusion of this study is that, based on application of the Ni geothermometers on the present dataset, temperatures derived using T-Ryan are as accurate as the temperatures derived using the more commonly used conventional geothermometers.

List of Figures

Chapter 2:

Chapter 3:

Chapter 4:

Chapter 6:

Chapter 7:

List of Plates

Chapter 2:

List of Tables

Chapter 2:

Chapter 3:

Chapter 4:

Chapter 6:

List of Appendices

Table of Contents

Chapter 1

1. Introduction

1.1 Thermal Structure of the Mantle

The temperature of the Earth's mantle is a prime control of magmatic and tectonic processes. For example. high temperatures in the mantle would cause high degrees of partial melting and would enhance mantle convection. Convection drives upwelling at mid-ocean ridges and hence controls sea floor spreading. Thus, mantle evolution and petrogenesis studies largely involve thermal evolution studies of the mantle. In addition to present day heat loss and heat production rates, the ancient crustal thermal record preserved in metamorphic rocks and lithospheric mantle pressure and temperature (P,T) data recorded in mantle xenoliths (Boyd, 1973) and in diamond inclusions (Richardson *et al.*, 1984), places constraints on these studies.

The rate at which heat leaves the Earth's surface, the surface heat flow (q_s), is expressed in mW/m^2 as the product of the average thermal conductivity (k) and the geothermal gradient, the variation of temperature (T) with depth (z):

$$q_s = k \cdot (\partial T/\partial z)$$

In general, for shallow crustal levels, $\partial T/\partial z$ data can be obtained by making direct temperature measurements at known depth in the mineral exploration drill holes. Thermal conductivity is measured either *in situ* or measured in laboratory on rock samples collected from the field (Stein, 1995). The heat flow in the continental lithosphere depends on three main factors:

i) heat production in the crust, derived from the radioactive decay of U, Th and K;

ii) tectonic setting, convective transport of heat from magmas and fluids entering lithosphere during orogenic events; and

iii) heat flux from the lower mantle by advection, and by conduction in the lithospheric mantle.

By comparison to oceans the heat flow is low in continents and is particularly low in cratonic areas. Moreover, global compilations of surface heat flow data show that stable Archaean cratons have a lower mean surface heat flow (41±12 mW/m^2) relative to the stable Proterozoic crust (55±17 mW/m^2) along the boundaries of the cratons (Rudnick *et al.*, 1998). Two reasons have been suggested for these differences in heat flow:

a) lower heat production in the Archaean cratons relative to the surrounding younger terrains.

b) the relatively greater thickness of the lithosphere in cratonic areas serves as a shield against heat from the sublithosphere reaching the surface.

The pressures and temperatures of equilibration of mantle xenoliths are influencing factors of the mineral phases present and their chemical composition. In reverse, the composition of coexisting mineral phases can give temperatures and pressures of equilibration of garnet and spinel peridotites occurring as xenoliths in kimberlites and other volcanic rocks. This has become an important tool to gain information about physical and chemical properties, and processes of the upper mantle, since the pioneering study of Boyd (1973).

P,T estimates of the mantle xenoliths and of diamond inclusions provide valuable information about the thermal structure of the mantle through geological time. The P,T estimates of mantle xenoliths brought to surface by Cretaceous kimberlites may be considered to represent the present day (or recent) thermal conditions of the mantle. Studies by Richardson *et al.* (1984) have shown that diamond inclusions are Archaean in age and thus indicate the presence of a greater than 200 km thick cratonic lithosphere (Boyd *et al.*, 1985) in the Archaean. In addition, P,T estimates of diamond inclusion pairs are consistent with the cratonic geotherm (40 mW/m^2) of Pollack and Chapman (1977) (Boyd *et al.*, 1985), similarly to the P,T estimates of coarse peridotites (Boyd, 1973). Similar results were found by Danchin and Boyd (1976) using mantle xenoliths from the 1.3 Ga Premier kimberlite and by Ganguly and Bhattacharya (1987) using mantle xenoliths from the Indian Proterozoic kimberlites. This implies that the craton from which these xenoliths are derived have maintained an essentially constant thermal structure since the Archaean.

Boyd and Gurney (1986) used diamond inclusion, and mantle xenocryst and xenolith data to characterise the structure of the portion of the Kaapvaal craton that lies within the mantle. These authors suggested that the craton has an ultramafic root that is strongly depleted in basaltic components. They also noted that this root extended to depths of ~190km, was formed earlier than 3 billion years ago (Richardson *et al.*, 1984) and, at the time, had ambient temperatures of 900 to 1200^{0}C. The restriction of diamond occurrence to old stable lithosphere beneath cratons imply the mantle roots provided suitable physical and chemical conditions for diamond formation and preservation (Boyd and Gurney, 1986; Helmstaedt and Gurney, 1995). The lack of diamonds in kimberlites intruded in areas that are off-craton indicate the absence of mantle roots beneath the younger mobile belts surrounding Archaean cratons during kimberlite emplacement.

Helmstaedt and Gurney (1995) noted that large-scale target area selection during the exploration of primary diamondiferous deposits should concentrate on regions in which these mantle roots existed during the kimberlite or lamproite intrusion. Detection of the mantle roots can be done geophysically by seismic surveys. However, seismic surveys detect the present state of the mantle and thus kimberlites on cratons without a geophysical signature of mantle roots may be diamondiferous if they sampled a mantle root prior to its destruction by mantle processes, e.g., mantle plumes (Helmstaedt and Gurney, 1995). A method that is more 'reliable', in terms of detection of the existence of mantle roots during kimberlite emplacement, is that involving studies of minerals occurring as xenocrysts ("indicator minerals") and xenoliths in kimberlites. The P,T estimates derived from the chemistry of coexisting mineral phases are plotted in P,T space to produce palaeogeotherms of the mantle sampled by the kimberlite.

The position and shape of these palaeogeotherms are the most important factors that give an indication of the diamond potential of a kimberlite or lamproite. Geotherms with high heat flows (e.g. in young terrains off-craton) do not enter the diamond stability field and therefore represent barren lithospheres (Morgan, 1995; Helmstaedt and Gurney, 1995). Such geotherms are thus unprospective for diamonds (Morgan, 1995; Nixon, 1995). It is areas with cool, typical 'cratonic' (35-40 mW/m^2) geotherms that are highly prospective. This is because such geotherms enter the diamond stability field at shallower depths and indicate that the lithosphere has a high potential for containing diamonds (Nixon, 1995, Griffin and Ryan, 1995).

1.2 Recent Advances in Geothermobarometry

Geothermometers and geobarometers are formulated from comparisons of geochemical data of mantle minerals with chemical data from experiments on synthetic and natural systems at known pressures and temperatures. These geothermometers and geobarometers have several limitations which include extrapolations to temperatures and pressures that are beyond the experimental conditions, extrapolations from simple synthetic systems to natural multi-component systems, disequilibrium in some or all of the phases, and different blocking temperatures for simultaneously solved barometers and thermometers. These and other limitations are discussed in more detail in section 5.4.1. The most recent study which has attempted to circumvent most of these problems is that of Brey *et al.* (1990) who carried out experiments at physical (10 to 60 kb and 900 to 1400^{0}C) and chemical conditions that are similar to those in natural four-phase peridotites.

For a long time, after the pioneering work of Boyd (1973), P,T estimates have been determined using geothermobarometer pairs which utilise major element chemistry of coexisting mineral phases occurring in equilibrium in the xenoliths. However, particularly in the early stages of diamond exploration, it is quite rare to find mantle mineral phases in coexistence. Normally these mantle minerals are found as disaggregated grains in heavy mineral concentrates recovered from stream sediment and soil samples. The recent development (Griffin *et al.*, 1989; Ryan *et al.*, 1996) and the experimental calibration (Canil, 1994) of the Ni geothermometer and the development of the chrome barometer (Ryan *et al.*, 1996) have created a potential to calculate

Chapter 2

2. Sample Descriptions

2.1 Locality

The sample suite from the Jagersfontein kimberlite pipe shows a wide range of temperatures and pressures of equilibration based on major element geothermobarometry (Winterburn, 1987; Hops, 1989). The sample suite from the Matsoku kimberlite pipe comprises mantle xenolith types equilibrated at essentially constant temperatures and pressures (Winterburn, 1987).

The locality of these two kimberlite pipes is shown in Fig. 2.1. Jagersfontein (29^{0}46'S, 25^{0}28'E) is a Group 1 (Smith, 1983) diamondiferous kimberlite, situated ~150 km south-east of Kimberley in the Free State province of the Republic of South Africa. The pipe intruded close to the southern edge of the Kaapvaal craton into the Beaufort Group (Permian to Triassic) of the Karoo Supergroup. The Jagersfontein kimberlite has a U-Pb whole rock age of 89 ± 4 Ma (Kramers and Smith, 1983) and a Rb-Sr phlogopite and whole rock age of 85.6 ± 1.0 Ma (Smith *et al.*, 1985a).

The Matsoku kimberlite (29^{0}05' S, 28^{0}44' E) is also a Group 1 diamondiferous kimberlite, located in northern Lesotho, between the Lipitsaneng and Matsoku rivers. Matsoku is located close to the southern edge of the Kaapvaal craton, and intruded into the 180 Ma Drakensberg Volcanic Suite. There is no age published for the Matsoku kimberlite; however, it is assumed to be about 90 Ma by association with the nearby Letseng, Kao, Mothae and Thaba Putsoa kimberlite (Smith; Gurney, *pers. comm.*).

equilibrium P,T conditions from single peridotite garnet grains. Ni geothermometry is based on the temperature dependency of the partitioning of Ni between garnet and coexisting olivine, with garnet accepting more Ni into its structure as temperature increases. Cr barometry is based on the Cr solubility in orthopyroxene coexisting with garnet. However, the composition of the orthopyroxene is calculated from the composition of a garnet phase, assumed to have coexisted with the orthopyroxene.

Using Ni geothermometry, equilibration temperatures can be derived from single garnets and can be plotted onto a known local geotherm to determine the pressure of equilibration of the garnets. Palaeogeotherms can also be derived using pressure and temperature estimates derived using a combination of Ni geothermometry and Cr barometry where there is a lack of multi-phase xenoliths and the local geotherm is unknown.

However, the experimental and empirical calibrations of the Ni geothermometer yield different results. Outside the Ni concentration range of ~38 to 90 ppm (corresponding to 900 to 1200^0C) the two calibrations differ by between 75 and 150^0C. The importance of Ni geothermometry in diamond exploration and mantle studies in the determination of equilibration P, T conditions of dissagregated mantle samples makes the resolution of the discrepancy between the empirical and the experimental Ni geothermometers a high priority, with immediate applications. A particular importance in diamond exploration is in providing early information on the likelihood of the presence of deep mantle in the exploration samples, indicating possible presence of diamond.

1.3 Analytical Techniques

In addition to the issues of calibration, the accuracy of the Ni geothermometers is also strongly dependent on the quality of Ni data. Continual improvement of analytical techniques have enabled geochemists to analyse for trace elements in rocks and minerals at greater accuracy, with better precision and to lower detection levels, bringing new insights into geological processes, including those that are related to diamond formation and preservation, than was previously possible. In addition to the use of trace Ni contents in Cr pyrope garnets in geothermobarometry, other trace elements have also been used in mantle studies. For example, variations of trace quantities of Y, Ga and Cr in peridotite garnets have been interpreted as due to degrees mantle depletion through partial melting, whereas enrichment in Zr, Y and Ti has been interpreted to provide clues to metasomatic processes such as infiltration of asthenospheric melts (Griffin *et al.*, 1995).

The use of these elements in mantle studies and diamond exploration (Griffin and Ryan, 1995) requires high quality analyses, making the comparison and evaluation of analytical techniques available to geochemists a high priority.

The techniques that are widely used in the trace element analysis of mineral grains, and which were chosen for this study were:-

- *proton-induced X-ray emission* (PIXE) analysis, using an Oxford proton microprobe at the National Accelerator Centre (NAC) in Faure, western Cape, South Africa;
- *secondary ion mass spectrometry* (SIMS), using a Cameca IMS-6f ion microprobe in the Department of Terrestrial Magnetism (DTM) at the Carnegie Institution of Washington, Washington, DC; and
- *laser ablation inductively coupled-mass spectrometry* (LA-ICP-MS), using an ELAN 6000 ICP-MS and Cetac LSX100 laser in the Department of Geological Sciences at the University of Cape Town (UCT).

1.4 Aims of Study

This study has two broad aims:

i) *To compare analytical techniques with respect to trace element analyses of garnet:*

- The three analytical techniques, viz. PIXE, SIMS and LA-ICP-MS, have been compared with respect to the determination of Ni, Zr and Y abundances in mantle garnets.
- Data have been evaluated in terms of accuracy, errors, detection limits and

agreement with data determined by other analytical methods.

ii) *To evaluate single garnet geothermobarometry against conventional geothermobarometry:*

- Most geothermobarometer combinations applicable to mantle peridotites were assessed by literature review and evaluation of results on two well-studied xenolith suites.
- The ability of the two Ni calibrations to reproduce temperature estimates determined by the commonly used conventional geothermometer has been assessed.
- "Garnet geotherms", constructed using single garnet geothermobarometry have been compared to geotherms determined by conventional geothermobarometry.

This study is based on two suites of well characterised (geochemically and mineralogically) mantle peridotites, one is from the Jagersfontein kimberlite pipe and the other is from the Matsoku kimberlite pipe (Chapter 2). Both these sample suites have peridotites with a wide range of textures, which include both coarse and deformed textures.

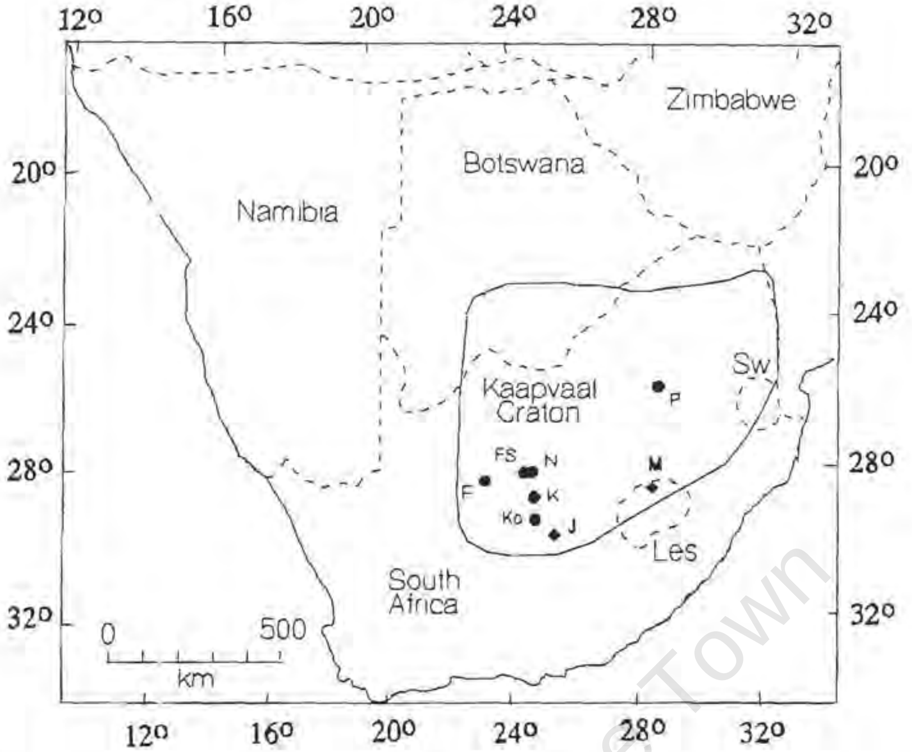

Fig. 2.1. Map of southern Africa (redrawn from Boyd and Gurney, 1986) showing the location of the Kaapvaal craton and the location of the kimberlites mentioned in the text. Also shown on the map is the location of some of the diamond producing kimberlites on the craton (F, P, Ko and K). J = Jagersfontein, M = Matsoku, FS = Frank Smith, N = Newlands; K = Kimberley, P = Premier, F = Finsch, Ko = Koffiefontein; Les = Lesotho, Sw = Swaziland.

After one hundred years, active mining of the Jagersfontein kimberlite pipe ended on 28 May 1971 (Wilson, 1972). The pit had became too deep and too small for economic mining, and the grades had dropped, from 14 carats per hundred tons (cpht) in 1913 to 6 cpht in 1965-70 (Wilson, 1972). The Jagersfontein mine, famous for the quality of its gem diamonds, like the *Excelsior* (995.20 carats), was kept going by its rare large stones (Wilson, 1972). The usually rare "blue white" diamonds were commonly found, but occasionally deep sapphire blue diamonds were also recovered. Matsoku kimberlite pipe was prospected, but never mined. Some diamonds were recovered in some of the prospecting samples, but overall, the pipe was found to be uneconomic (Gurney, *pers. comm.*).

2.2 Petrography

Extensive petrographic and geochemical work has been done on the mantle xenoliths selected for this study, e.g. Cox *et al.* (1973), Harte *et al.* (1975), Gurney *et al.* (1975), Harte and Gurney (1982), Winterburn (1987), Harte *et al.* (1987) and Hops (1989). Based on these studies, the samples selected have a wide range of textures, mineral chemistry and temperatures and pressures of equilibration.

Because of the requirements of this study, i.e. samples with coexisting olivine and garnet, sample selection was restricted to garnet peridotites. The textural classification used in this study is that of Harte (1977) (Table 2.1), and is based on the degree of olivine recrystallisation. A list of the samples selected and brief petrographic descriptions of each sample are presented respectively in Table 2.2 and Appendix A.1.

Table 2.1. Textural classification used in this study as defined by Harte (1977).

TEXTURE	DESCRIPTION
Coarse	Average grain size greater than 2 mm
Porphyroclastic	More than 10 volume % of the olivine occurs as porphyroclasts
Mosaic Porphyroclastic	More than 90 volume % of the olivine has recrystallised and pyroxenes are the dominant porphyroclasts
Laminar	Olivine and orthopyroxenes are associated with thin lenticles
Fluidal	Porphyroclasts of a mineral connect narrow stripes of the same mineral, occurring as tiny grains and extend across regions in which another mineral shows a dominantly mosaic texture.

The following is a discussion of the general petrography of the samples based on primary mineralogy. Unique samples in each sample suite are discussed in more detail.

2.2.1 Jagersfontein peridotites

Included in the selected Jagersfontein sample suite were garnet harzburgites, garnet lherzolites, a garnet dunite (JJH23), and a modally metasomatised garnet peridotite (JJG1716) (Winterburn, 1987; Winterburn and Harte, 1987; Field *et al.*, 1989). The samples selected had textures that include coarse[1], porphyroclastic, mosaic porphyroclastic and fluidal mosaic porphyroclastic in increasing degree of deformation (Plate 2.1 to 2.3).

Table 2.2 A list of the peridotite samples used in this study. The J series sample numbers are for Jagersfontein peridotites and the LBM series are for the Matsoku peridotites.

Sample no.	Type	Texture
J117	garnet lherzolite	coarse
JJG1710	garnet lherzolite	fluidal mosaic-porphyroclastic
JJG1716	garnet harzburgite	modally metasomatised coarse
JJG1728	garnet harzburgite	coarse
JJG1729	garnet lherzolite	porphyroclastic
JJG1733	garnet lherzolite	coarse
JJG1757	garnet harzburgite	coarse
JJG1761	garnet harzburgite	coarse
JJG864	garnet lherzolite	coarse
JJH1	garnet harzburgite	porphyroclastic
JJH10	garnet lherzolite	mosaic-porphyroclastic
JJH23	garnet dunite	mosaic-porphyroclastic
JJH28	garnet lherzolite	porphyroclastic
JJH29	garnet harzburgite	mosaic-porphyroclastic
JJH32	garnet lherzolite	mosaic-porphyroclastic
JJH35	garnet lherzolite	porphyroclastic
JJH6	garnet harzburgite	porphyroclastic
JJH7	garnet lherzolite	mosaic-porphyroclastic
JJH8	garnet lherzolite	mosaic-porphyroclastic
JJH9	garnet harzburgite	porphyroclastic
LBM10	garnet lherzolite	coarse
LBM16	garnet lherzolite	porphyroclastic
LBM17	garnet harzburgite	coarse
LBM20	garnet dunite	coarse
LBM22	garnet harzburgite	porphyroclastic
LBM3	garnet lherzolite	coarse
LBM30	garnet lherzolite	porphyroclastic
LBM32	garnet orthopyroxenite	porphyroclastic
LBM36-2	garnet pyroxenite	coarse
LBM36-3	garnet pyroxenite	coarse
LBM6	garnet lherzolite	coarse
LBM8	garnet harzburgite	coarse
LBM9	garnet lherzolite	coarse

---

[1] Coarse = undeformed.

Plate 2.1

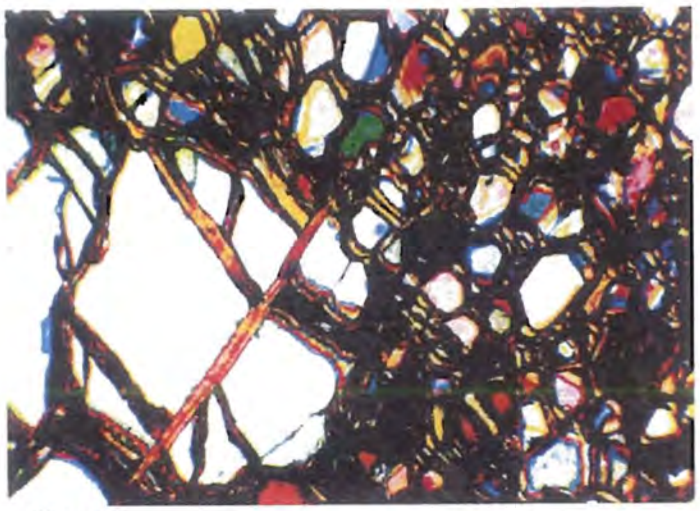

Plate 2.2

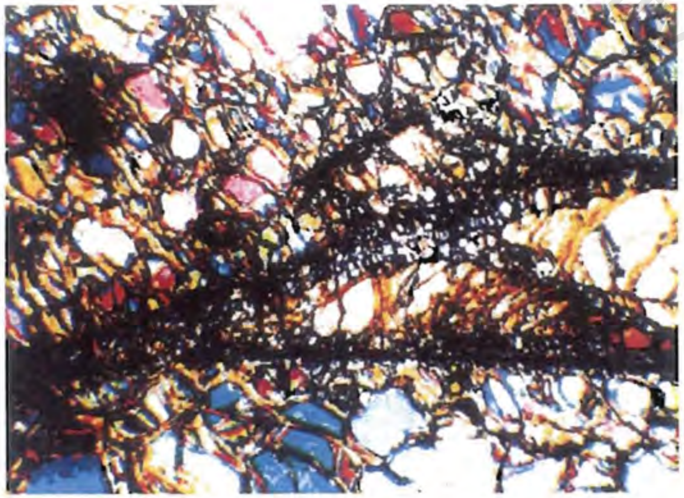

Plate 2.3

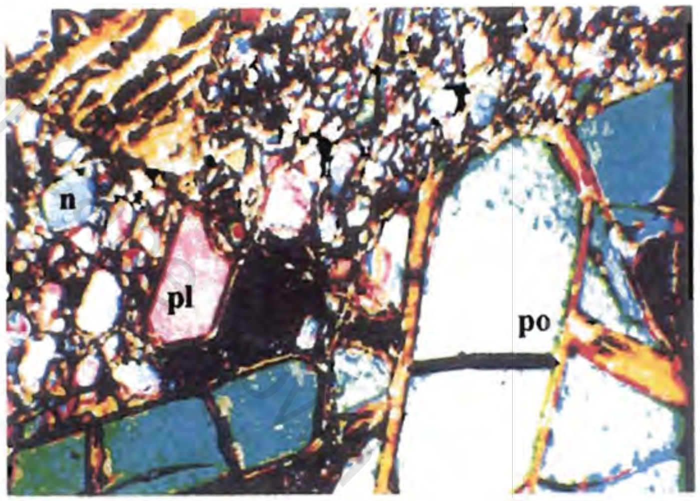

Plate 2.4

All photos taken in cross polarised light

Field of view = 1.5 mm

Plate 2.1. A coarse texture in JJG1761 with straight 120^0 triple point grain boundaries (highlighted by dotted lines). The grain boundaries are highly altered and serpentinised. ol = olivine, gt = garnet.

Plate 2.2 A large porphyroclast and smaller neoblasts of olivine in JJH32. The relative proportions of porphyroclasts and neoblasts define the texture (Table 2.1).

Plate 2.3 A fluidal porphyroclastic texture in JJG1710: a porphyroclast of orthopyroxene elongated to narrow strips of neoblasts of the same phase on both ends of the porphyroclast (one end shown).

Plate 2.4 JJH35: Three forms of olivine in deformed peridotites – po = porphyroclast, pl = platelet, n = neoblast.

The primary mineralogy of the samples is olivine, orthopyroxene, garnet and clinopyroxene in descending order of abundance. However, in some of the samples primary spinel and secondary phlogopite, sulphides and spinel were found. The secondary phases were mainly restricted to kelyphite rims of garnets and in metasomatic veins.

2.2.1.1 Jagersfontein deformed[2] peridotites

Olivine dominates in most of the peridotites, with modal percentages ranging from 50 to 90 volume (vol)% and an average grain size of 5mm. Olivines were the first to deform and occur in three forms: deformed *porphyroclasts* showing undulose extinction and unstrained *platelets* and *neoblasts* (Plate 2.4). The platelets were 1 mm in size in longest dimension and were found only in some of the peridotites. Neoblasts are a recrystallisation product of porphyroclasts and thus the relative proportions of the neoblasts and porphyroclasts is dependent on the degree of recrystallisation. In some of the peridotites olivine porphyroclasts have been completely recrystallised to neoblasts. Grain edges and fractures of the olivines have been serpentinised.

Orthopyroxene was the next phase to deform and is the second most abundant mineral in the majority of the peridotites, with modal abundances of 10 to 35 vol% and a grain size of 3mm. The recrystallisation of orthopyroxene porphyroclasts to neoblasts is restricted to grain edges and fractures (Plate 2.5). All orthopyroxenes in deformed peridotites show undulose extinction (Plate 2.5) and occur mostly as thin lenticles in extremely deformed peridotites (Plates 2.3). As in the olivines, serpentinisation varies from occurring in fractures, to completely replacing the orthopyroxenes in highly altered peridotites (Plate 2.6).

Garnet has a modal abundance ranging from 10 to 25 vol% and a grain size of 0.5 to 8 mm in diameter. Besides fracturing, which is observed in both coarse and deformed

---

[2] Deformed = sheared

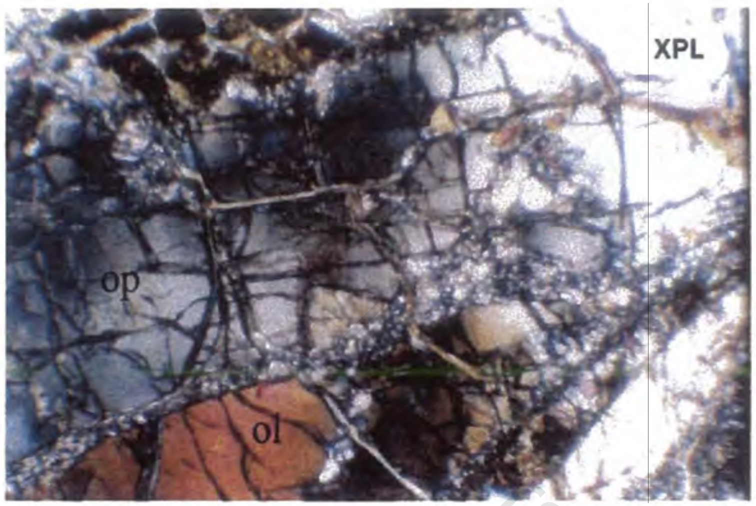

Plate 2.5

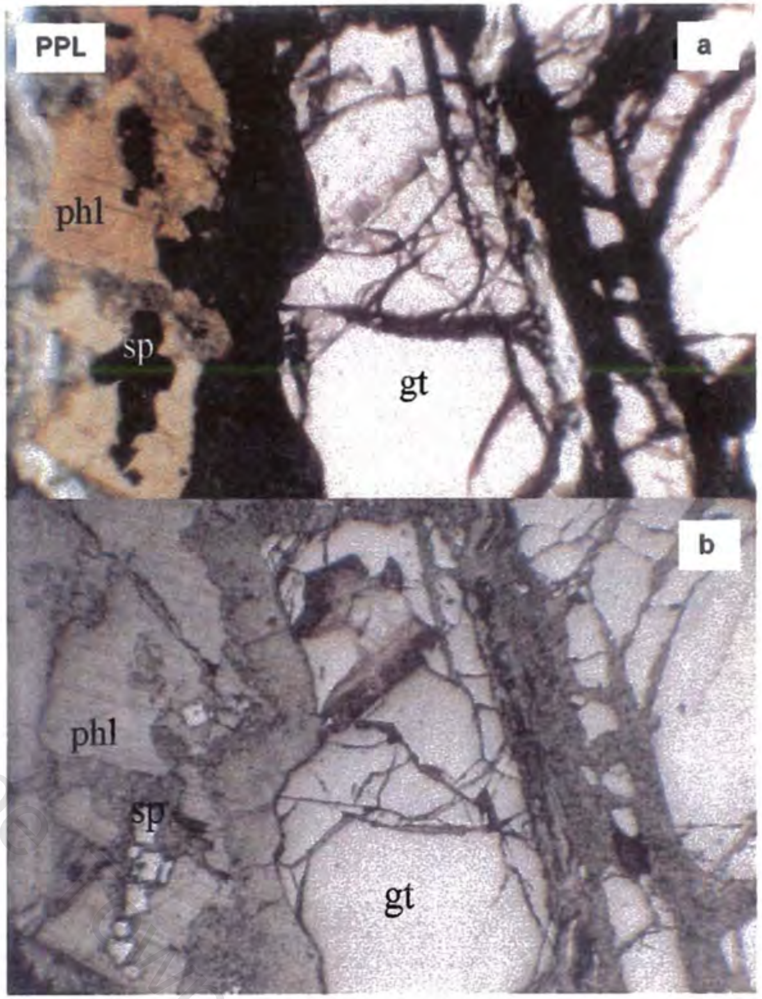

Plate 2.7

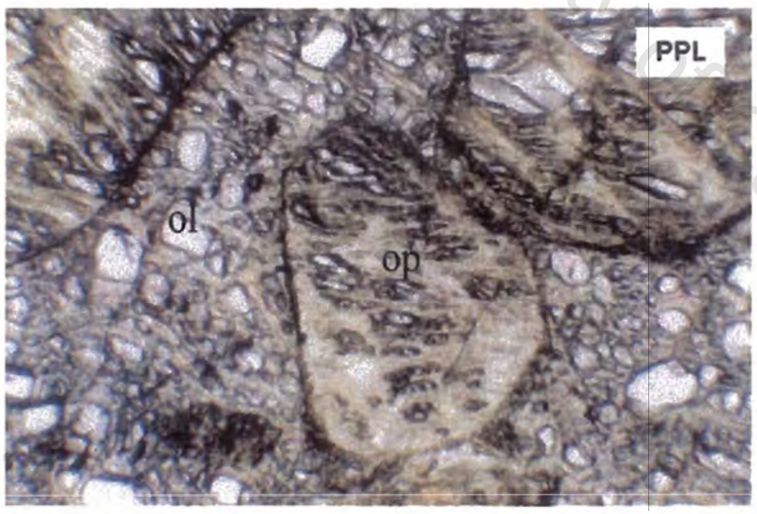

Plate 2.6

Field of view = 1.5 mm

PPL = plane-polarised light; XPL = cross-polarised light

Plate 2.5. Undulose extinction in orthopyroxene (op) in JJH6. Neoblasts are observed in fractures and grain edges of the orthopyroxene. ol = olivine.
Plate 2.6 Almost total replacement of orthopyroxene (op) by serpentine in JJH35. Olivine (ol) has been totally recrystallised to neoblasts in this sample.
Plate 2.7 Two kelyphite rims on a garnet (gt) in JJG1757. The inner rim is dark brown and microscopically unidentifiable. The outer rim is mainly composed of phlogopite (phl) and spinel (sp). The lower photo (b) is in reflected light to show the euhedral and subhedral nature of spinels.

peridotites, no indication of deformation (undulose extinction and recrystallisation) was found in the garnets. In most of the peridotites the garnets are round in shape, fractured and the kelyphite consists two concentric rims (Plate 2.7). The inner rim is dark brown and optically unidentifiable, whereas the outer rim mostly comprised phlogopite and spinel. In some of the samples, especially the smallest garnets, kelyphite rims have completely replaced the garnets (Plate 2.8).

Clinopyroxene is the least abundant primary mineral, with a modal abundance of 0 to 15 vol%. Like garnets, clinopyroxenes normally do not show internal deformation and recrystallisation to neoblasts. However, most of the clinopyroxene grains in deformed peridotites have 'spongy' grain edges, interpreted to result from decompression melting during transport to surface by the kimberlite (Carswell, 1975 and Ehrenberg, 1979) (Plate 2.9).

2.2.1.2 Jagersfontein coarse peridotites

In coarse peridotites mineral phases generally have 120^0 triple-point grain boundaries (Plate 2.1), indicating textural equilibrium. Grain boundaries are extensively serpentinised in all the coarse peridotites. Olivine has an average grain size of 8 mm and is highly fractured, altered and serpentinised. In addition to serpentine, phlogopite occurred in most of the fractures. Garnet has grain sizes of 2 to 6 mm and double-rimmed kelyphite rims as found in the deformed peridotites. Primary spinel occurs as anhedral grains in trace amounts in all the coarse peridotites (except J117).

One of the coarse peridotites (JJG1716) contains amphibole, which partially, and sometimes completely, encloses garnet (Plate 2.10). In this peridotite, garnet seems to have formed from exsolution of pyroxene, and occurs in a "necklace" texture (Plate 2.11). Olivine and orthopyroxene in this peridotite are highly serpentinised along grain boundaries and fractures within the minerals. The fractures are also filled with metasomatic minerals, mainly spinel, sulphides and phlogopite.

Plate 2.8

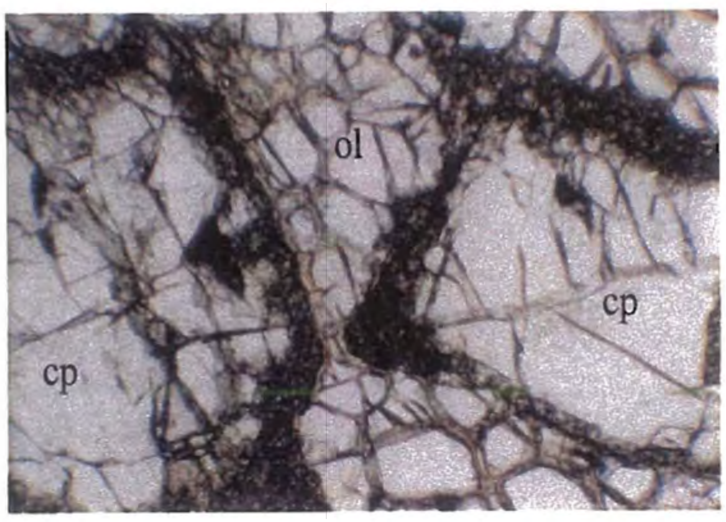

Plate 2.9

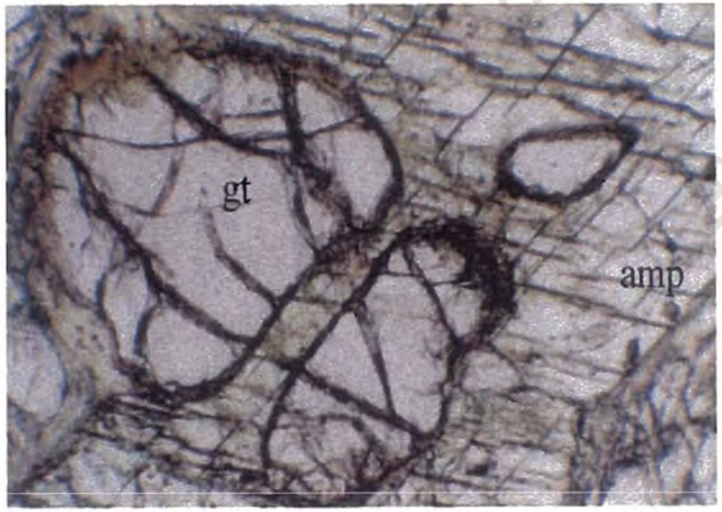

Plate 2.10

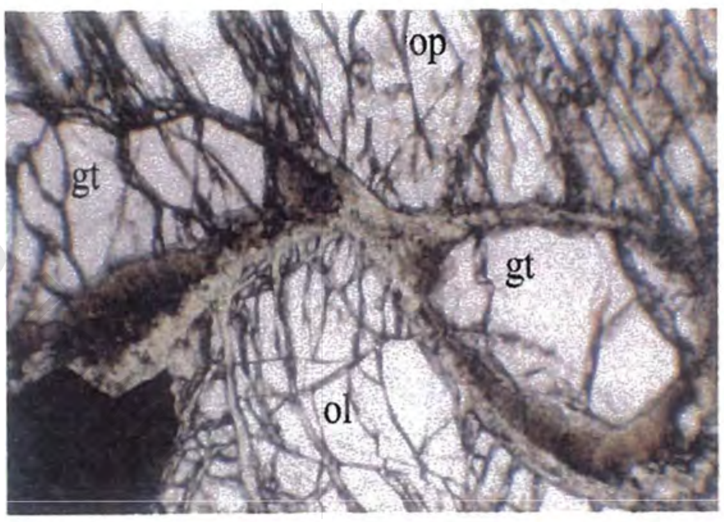

Plate 2.11

Field of view = 1.5 mm

All photos taken in plane-polarised light

Plate 2.8. An almost complete replacement of a garnet by kelyphite in JJG1729.
Plate 2.9 'Spongy' grain edges in clinopyroxenes (cp) in JJH10; ol =olivine.
Plate 2.10 Amphibole (amp) with inclusions of garnet (gt) in a modally metasomatised amphibole-bearing peridotite (JJG1716).
Plate 2.11 Garnets (gt) in a 'necklace texture' in JJG1716; op = orthopyroxene, ol =olivine.

Sample J117 is the only coarse, high temperature (Winterburn, 1987; Hops, 1989) peridotite in the sample suite. Although this peridotite has, on average, a coarse texture, olivine and orthopyroxene show undulose extinction. Moreover, clinopyoroxene has 'spongy' grain edges similar to clinopyroxenes in deformed peridotites (Plate 2.9).

2.2.2 Matsoku peridotites

The Matsoku kimberlite sampled a wide range of mantle xenoliths (Cox *et al.*, 1973; Harte *et al.*, 1975, 1987; Gurney *et al.*, 1975; Harte and Gurney, 1975) which included:

- non-metasomatised, intrusion-free xenoliths (both coarse and deformed nodules),
- banded xenoliths with cumulitic bands defined by variations in proportions of the constituent primary minerals,
- modally metasomatised xenoliths ([3]IRPS-bearing xenoliths),
- xenoliths with pyroxenite intrusion sheets, and
- xenoliths with garnet-rich veins.

However, due to a lack of coexisting garnet and olivine in most of the samples available for this study, the samples selected do not fully represent the range of mantle xenoliths sampled by the Matsoku kimberlite. The sample suite selected is dominated by garnet lherzolites, but also includes garnet harzburgites, a garnet dunite (LBM20) and a banded pyroxenite (LBM36). The textures of the selected samples include coarse, porphyroclastic and mosaic-porphyroclastic textures.

The primary mineralogy of the selected samples includes olivine, orthopyroxene, garnet and clinopyroxene. In some peridotites olivine is are the most dominant phase, whereas in others orthopyroxene is the most dominant phase. Clinopyroxene (except in LBM36) and garnet (except in LBM32) occurred as minor components.

---

[3] IRPS = Ilmenite Rutile Phlogopite Sulphide

2.2.2.1 Matsoku deformed peridotites

Olivine has modal proportions of 25 to 60 vol%. Where olivine porphyroclasts dominate over neoblasts, recrystallisation is restricted to grain edges and major fractures. Garnet has modal proportions ranging from 5 to 25 vol%, and is highly altered and completely replaced by kelyphite in some samples. In addition to occurring as porphyroclasts, garnet in some rocks forms streaks of altered, small, rounded grains (Fig. 2.12). These streaks are interpreted to have developed by deformation of garnet porphyroclasts (Cox *et al.*, 1973). Evidence for this is shown in Plate 2.13 where a large porphyroclast has small rounded garnets along its edge.

2.2.2.2 Matsoku coarse peridotites

Matsoku coarse peridotites generally have sub-straight to straight 120^0 triple-point grain boundaries. Olivine has modal proportions that range from 30 to 60 vol% and an average grain size of 5 mm. In some of the coarse peridotites olivine is intensely fractured and serpentinised, and shows undulose extinction. Orthopyroxene has modal proportions ranging between 40 and 60 vol%, and in some of the peridotites has olivine and clinopyroxene occurring as inclusions (Plate 2.14). Garnets are generally subhedral in shape and range from 1 to 5 mm in longest dimension. The modal proportions of the garnets vary between 2 and 10 vol%. Garnets have minor fractures and dark-brown kelyphite rims surrounded by a phlogopite-spinel outer-rim. Clinopyroxenes have modal proportions of 0 to 30 vol% and show no signs of deformation and internal strain, and minimal or no 'spongy' grain edges (Plate 2.15).

The relative proportions of ortho- and clinopyroxene distinguish the different bands in LBM36: LBM36-3 has less clinopyroxene and more orthopyroxene, whereas in LBM36-2 the relative proportions of the pyroxenes are reversed. Although the banded peridotite has, on average a coarse texture, olivine and orthopyroxene in this peridotite show undulose extinction. In addition, olivine has recrystallised to neoblasts along grain edges and clinopyroxenes have 'spongy' grain edges.

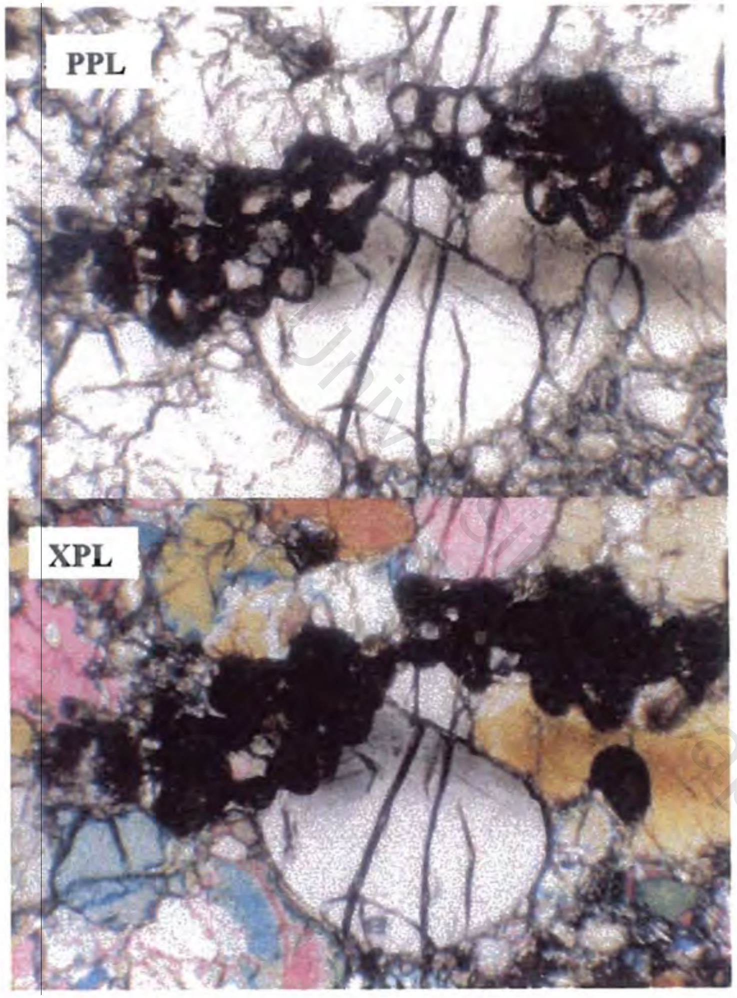

Plate 2.12

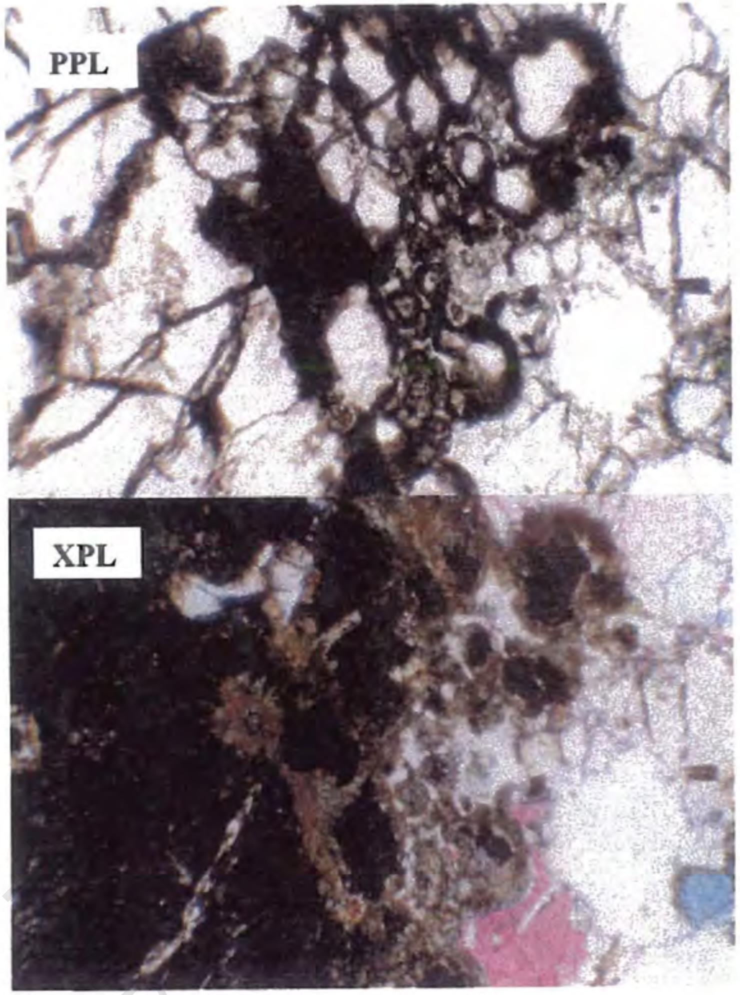

Plate 2.13

PPL = plane-polarised light; XPL = cross-polarised light **Field of view = 1.5 mm**

Plate 2.12. Rounded altered garnet grains drawn out to streaks in a porphyroclastic textured rock (LBM16).
Plate 2.13 A garnet porphyroclast surrounded by rounded smaller garnet grains in LBM16.

XPL

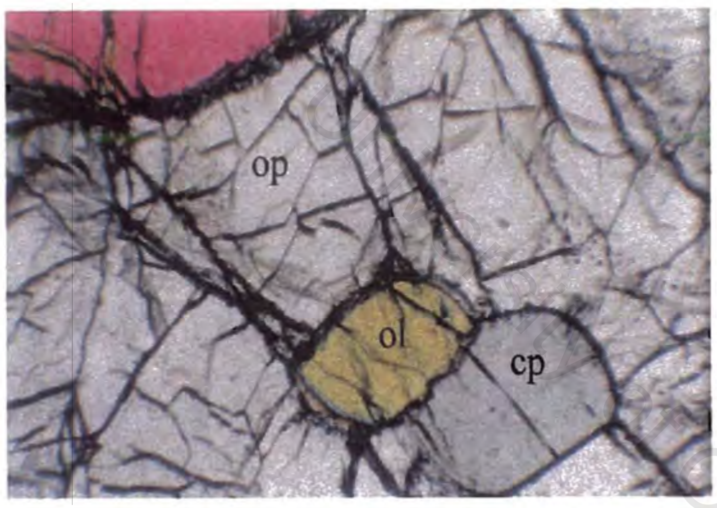

Plate 2.14

PPL

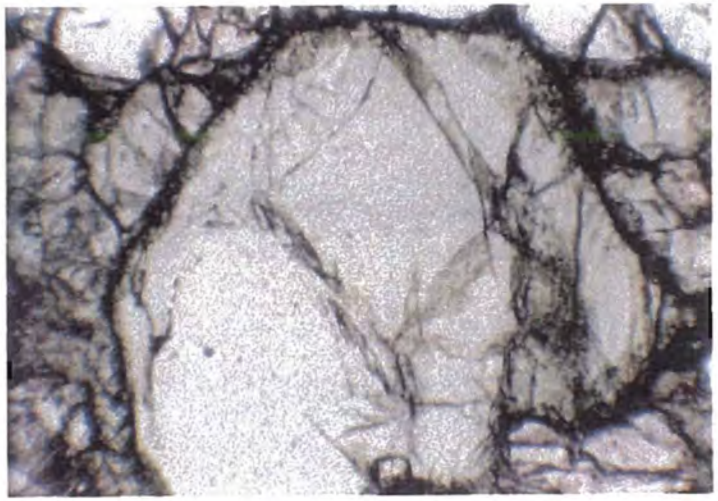

Plate 2.15

Field of view = 1.5 mm

Plate 2.14. An olivine (ol) and a clinopyroxene (cp) inclusion in an orthopyroxene (op) in LBM36-2.
Plate 2.15. A strain-free clinopyroxene with minimal 'spongy' grain edges in LBM10.

2.2.3 General Comments

The range of textures of the Jagersfontein sample suite illustrates the different stability fields of the mantle sampled by this kimberlite. The coarse peridotites (excluding J117) from this locality were sampled from a relatively shallower mantle within the garnet-spinel transition field (these garnet peridotites all contain spinel). The different textures of the Jagersfontein deformed peridotites manifest varying degrees of deformation, which probably occurred over a wide range of pressure-temperature (PT) conditions of equilibration (Hops, 1989).

Previous studies have shown that all Matsoku peridotites equilibrated at essentially the same PT conditions. The textures of the Matsoku samples selected are not as varied as the Jagersfontein peridotites and an overlap seems to exist between the P,T conditions for deformed and the coarse peridotites textures. The deformed peridotites are mostly porphyroclastic with recrystallisation of the olivines generally restricted to grain boundaries. The coarse peridotites, although with an average coarse texture, show some degree of deformation. In these peridotites, olivines and orthopyroxenes show undulose extinction and, in addition, some recrystallisation was observed in a few of the samples.

Kelyphite rims in garnets are found in both deformed and coarse peridotites. Thus, these rims are believed to have formed by subsolidus reactions after entrainment into the ascending kimberlite. Judging by the mineralogy of the outer rim, these reactions most probably occurred at similar PT conditions for both coarse and deformed peridotites, i.e., within the spinel and phlogopite stability fields. From the few peridotites containing clinopyroxene, it appears that the 'spongy' grain edges to clinopyroxene are confined to, or rather better developed in, the deformed peridotites. This might be due to the deformed peridotites having a larger change in PT conditions, by comparison to the coarse peridotites, during transport to surface.

Chapter 3

3. Analytical Methods

3.1 Introduction

Modern analytical techniques available to geochemists are capable of element analysis to trace levels with better precision and accuracy than before. The best analytical methods are those that enable analysts to acquire high quality data in an inexpensive and rapid manner. However, different techniques may still give dissimilar data values for the same sample and no technique is infallibly capable of absolute accuracy. Moreover, the same analytical technique can give different values for the same sample. For example, Campbell *et al.* (1996) reported an approximately 10% difference between their PIXE Ni data determined at the [4]CSIRO proton microprobe facility and the Ni data of Fedorowich *et al.* (1995) determined by PIXE at the [5]Guelph proton microprobe facility. Data reduction was done using the GeoPIXE (Ryan *et al.*, 1990) and the GUPIX (Maxwell *et al.*, 1989; Campbell *et al.*, 1996) software packages, respectively, at these facilities.

Of primary importance in the present study is the determination of the Ni content in mantle peridotite garnets. Ni geothermometry has emerged as a very important tool in mantle studies (e.g., Griffin *et al.*, 1992) and diamond exploration (Griffin and Ryan, 1995). In addition to calibration, the accuracy of the Ni geothermometers is strongly dependent on the quality of Ni data. Thus, the main objective of the analytical section of this study was to acquire high quality Ni data using PIXE, SIMS and LA-ICP-MS, compare these data, and select the most 'reliable' for use in the evaluation of Ni geothermometry.

Data 'reliability' has been tested by analysis of samples of 'known' composition where possible and by comparing data determined by different methods. Care was taken

---

[4] CSIRO, Heavy Ion Analytical Facility, Division of Exploration Geoscience, North Ryde, Australia.

[5] Department of Physics, University of Guelph, Guelph, Ontario, Canada.

to only compare data for samples that are homogeneous on the microscale. Homogeneity is particularly essential for standard samples used for calibration purposes and thus it was thoroughly tested for the secondary standards. In addition to Ni, other trace elements, e.g., Zr, Y and Ga, useful in mantle studies and diamond exploration have also been determined.

The trace element concentrations determined in this study were obtained by PIXE, LA-ICP-MS and SIMS techniques. The three techniques were chosen because of their wide use in *in situ* determination of trace elements in minerals. However, because of problems due to matrix effects there is no work published on analyses of Ni in garnets by SIMS. More importantly, these techniques are based on fundamentally different principles. PIXE is an X-ray fluorescence technique, using protons as primary ions. SIMS and LA-ICP-MS are both mass spectrometry techniques. However, these two methods differ in the methods of secondary ion production.

Ni determination at levels of tens of ppm in garnets presents a particular challenge to analysts. In SIMS, Ni isotopes suffer from interferences in mass spectra, mainly due to Si-O and Si-Si molecular ions. In PIXE, X-ray spectra for many Fe-bearing silicate minerals with low Ni abundances, including garnets, have a weak Ni$K\alpha$ X-ray line that lies on the flank of the relatively intense FeK_β X-ray line. The ratio of the intensities is about 100:1 (Fe:Ni) (Campbell *et al.*, 1996), due to the differences in element concentration. Thus, slight errors in the fitting of the Fe lines in the spectrum or the continuum background could cause significant errors in the inferred Ni concentration.

Analytical conditions used for each technique are discussed below. The descriptions of the specific instruments used are given in Appendix B.

3.2 Sample Preparation

All the three techniques compared in this study are capable of *in situ* analyses at a scale of tens of micrometers of selected points on polished sections. This allows a comparison of the trace element content of approximately the same spot in each sample using the three techniques, a basic requirement for a comparison of analytical data.

Samples were variously analysed as polished grain mounts, as "thick" thin sections (60μm) and as slabs. The grain mounts were prepared from the megacrysts, whereas the thin sections and slabs were prepared from the peridotite samples. The slabs were made for the LA-ICP-MS, for which thickness problems were encountered: under the analytical conditions used the laser penetrated right through the thin sections. For the electron microprobe and the proton microprobe the samples were coated with a thin conducting carbon film to avoid charge integration errors. For the ion microprobe the samples were coated with a thin conducting gold film to ensure that the sample offers a surface of equal potential with respect to the secondary ion extraction electrode, to facilitate stable collection of secondary ion signals. No coating was required for LA-ICP-MS.

3.3 Standard Samples

An evaluation and a comparison of analytical techniques requires standards for cross-checking agreement between the methods, for testing accuracy of each method and for the development of working curves where applicable. The first step was thus to establish garnet reference standards and determine their composition by multi-method analyses.

Twenty garnet megacrysts from Frank Smith (10) and Monastery (8) kimberlite pipes, and from an unknown locality (2) were selected for this purpose and were analysed for trace elements by PIXE. From these megacrysts three were selected in terms of sample size, clarity and homogeneity of trace elements, in particular Ni. In addition, the three samples were selected in such way that their Ni compositions would incorporate the whole range of the upper mantle peridotite garnet Ni composition, i.e. approximately 10 to 120 ppm (Griffin *et al.*, 1989).

The three samples selected were ROM33, MON32 and MON34, which respectively have ~50 ppm, ~60 ppm and ~120 ppm Ni (Chapter 4), and are all from Monastery. To incorporate the lower end of the Ni range, garnets from a garnet pyroxenite (JJG1424; AP le Roex, unpublished data), which have ~15 ppm Ni (Chapter 4), were included. In addition to the techniques compared in this study the solution-mode ICP-MS at UCT was used to chemically characterise the four standard samples. Also, for comparison, these garnets were sent to the University of Guelph, Canada, for PIXE trace element analysis using the GUPIX software package for data reduction.

3.4 Major Element Determination

The major element compositions of all the samples analysed for trace elements in this study were determined using the Cameca Camebax Microbeam electron microprobe in the Department of Geological Sciences, UCT. The electron beam was finely focused under the following conditions:

Accelerating potential = *15 kV*
Beam current = *40nA*
Beam diameter = *1 μm*

A peak counting time of 10 seconds was used for all elements, with the exception of Ni in olivine for which a counting time of 30 seconds was used to ensure determination of the trace amounts of Ni in olivine. Inter-element and matrix effects were corrected for using the PAP method (Pouchou and Pichoir, 1984). The detection limits, analysing crystals and standards used for the electron microprobe analyses are presented in Appendix B. Cores and rims of olivines, garnets and pyroxenes in each sample were analysed.

3.5 Trace Element Determination

3.5.1 Proton Microprobe

All the analyses were carried out using a 3MeV proton (H^+) beam and an Oxford proton microprobe at the National Accelerator Centre, Faure, South Africa. This particular instrument has been described in detail by Prozesky *et al.* (1995). Van Achterbergh (1994) and van Achterbergh *et al.* (1995) have presented its development as an analytical tool in geochemistry and its accuracy and precision.

The beam-on-target current was 4 nA with a spot size of 5-10 μm (Fig. 3.1). The secondary electron suppressor voltage was −1500 volts. The X-rays were detected using a LINK Si(Li) energy dispersive detector with an active area of 80 mm^2 and a detector-target distance of ~30 mm. The detector had a solid angle of 91.9 msr and an 8.0 micron thick Be window. Between the sample chamber and the detector there was a Kapton exit window of 13.00 μm thickness. In the present work the Fe X-rays which caused high dead time and pile-up peak contamination were attenuated using a 163 μm thick Al filter. The detector resolution was 180eV (for MnKα line). Each point analysis took ~5 minutes and the trace elements determined included Ni, Zr, Y, Ga and Zn.

Fig. 3.1. An electron micrograph of a spot (the centre of outward radiating cracks) made by the proton beam on one of the garnets analysed by PMP. The cracks are due to prolonged probing of one point. The mark is ~5 μm in diameter. (The scale bar is 1 μm).

Calibration of the proton microprobe was done using pure elements as reported by van Achterbergh (1994). Data reduction was achieved using the GeoPIXE software package (Ryan *et al.*, 1990). The major element composition of each garnet, determined by electron microprobe, was utilised to fix the matrix composition for the PIXE yield calculation. The Fe content (determined by electron microprobe) of each garnet to be analysed was used as an internal standard, to calculate a normalised concentration C_a^{norm} of a trace element a in the following manner:

$$C_a^{norm} = \frac{C_a^{PIXE} \times C_{Fe}^{EMP}}{C_{Fe}^{PIXE}}$$

where C_a^{PIXE} and C_{Fe}^{PIXE} are respectively the concentration of a and Fe determined by PIXE and C_{Fe}^{EMP} is the Fe content determined by electron microprobe. The 'reliability' of the normalised concentration depends on the accuracy of the electron microprobe data.

3.5.2 Ion Microprobe

SIMS analyses were carried out using a Cameca IMS-6F ion microprobe at the Department of Terrestrial Magnetism, Carnegie Institution of Washington, Washington DC. Samples were sputtered using a focused beam of oxygen (O^-) ions.

Due to interferences (mainly from Si-O and Si-Si molecular species) that affect the Ni peak in the mass spectrum, Ni analyses had to be carried out separately under high mass resolution. For Ni analyses the beam was focused to a spot of ~30 μm, with a primary accelerating voltage of -12.5 kV and a primary beam of 10 nA. Positive secondary ions were collected through a secondary high voltage of 10 kV. A high mass resolution of 4000 atomic mass units was used. Each Ni analysis took 10 minutes which included 300 seconds pre-sputtering and four 75 seconds blocks of data collection. Each block had 5 cycles, each involving 15 seconds counting time on the peak. ^{60}Ni and ^{30}Si isotopes were selected for the analyses. Secondary garnet standards were used to produce a Ni working curve (Fig. 4.5, Chapter 4).

Data for the other trace elements and rare earth elements (REE) were obtained under a low mass resolution of 300 atomic mass units. The beam was focused to a spot size of 15-20 μm. Energy filtering was used with an energy offset of 70 volts and an energy window of 50 eV. Each point analysis took ~40 minutes and included data for Li, Be, Sc, Ti, Sr, Y, Zr, Nb, Ba, La, Ce, Nd, Sm, Eu, Gd, Dy, Er, Yb, and Hf. Working curves for these elements were determined using the NIST glass standards (NIST 610, 612 and 614; *certified concentrations*, National Institute of Standards and Technology, USA) and a basaltic glass standard, BHVO (Frey and Clague, *unpublished data*).

3.5.3 Laser Ablation ICP-MS

LA-ICP-MS data were determined using a *CETAC LSX100* Nd:YAG[6] frequency quadrupled UV laser and a *Perkin-Elmer SCIEX Elan6000* ICP-MS at the Department of Geological Sciences, UCT. The laser was operated with a pulse energy of 1-2 mJ, a pulse repetition rate of 4 Hz with a 45 s delay time before data acquisition. The ablated sample material was flushed out of the sample cell by an Ar carrier gas which transported the sample to the plasma.

The sample pits made by the laser were ellipsoid-shaped on the surface, with a long axis of ~60 μm (Fig. 3.2). The number of sample spots on each garnet was limited mainly by the garnet size (surface area), but also the size of a polished area on the garnets which is away from cracks and inclusion-free. However, an attempt was made to obtain at least two data points on the core and on the rim of each garnet.

Fig. 3.2. An electron micrograph of a laser ablation pit on one of the garnets analysed by the *Cetac LSX100* laser, under conditions described in section 3.5.3. The pit is ellipsoidal on the surface with a longest dimension of ~60 μm. (The scale bar is 10 μm).

---

[6] Nd:YAG = Neodynium-doped $Y_3Al_2Al_3O_{12}$ garnet.

Trace element data were collected in peak-hopping mode. The data were collected in four replicates, each involving 20 sweeps with a dwell time of 40 ms, giving a total analysis time of 30 s. The mass spectrometer lens was set in auto-lens mode. The trace elements determined included Sc, Ni, Ga, Sr, Y, Zr and Yb.

	NIST612	NIST610
Ni	34.5	415
Ga	35.9	431
Y	41.2	490
Zr	42.1	490

Table 3.1. Ni, Ga, Y and Zr data (in ppm) for the NIST synthetic standards used for external calibration of LA-ICP-MS analyses. These data and those of other trace elements are as given by Norman *et al.* (1996) in their Table 4.

^{43}Ca (CaO determined by electron microprobe) was used as an internal standard for the normalisation of the intensity of all analyte elements. Calibration was achieved by producing working curves for each element using the synthetic glass reference standards, NIST 612 and NIST 610 (Table 3.1). Background counts for the Ar carrier gas were determined prior to this calibration. In addition, one of the secondary external standards, MON32, was analysed before and after each calibration.

Chapter 4

4. Analytical Results

4.1 Introduction

In this chapter major element data for the secondary garnet standard samples and the peridotite garnets, analysed by electron microprobe, and trace element data acquired by PIXE, solution ICP-MS, LA-ICP-MS and SIMS are presented. The main focus is on Ni concentrations in these garnets, which is of major interest to this study. However, data for Zr, Y and Ga in the garnets are also presented, mainly because the concentrations of these elements are used in conjunction with Ni concentrations in diamond exploration target area selection (Griffin and Ryan, 1995). Although not discussed or used in this study, data for other trace elements analysed are presented in Appendix C.1.

Trace element data are presented as means, together with their 2σ errors and relative standard deviation as percentages calculated from repeat analyses of each sample. Amongst other factors, counting times and the number of analyses on each sample affect precision. Ideally, for comparison of analytical precision between techniques, similar number of analyses must be done using each method. As is discussed below, it was impracticable to do as many analyses as intended. Thus precisions presented here do not necessarily represent the optimum capabilities of the methods used but serve as an indication of the reproducibility of the data obtained.

It was, however, not the aim of this study to investigate the optimal analytical conditions and set procedures (e.g. analysis time) of each analytical technique used. The main objective was to use the routine procedures at each technique to acquire Ni contents of peridotite garnets, compare the data, and decide which dataset was the most 'reliable' for use in the evaluation of Ni geothermometers. However, where applicable the standard procedures were modified to suit the needs of this study; for example, in-house secondary garnet standards produced in this study were used to create a Ni working curve for SIMS as it was clear that calibration against NIST glass standards gave erroneous results (section 4.3.2.2).

4.2 Secondary garnet standards

The major and trace element data for all the garnet megacrysts (including those not selected for use as standards), respectively determined by electron microprobe and PIXE are presented in Appendix C.2. A summary of the major and trace element analyses for the three garnet megacrysts and the JJG1424 garnets, selected for making secondary garnet standard samples, are presented in Table 4.1. These garnets are generally close in major element composition to the peridotite garnets used in this study (Table 4.1). The only major difference is in Cr and Ti compositions. The three garnet megacrysts are Cr-poor (0.23 to 0.79 wt% Cr_2O_3) and have high Ti contents (1.10 to 1.17 wt% TiO_2), whereas the peridotite garnets have a higher Cr content (1.39 to 11.39 wt% Cr_2O_3) and a relatively lower Ti content (0.02 to 0.81 wt% TiO_2).

4.2.1 Ni composition of the secondary garnet standards

The trace element composition of the garnet standards was analysed using PIXE, solution ICP-MS and LA-ICP-MS. The solution ICP-MS Ni data were the most precise, with errors of 2 to 3 % (2σ) over the range ~50 to 121 ppm. These data showed generally good agreement with the means of the LA-ICP-MS data (Fig. 4.1). The LA-ICP-MS Ni data had 2σ errors of 4 to 11% for ~12 to ~122 ppm (the large errors in Table 4.1 are associated with limited analyses or low element abundances). Although PIXE Ni data were slightly higher than solution ICP-MS and LA-ICP-MS Ni data, these data still agreed within error with those from the other two techniques (Fig. 4.1). PIXE data determined at NAC and at the University of Guelph showed a remarkable agreement although these data were respectively, processed using GeoPIXE and GUPIX software programmes (Fig. 4.1) which have been reported to reproduce significantly different results (Campbell *et al.*, 1996). These data were within their 2σ errors of, respectively, 6 to 8 % and 3 to 5% at ~15 to 136 ppm Ni.

	ROM33	MON32	MON34	JJG1424	Peridotite Garnets
SiO2	41.63	41.72	41.95	41.86	40.32 - 42.65
TiO2	1.17	1.10	1.13	0.09	0.02 - 0.81
Al2O3	21.75	21.92	21.51	23.47	14.32 - 23.07
Cr2O3	0.13	0.27	0.79	1.06	1.39 - 11.39
FeO	12.21	11.58	9.85	8.11	5.21 - 10.46
MnO	0.34	0.31	0.24	0.3	0.21 - 0.54
MgO	18.48	18.72	20.15	20.39	19.96 - 23.55
CaO	4.62	4.54	4.64	4.69	2.23 - 8.24
Total	100.34	100.17	100.25	99.97	

Table 4.1. Major element (wt%) and trace element (ppm) data for the secondary garnet standards. The range of major element data for the peridotites under study is included for comparison of matrix compositions. The errors are 2σ errors. n = the number of analyses

		PIXE - GeoPIXE			PIXE - GUPIX			Laser			ICPMS		
	Sample	Mean	n	%RSD	Mean	n	%RSD	Mean	n	%RSD	Mean	n	%RSD
Ni	JJG1424	14.6 ± 1.2	13	8%				12.4 ± 3.7	3	30%	15.7 ; 14.9	2	
	ROM33	54 ± 5	4	8%	51 ± 3	10	5%	51 ± 10	4	20%	49 ± 2	4	3%
	MON32	67 ± 6	4	8%	68 ± 2	9	4%	65 ± 2	2	4%	64 ± 2	4	3%
	MON34	134 ± 8	4	6%	136 ± 4	10	3%	122 ± 14	7	11%	121 ± 3	4	2%
Zr	JJG1424	30 ± 2	13	7%				30 ± 5	3	17%	31 ; 31	2	
	ROM33	149 ± 12	4	8%	147 ± 7	10	5%	154 ± 9	4	6%	146 ± 4	4	3%
	MON32	121 ± 1	4	1%	116 ± 2	9	2%	118 ± 3	24	2%	125 ± 4	4	3%
	MON34	114 ± 4	4	4%	111 ± 2	10	2%	119 ± 4	7	3%	119 ± 5	4	4%
Y	JJG1424	27 ± 1	13	3%				22 ± 4	3	18%	25 ; 25	2	
	ROM33	47 ± 1	4	3%	43 ± 1	10	3%	47 ± 2	4	5%	46 ± 1	4	1%
	MON32	41 ± 3	4	7%	39 ± 1	9	3%	40 ± 1	24	2%	42 ± 0	4	1%
	MON34	39 ± 2	4	6%	39 ± 1	10	3%	41 ± 1	7	4%	41 ± 0	4	1%
Ga	JJG1424	8.2 ± 0.4	13	5%				6.8 ± 1.5	3	23%			
	ROM33	21 ± 2	4	7%	21 ± 1	10	5%	19.8 ± 5.0	4	25%			
	MON32	19.1 ± 1	4	4%	20 ± 1	9	5%	19.4 ± 0.9	24	4%			
	MON34	15.4 ± 2	4	12%	14.9 ± 0.8	10	5%	13.9 ± 1.9	7	13%			

The means of Ni data for each sample analysed by the three techniques were compared using the *Student t-test*. The *null hypothesis* of the test is that the two means of analytical data obtained by two techniques compared are the same at 95% confidence level and an *alternative hypothesis* that the two means are significantly different. The results of the test, presented in Table 4.2, show that the *null hypothesis* holds for ten of the twelve comparisons for Ni: the pairs of means for MON34 and those for ROM33 Ni data, analysed by solution ICP-MS and PIXE are significantly different at 95 % confidence level.

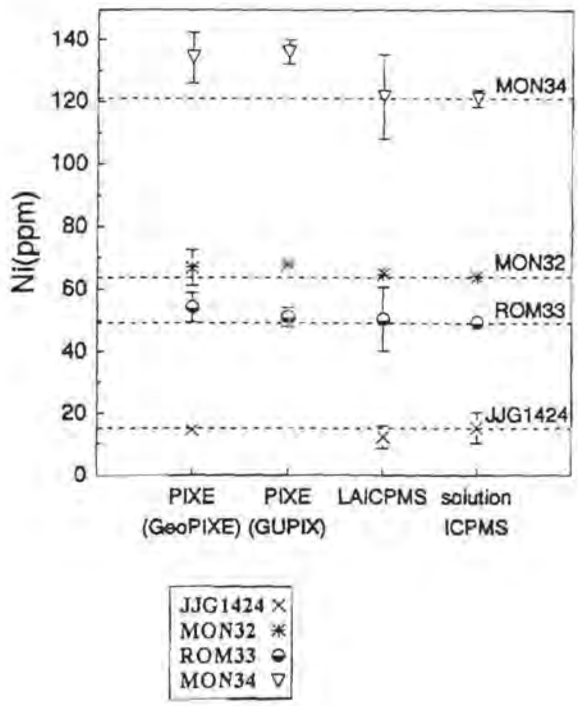

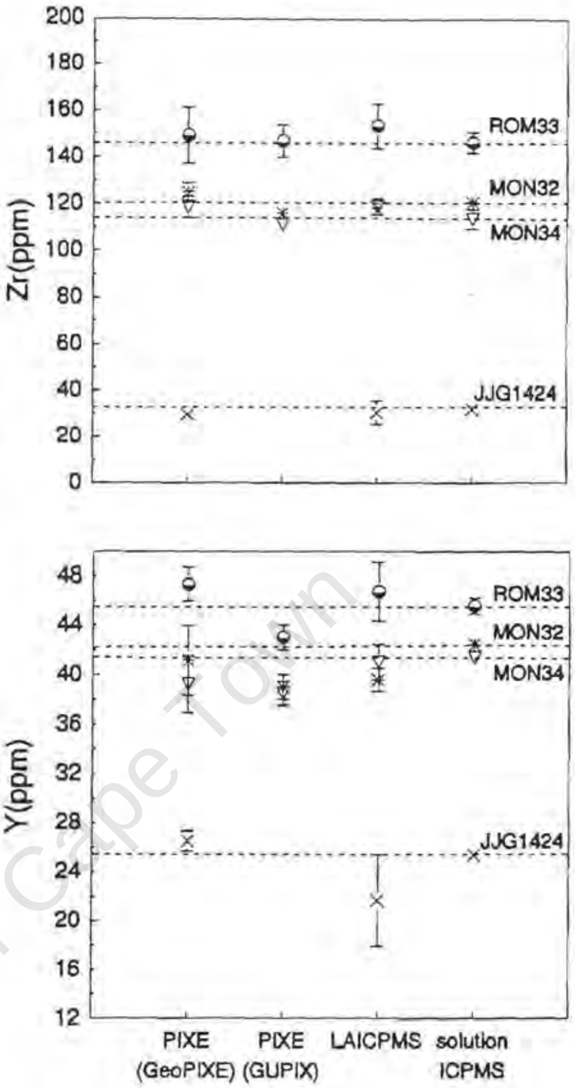

Fig. 4.1. Ni, Zr and Y data for the secondary garnet standards. The error bars represent 2σ error. The dotted lines are drawn through solution ICP-MS data for comparison. PIXE data processed by GeoPIXE at NAC and by GUPIX software at Guelph are shown.

	Sample#	ICP vs PIXE	ICP vs Laser	PIXE vs Laser
Ni	JJG1424	Yes	Yes	Yes
	ROM33	No	Yes	Yes
	MON32	Yes	Yes	Yes
	MON34	No	Yes	Yes
Zr	JJG1424	Yes	Yes	Yes
	ROM33	Yes	Yes	Yes
	MON32	No	Yes	Yes
	MON34	No	Yes	No
Y	JJG1424	Yes	No	No
	ROM33	No	Yes	Yes
	MON32	Yes	Yes	Yes
	MON34	No	Yes	No
Ga	JJG1424	▨	▨	No
	ROM33	▨	▨	Yes
	MON32	▨	▨	Yes
	MON34	▨	▨	Yes

Table 4.2. A comparison of means of data determined by different methods, using the Student t-test at 95% confidence level. Yes = the means are equal or the null hypothesis holds (section 4.2.1); No = the means are not equal or the alternative hypothesis holds (section 4.2.1); Laser = LA-ICP-MS; ICP = solution ICP-MS. Ga was not analysed by solution ICP-MS. PIXE = data processed using GeoPIXE.

The agreement of the data obtained by the three techniques indicates that the accuracy of these methods is probably good. The reproducibility of data for each sample suggested that the samples are homogeneous when it is considered that different garnet grains, randomly selected from each sample of crushed megacryst and pyroxenite garnets, were analysed by the three techniques. Moreover, in some cases different points on each garnet grain were analysed by PIXE and LA-ICP-MS. The homogeneous nature of these samples, the similarity of their major element composition to the peridotite garnets used in the present study and the fact that their Ni content span the range of interest (~10 to ~120 ppm) justify their use as Ni secondary standards for the present study.

4.2.2 Zr, Y, and Ga contents of the secondary garnet standards

Zr, Y and Ga analyses generally had 2σ errors of less than 10% (Table 4.1). The few large errors can be explained as for Ni (section 4.2.1). The comparison of the Zr, Y, and Ga data analysed using the three techniques is presented in Table 4.2 (*Student t-test*) and Fig. 4.1. The techniques are generally in agreement, with the few comparisons for which the null hypothesis of the *t-test* does not hold still being within error of each other (Table 4.1, Fig. 4.1).

4.3 Garnet Peridotite Analyses

4.3.1 Major element analyses of the garnet peridotites

Major element analyses of garnets, olivines, orthopyroxenes and clinopyroxenes are presented in Appendix C.3. Matsoku peridotites have olivines with Mg#'s [7] ranging from 87 to 93, and thus have both Mg-rich (Mg# >91) and Fe-rich (Mg# < 91) olivines, according to the classification scheme of Harte (1983), without a distinction between deformed and coarse peridotites. On the other hand, Jagersfontein deformed peridotite olivines are Fe-rich (Mg# = 90 to 92), whereas the coarse peridotite olivines are Mg-rich

---

[7] Mg# = 100*Mg/(Mg+Fe) atomic proportions.

(Mg# = 92 to 94).

The orthopyroxenes are enstatites and have Al contents ranging from 0.54 to 1.28 wt% Al_2O_3 in Jagersfontein peridotites (Fig 4.2a). In Matsoku peridotites these enstatites have a generally much narrower range of Al content (0.69 to 0.87 wt% Al_2O_3; Fig 4.2a). The orthopyroxenes in Jagersfontein peridotites have Mg#'s ranging from 91 to 95, whereas those from Matsoku peridotites have Mg#'s ranging from 89 to 94 (Fig. 4.2a). The orthopyroxenes from Jagersfontein coarse peridotites are more Mg-rich (higher Mg#'s) than those from deformed peridotites (Fig. 4.2a). Such a distinction is not observed in Matsoku peridotites.

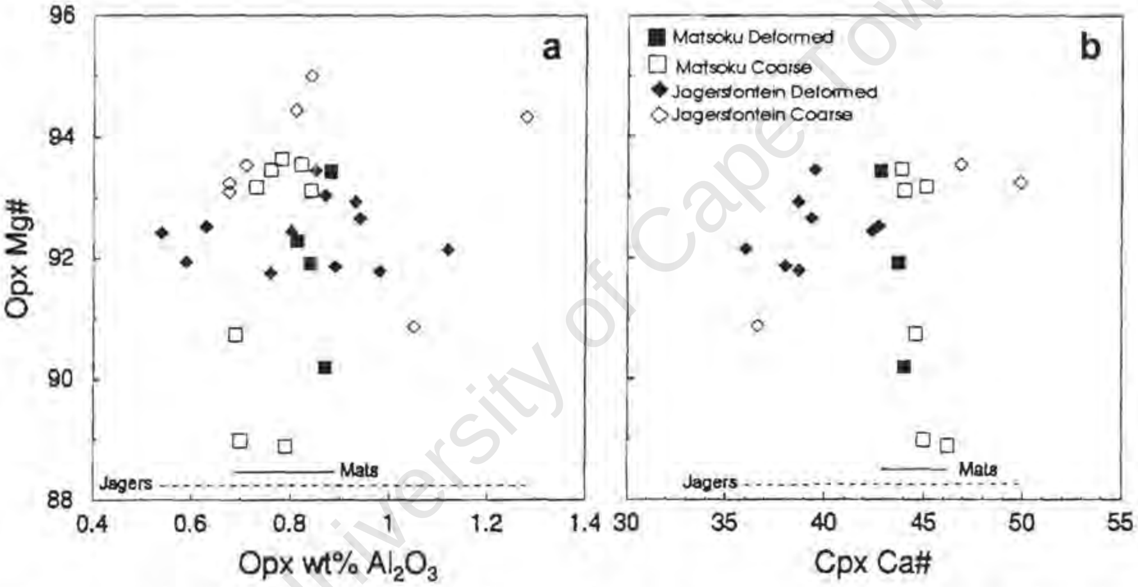

Fig. 4.2. A plot of (a) Al content against Mg# (100*Mg/Mg+Fe) of orthopyroxenes (opx) and (b) a plot of clinopyroxene (cpx) Ca# (100*Ca/Ca+Mg) against opx Mg#. The horizontal lines show the range in composition of the samples from the two localities (Mats = Matsoku, Jagers = Jagersfontein). Not all samples are plotted in both diagrams, as some do not contain any clinopyroxene, hence the missing data points in (b).

The clinopyroxenes are Cr diopsides with 0.59 to 2.56 wt% Cr_2O_3 in Jagersfontein peridotites and 0.77 to 2.38 wt% Cr_2O_3 in Matsoku peridotites. Ca concentration varies widely in Jagersfontein peridotite clinopyroxenes ([8]Ca# = 36 to 47), but is essentially constant in Matsoku peridotite clinopyroxenes (Ca# = 43 to 45) (Fig. 4.2b).

---

[8] Ca# = 100*Ca/(Ca+Mg) atomic proportions.

The garnets are Cr pyropes with Cr contents varying from 1.64 to 11.39 wt% Cr_2O_3 in Jagersfontein peridotites, and from 1.88 to 6.71 wt% Cr_2O_3 in Matsoku peridotites. Most of these garnets are calcic, with Ca contents of 4.00 to 8.24 wt% CaO. On the basis of a Cr_2O_3-CaO plot (Gurney and Switzer, 1973; Fig. 4.3), garnets from four Jagersfontein peridotites have 'G10' garnets[9]. In contrast, none of the Matsoku peridotites contain such garnets.

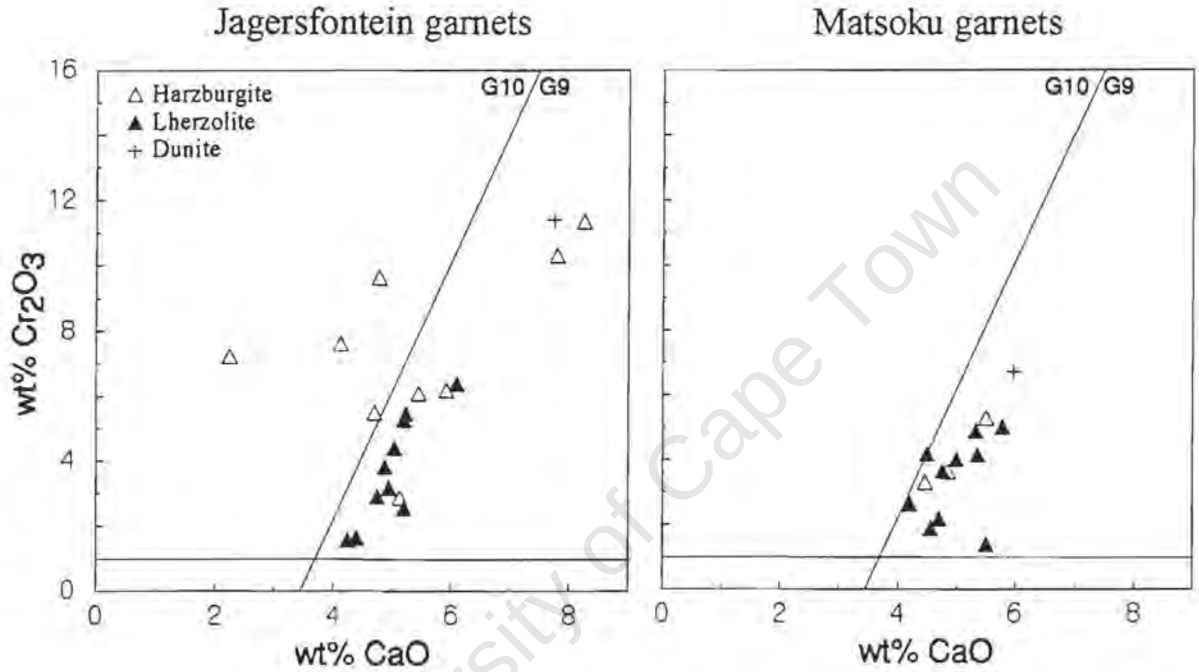

Fig. 4.3. A Cr_2O_3 vs CaO plot for the garnets analysed in this study. Four of the Jagersfontein peridotites have G10 garnets, whereas none of the Matsoku samples have these subcalcic garnets. The classification as harzburgite, lherzolite and dunite is according to petrographic observations.

4.3.2 Ni analyses of the peridotite olivines and garnets

The Ni contents of olivines were analysed using electron microprobe and are presented in Table 4.3. Jagersfontein peridotite olivines have Ni contents ranging from 2570 to 3400 ± 228 ppm Ni (1σ, counting statistics), and those from Matsoku peridotites have 2520 to 3670 ± 229 ppm Ni. Thus, all the olivines have Ni contents that fall within the range (3000±500 ppm Ni) suggested by Griffin *et al.* (1989) for mantle olivines.

---

[9] G10 garnets are harzburgitic garnets with high proportions of MgO and Cr_2O_3 and low proportions of CaO (Gurney and Switzer, 1973), similar to the G10 class of Dawson and Stephens (1975), and to garnets found as inclusions in diamonds.

Table 4.3. Ni composition (ppm) of garnets and olivines from the peridotites under study. Data presented are means for the analyses done on each sample; where only two analyses on garnets were done by PIXE and LA-ICP-MS these two analyses are given (in *italics*); n = number of analyses. The errors are 2σ errors.

		Ni(ppm)						
		GARNETS						**OLIVINES**
		PIXE		**LA-ICP-MS**		**SIMS**		**EMP**
		n	**Average**	**n**	**Average**	**n**	**Average**	**Average**
Jagersfontein	**J117**	6	85 ± 2	6	112 ± 10	2	95 ± 0.3	2860
	JJG1710	6	102 ± 4	4	96 ± 14			2990
	JJG1716	6	16.4 ± 1.3	6	17.9 ± 3.6	2	17.7 ± 0.4	3190
	JJG1728	6	35 ± 3	*2*	*34 ; 34*			2890
	JJG1729	11	94 ± 3	5	78 ± 5			2980
	JJG1733	12	14.1 ± 1.1					3190
	JJG1757	6	57 ± 3	*2*	*62 ; 53*	2	69 ± 0.3	2650
	JJG1761	6	35 ± 1	8	45 ± 2	2	36 ± 0.2	2570
	JJG864	5	26 ± 5	4	26 ± 3	2	32 ± 0.2	3400
	JJH1	6	63 ± 3	5	72 ± 5	2	89 ± 0.2	3080
	JJH10	6	100 ± 5	6	86 ± 2	2	100 ± 0.3	3140
	JJH23	6	73 ± 5					3080
	JJH28	6	77 ± 5	12	72 ± 3	2	77 ± 0.3	3000
	JJH29	6	92 ± 2	7	88 ± 7			2970
	JJH32	12	99 ± 2	9	100 ± 10	2	88 ± 0.3	3060
	JJH35	6	71 ± 3					2880
	JJH6	3	77 ± 7	3	81 ± 8			3100
	JJH7	12	101 ± 4	1	100	2	108 ± 0.3	2750
	JJH8	6	99 ± 3			2	113 ± 0.3	3040
	JJH9	6	77 ± 5	3	75 ± 19			3050
Matsoku	**LBM10**	6	41 ± 3	4	45 ± 3	2	57 ± 0.2	3440
	LBM16	6	47 ± 4	6	39 ± 4			3300
	LBM17	6	46 ± 3	4	47 ± 11	2	52 ± 0.3	3200
	LBM20	9	51 ± 4					3060
	LBM3	6	45 ± 3	5	46 ± 6	2	48 ± 0.2	3380
	LBM30	*2*	*47 ; 46*					2520
	LBM32	9	35 ± 2			2	50 ± 0.2	2810
	LBM36-2	9	48 ± 2			2	62 ± 0.2	3670
	LBM36-3	6	54 ± 4	3	53 ± 5	2	58 ± 0.2	3580
	LBM6	6	56 ± 3	4	53 ± 4			3230
	LBM8	6	43 ± 2	8	42 ± 4	2	55 ± 0.2	3390
	LBM9	6	43 ± 2	5	39 ± 2	2	53 ± 0.3	3560

None of the garnets analysed, by any of the methods used in the present study, show any evidence for Ni heterogeneity. Average Ni abundances, determined by each technique, are presented in Table 4.3. Jagersfontein peridotite garnets have Ni contents ranging from ~14 to ~110 ppm. In contrast, Matsoku peridotite garnets have a narrow range of Ni contents (~35 to ~55 ppm).

4.3.2.1 Ni analyses of peridotite garnets - PIXE

PIXE analyses were the first to be carried out and from these analyses it was discovered that all the garnets analysed have homogeneous Ni compositions, within and between garnets in each peridotite. The PIXE Ni analyses presented in Table 4.3 are generally an average of six analyses (three core + three rim analyses). In some cases more than one garnet was analysed in a sample, hence averages of more than six analyses are presented. Only core analyses were carried out on small and/or altered garnets, and hence averages of only three analyses are presented.

Precision of Ni determinations by PIXE (based on counting statistics) for Ni abundances in the range of 14 to 101 ppm typically varied between 2 and 10% relative (95% confidence limit) (Table 4.3, Fig. 4.4). Limits of detection (L.O.D.) were ~6 ppm, calculated by the GeoPIXE software at 99% confidence level, using the following relationship of Currie (1958):

$$L.O.D. = 3.29\sqrt{B} \qquad (4.1)$$

where B is the background intensity.

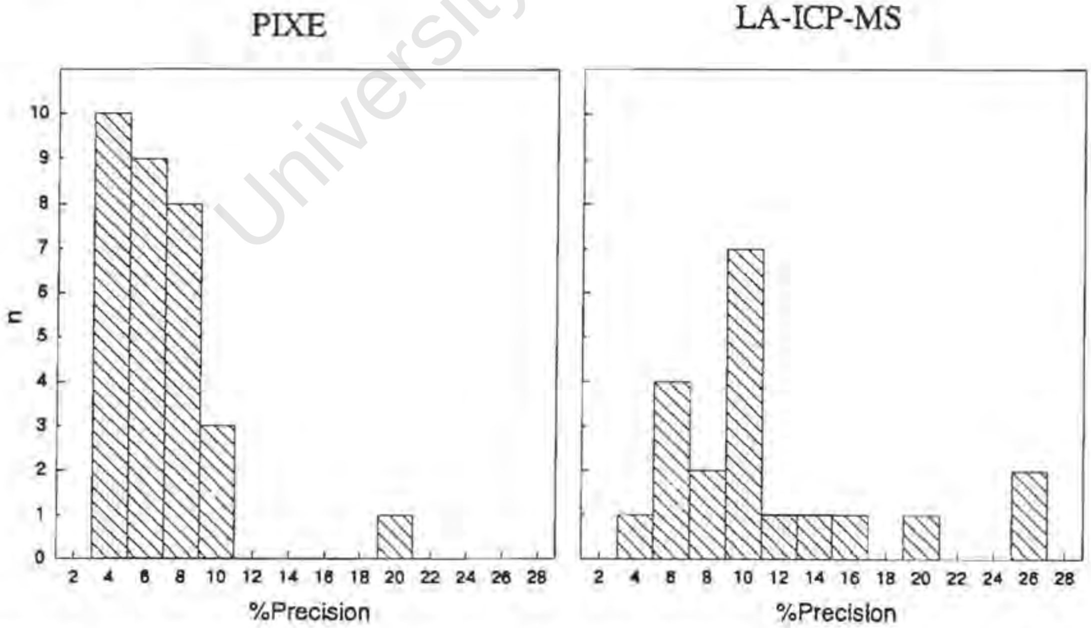

Fig. 4.4. A graphical illustration of the reproducibility of the Ni data obtained by PIXE and LA-ICP-MS under the analytical conditions used in this study. n = frequency of data, % Precision is the percentage ratio of the 2σ error to the mean value.

A further test for precision was performed on a garnet from one of the Matsoku peridotites, LBM9. The Ni concentration of this garnet was determined on two different days separated by a three month period under similar analytical conditions. Similar results for Ni concentration and precision were obtained (43±2 and 45±2 ppm Ni, Table 4.4) on both these days.

Point	Ni(ppm) 23/10/1997	Ni(ppm) 09/12/1997
1	44	46
2	44	46
3	40	45
4	44	46
5	45	42
6	40	48
7		48
8		45
9		43
10		40
Average	43	45
Average error	2	2
%RSD	4%	4%

Table 4.4. Ni data for a garnet from LBM9, analysed by PIXE on two different days, three months apart. The errors are 2σ errors of the repeat analyses presented.

In addition to comparing PIXE Ni analyses with solution ICP-MS analyses, these analyses were compared with analyses done by Instrumental Neutron Activation Analysis (INAA). PIXE analysis of a garnet megacryst, previously analysed by INAA (Hart, unpublished data) was carried out. The results are presented in Table 4.5 and show an agreement between PIXE and INAA Ni data.

	Point	Ni(ppm)
PIXE	1	123 ± 2
	2	122 ± 2
	3	118 ± 2
	4	123 ± 2
	5	118 ± 2
	Average	121 ± 2
INAA		121 ± 2

Table 4.5. PIXE repeat analyses on a garnet megacryst (GHR1), previously analysed by INAA (Hart, unpublished data). The errors are 2σ errors.

4.3.2.2 Ni analyses of peridotite garnets - LA-ICP-MS

Errors (2σ) for Ni analyses by LA-ICP-MS typically varied between 4 and 12 % relative for Ni abundances of ~18 to ~112 ppm (Table 4.3, Fig. 4.4). The L.O.D. for the Ni analyses by LA-ICP-MS was ~0.5 ppm, calculated using equation 4.2 with the background intensity determined using the Ar gas blank at the same analytical conditions as the analyses:

$$L.O.D. = 3 \times \left(\sqrt{2 \times I_{blank}}\right) \times \left(\frac{C_{std}}{I_{std} - I_{blank}}\right) \qquad 4.2$$

where I_{blank} and I_{std} are, respectively the intensities of the Ar gas blank and of the element of interest in the calibration standard; C_{std} is the concentration of the element of interest in the standard.

4.3.2.3 Ni analyses of peridotite garnets - SIMS

As mentioned in Chapter 2, SIMS Ni analyses were carried out separately from the rest of the other trace elements, at a high mass resolution. Ni determination is strongly affected by matrix effects associated mainly with Si-O and Si-Si molecules: working curves with distinctively different slopes are produced using reference standards with significantly different Si contents (Fig. 4.5). The NIST standards have high Si contents (72 wt% SiO_2), whereas the secondary garnet standards have relatively lower Si contents (~42 wt% SiO_2). Another standard, a basaltic glass BHVO (~50 wt% SiO_2), and a clinopyroxene from the pyroxenite, JJG1424 (~57 wt% SiO_2), plot on neither the curve formed by the NIST standards nor the curve defined by the secondary garnet standard samples (Fig. 4.5).

Because of the similarity of the peridotite garnet compositions to that of the secondary garnet standards (Table 4.1), SIMS Ni analyses presented here were calculated using the Ni working curve defined by the secondary garnet standards. Solution ICP-MS Ni data were used for the determination of the working curve.

Only core compositions, on 19 of the samples used in the present study, were analysed. The results are presented on Table 4.3 and are an average of two analyses per sample. Ni was analysed with a %RSD of 0.2 to 2.3 % (percentage ratio of the standard deviation of the intensity ratios to the mean of the intensity ratio) for Ni content in the range of ~18 to ~110 ppm.

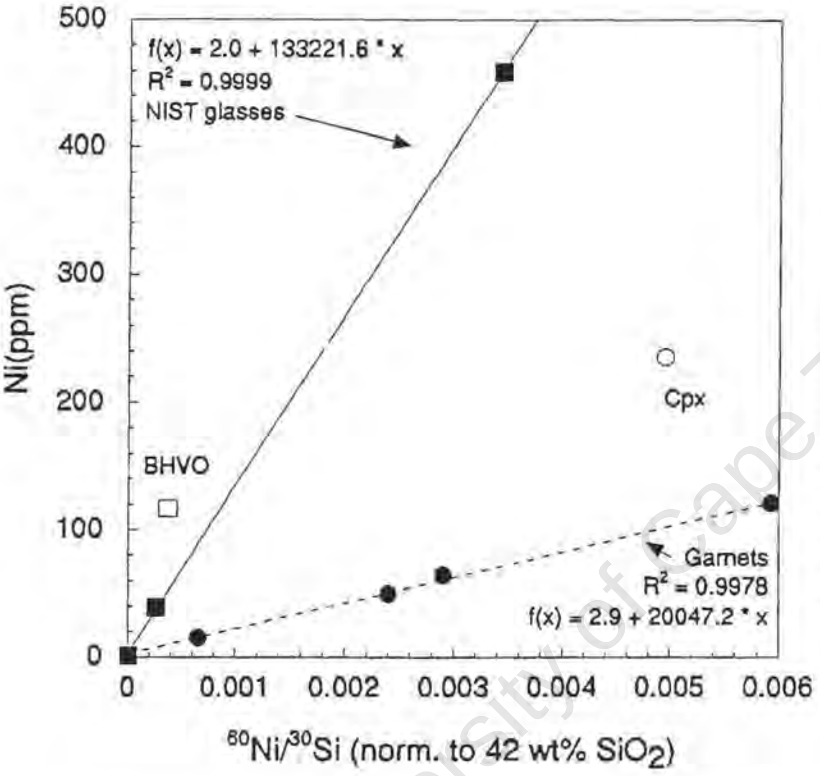

Fig. 4.5. Intensity ratios of Ni and Si isotopes determined by SIMS against Ni content (ppm). The ratios are normalised to 42 wt% SiO_2. The Ni contents of the garnets and the clinopyroxene (cpx) are determined by solution ICP-MS at UCT. The values used for the glass standards are: NIST614, 1 ppm Ni; NIST612, 39 ppm Ni; NIST610, 459 ppm Ni (*certified values*, National Institute of Standards and Technology, USA); BHVO, 117 ppm Ni (Frey and Clague, *unpublished data*). Samples of different matrix compositions produce different working curves.

4.3.3 Zr and Y analyses of peridotite garnets

Most of the garnets analysed are homogeneous with respect to Zr and Y when core and rim compositions are compared and thus averages of data are presented (Table 4.6). However, for two deformed peridotites (from Matsoku) rim and core compositions are significantly different. LBM8 garnets have rims that are enriched in Zr and Y relative to the cores, whereas in LBM16 the core is enriched relative to the rim.

Table 4.6. Y and Zr (ppm) data for the pyrope garnets from the peridotites under study. For PIXE and LA-ICP-MS data are given as averages of several repeat analyses; n = number of analyses. For SIMS the values given are an average of four blocks (section 3.5.2) of data. The errors are 2σ errors.

		Y(ppm)						Zr(ppm)					
		PIXE		LAICPMS		SIMS		PIXE		LAICPMS		SIMS	
		n	Average	n	Average	n	Average	n	Average	n	Average	n	Average
Jagersfontein	J117	6	12.2 ± 0.9	6	20 ± 1	1	19.2 ± 0.6	6	32 ± 1	6	52 ± 3	1	57 ± 2
	JJG1710	6	13.6 ± 1.2	4	13.1 ± 0.6	1		6	33 ± 2	4	31 ± 2	1	
	JJG1716	6	17.8 ± 1.4	6	15.9 ± 0.8	1	16.1 ± 0.5	6	34 ± 2	6	33 ± 3	1	38 ± 1
	JJG1728	6	6.4 ± 2.0	2				6	70 ± 8	2			
	JJG1729	11	20 ± 2	5	21 ± 2			11	50 ± 6	5	50 ± 5		
	JJG1733	12	9.0 ± 1.5					12	14.7 ± 1.2				
	JJG1757		<4ppm	2	2.0 ; 1.8	1	1.8 ± 0.1	6	23 ± 1	2	26 ; 27	1	29 ± 1
	JJG1761	6	4.4 ± 0.8	8	4.3 ± 0.3			6	58 ± 2	8	58 ± 3		
	JJG864	5	12.8 ± 3.7	4	9.5 ± 4.6	1	9.9 ± 0.4	5	85 ± 9	4	67 ± 3	1	84 ± 3
	JJH1	6	4.2 ± 1.3	5	4.2 ± 0.6	1	4.9 ± 0.1	6	14.7 ± 5.6	5	13.6 ± 9.0	1	18.4 ± 0.8
	JJH10	6	18.1 ± 1.2	6	17.8 ± 1.1			6	41 ± 5	6	36 ± 5		
	JJH28	6	13.7 ± 1.2	12	12.7 ± 0.5			6	18.7 ± 1.5	12	16.7 ± 0.4		
	JJH29	6	4.8 ± 0.8	7	6.2 ± 4.0			6	79 ± 8	7	73 ± 26		
	JJH32	12	14.8 ± 0.7	9	13.3 ± 0.4			12	43 ± 5	9	32 ± 2		
	JJH35		<4ppm			1	2.8 ± 0.1	6	8.2 ± 1.1			1	11.3 ± 0.2
	JJH6		<4ppm	3	1.9 ± 0.1			3	18.1 ± 3.2	3	15.4 ± 1.1		
	JJH7	12	17.2 ± 3.0			1	11.3 ± 0.4	12	70 ± 6			1	61 ± 2
	JJH8	6	10.3 ± 1.6	1	6.6	1	10.2 ± 0.4	6	50 ± 3	1	49	1	64 ± 2
	JJH9		<4ppm	3	1.3 ± 0.5				<3.5ppm	3	1.1 ± 0.3		
Matsoku	LBM10	6	4.2 ± 1.1	4	5.8 ± 2.3	1	9.2 ± 0.4	6	47 ± 5	4	64 ± 8	1	9.1 ± 0.4
	LBM16c	3	31 ± 12					3	142 ± 23				
	LBM16r	3	22 ± 5	4	26 ± 5			3	110 ± 20	4	123 ± 12		
	LBM17	6	4.9 ± 2.8	4	3.5 ± 2.1	1	2.3 ± 0.1	6	57 ± 6	4	52 ± 10	1	60 ± 1
	LBM20	9	34 ± 2					9	134 ± 8				
	LBM3		<4ppm					6	33 ± 4				
	LBM30	3	33 ± 6					3	138 ± 15				
	LBM32	9	40 ± 6			1	31 ± 0	9	109 ± 15			1	113 ± 2
	LBM36-2	9	24 ± 3			1	18 ± 1	9	70 ± 4			1	70 ± 3
	LBM36-3	6	25 ± 1	3	19.2 ± 6.4	1	23 ± 1	6	73 ± 5	3	61 ± 22	1	83 ± 4
	LBM6	6	10.0 ± 1.6	4	9.7 ± 0.6			6	28 ± 3	4	27 ± 2		
	LBM8c	6	5.6 ± 2.5	6	2.7 ± 0.3			6	49 ± 13	6	37 ± 6		
	LBM8r	6	22 ± 7	2	20			6	124 ± 13	2	125		
	LBM9	6	6.0 ± 1.2	5	2.9 ± 0.6	1	12.0 ± 0.3	6	55 ± 10	5	35 ± 3	1	102 ± 3

4.3.3.1 Zr and Y contents of peridotite garnets - PIXE

For most of the samples, 2σ precision for Zr abundances of ~14 to ~140 ppm typically ranged between 2 and 12 % relative. The L.O.D. for Zr analyses by PIXE was 4 ppm (calculated by the GeoPIXE software using equation 4.1 at 99% confidence level).

Precision for Y abundances between 12 and 34 ppm ranged from 5 to 13 %. In contrast, at lower concentrations (~4 to 12 ppm Y) the precision deteriorated to between

16 and 32 % relative. The L.O.D. for Zr analyses by PIXE was 3.5 ppm.

4.3.3.2 Zr and Y contents of peridotite garnets - LA-ICP-MS

Where a number of spots could be analysed by laser ablation ICP-MS, Zr data were typically determined with a relative precision of 2 to 13 % for a concentration range of ~15 to ~125 ppm. A similar relative precision was obtained for Y over the concentration range of ~6 to ~22 ppm. At lower concentrations (< 6 ppm Y) the errors increased to up to 50% or more. The L.O.D.'s for LA-ICP-MS Y and Zr analyses were, respectively, 0.07 ppm and 0.13 ppm.

4.3.3.3 Zr and Y contents of peridotite garnets - SIMS

Due to time constraints at the Department of Terrestrial Magnetism and the long analysis times (~40 minute) for trace elements other than Ni, only one point was analysed with the ion microprobe on the core of the garnets. The relative precision based on counting statistics was 2 to 4% for Zr and 3 to 5% for Y.

4.4 Discussion

For most samples mean Ni data values determined by PIXE and LA-ICP-MS are the same when compared using the *Student t-test* at 95% confidence level (see results of the test on Table 4.7; and Fig 4.6). The means differ significantly for only five of the samples at 95% confidence level.

The greatest deviation in the Ni data is for the coarse peridotite J117. PIXE yields a value of 83 ppm Ni, whereas LA-ICP-MS yields a value of 112 ppm Ni for the garnets in this peridotite. A Ni value that is higher than that of the garnets from the rest of the samples was expected for garnets in J117 since this sample has the highest temperature of equilibration (Chapter 6). Thus the LA-ICP-MS data are believed to be more accurate.

Table 4.7. The results of the *Student t-test* (95% confidence level) on the means of the trace element data determined by PIXE and LA-ICP-MS. Yes = the means are equal and NO = the means are not equal at this confidence level.

	Ni PIXE vs LA-ICP-MS	Zr PIXE vs LA-ICP-MS	Y PIXE vs LA-ICP-MS	Ga PIXE vs LA-ICP-MS
J117	NO	NO	NO	NO
JJG1710	Yes	Yes	Yes	NO
JJG1716	Yes	Yes	NO	Yes
JJG1728	Yes	NO	NO	Yes
JJG1729	NO	Yes	Yes	NO
JJG1757	Yes	NO	Yes	Yes
JJG1761	NO	Yes	Yes	NO
JJG864	Yes	NO	Yes	Yes
JJH1	NO	Yes	Yes	NO
JJH10	Yes	Yes	Yes	Yes
JJH28	Yes	NO	NO	NO
JJH29	Yes	Yes	Yes	NO
JJH32	Yes	NO	NO	Yes
JJH6	Yes	NO	Yes	Yes
JJH7	Yes	Yes	Yes	Yes
JJH8	Yes	Yes	Yes	Yes
JJH9	Yes	Yes	Yes	Yes
LBM10	Yes	NO	Yes	Yes
LBM16	NO	Yes	Yes	NO
LBM17	Yes	Yes	Yes	Yes
LBM3	Yes	Yes	Yes	Yes
LBM36-3	Yes	NO	NO	Yes
LBM6	Yes	Yes	Yes	Yes
LBM8	Yes	Yes	Yes	Yes
LBM9	Yes	NO	NO	Yes

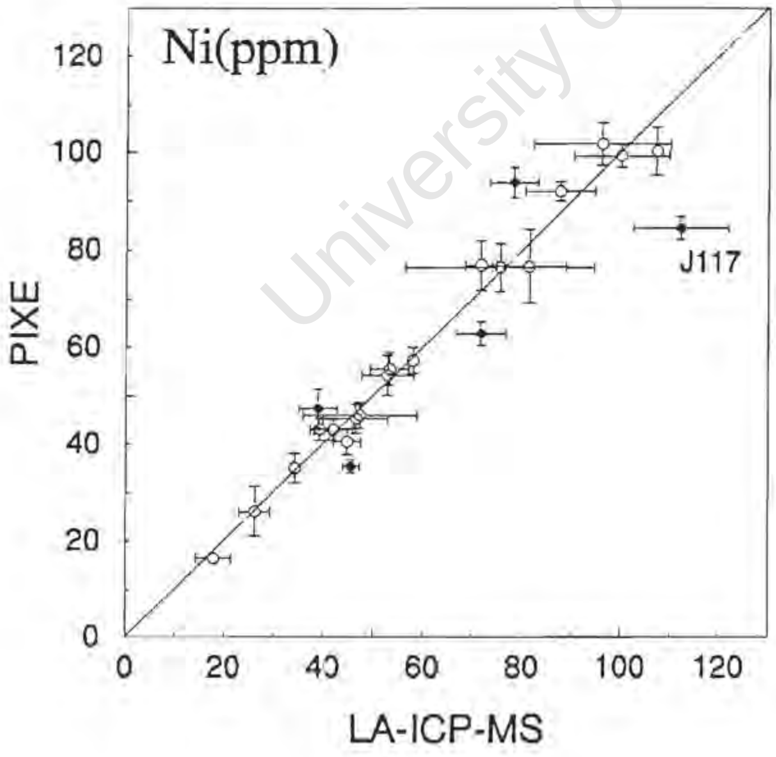

Fig. 4.6. A comparison of Ni data analysed by PIXE and LA-ICP-MS. The open symbols are for data that agree (*student t-test*, 95% confidence level); solid symbols are for data that do not agree at 95% confidence level. The diagonal line is a 1:1 correlation line. The error bars are for 2σ error. J117 is a coarse high temperature (conventional geothermometry) peridotite.

For the majority of the samples Y and Zr data analysed by LA-ICP-MS and PIXE agree within error (Figs. 4.7 and 4.8). In general, the samples that are in disagreement had large errors using either or both of the techniques (Fig. 4.7 and 4.8). Thus, these data might not be acceptable in terms of reproducibility and hence not useful for correlation.

SIMS data are the poorest because, due to time constraints and long analysis times (~10 minutes for Ni and ~40 minutes for multi-element analysis, excluding the time for sample changing), only two analyses for Ni and only one for the other trace elements were carried out on each mineral. The number of samples could have been reduced to allow more analyses per mineral. However, at the time SIMS analyses were carried out it was not clear which technique would give the most reliable data. Thus, in searching for a sufficiently reliable dataset for the present study, as many samples as possible were analysed.

Nevertheless, for half of the samples analysed by SIMS, Ni data are within error of the PIXE Ni data (Fig. 4.9) although they are generally higher than the PIXE Ni data for the rest of the samples. This indicates a good potential for SIMS Ni analysis, which has been avoided in the past due to matrix effects and isobaric interferences. Except for a few samples (including J117), SIMS data for Zr are in agreement with PIXE Zr data (Fig. 4.10). Correlation between SIMS and PIXE for Y data is poor and random (Fig. 4.11). It is uncertain whether this poor correlation is due to factors inherent in the techniques, or whether it has occurred in this particular case, owing to the poor quality of the SIMS data. More SIMS analyses per sample would be required to establish precision and accuracy of these analyses, which in turn might improve correlation of SIMS to the other methods.

Because of the agreement between the PIXE and LA-ICP-MS Ni datasets it should not matter which of the two datasets is used for the evaluation of the Ni geothermometers. However, more samples were analysed by PIXE than by LA-ICP-MS: analyses by the

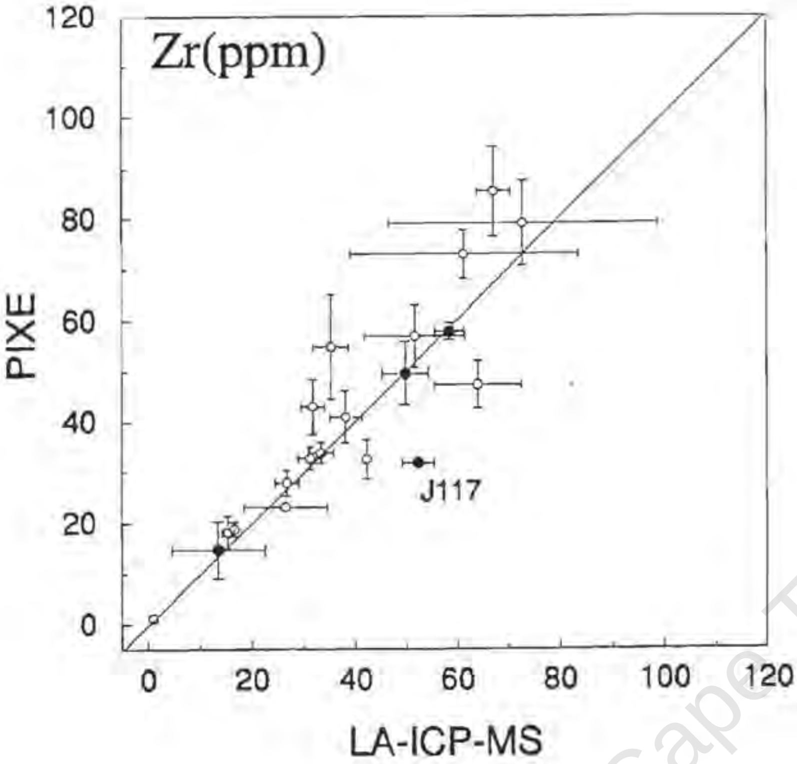

Fig. 4.7. A comparison of Zr data analysed by LA-ICP-MS with data determined by PIXE. The solid symbols are for samples for which Ni data were significantly different using PIXE and LA-ICP-MS (see Fig. 4.6). The diagonal line represents a 1:1 correlation. The error bars represent a 2σ error.

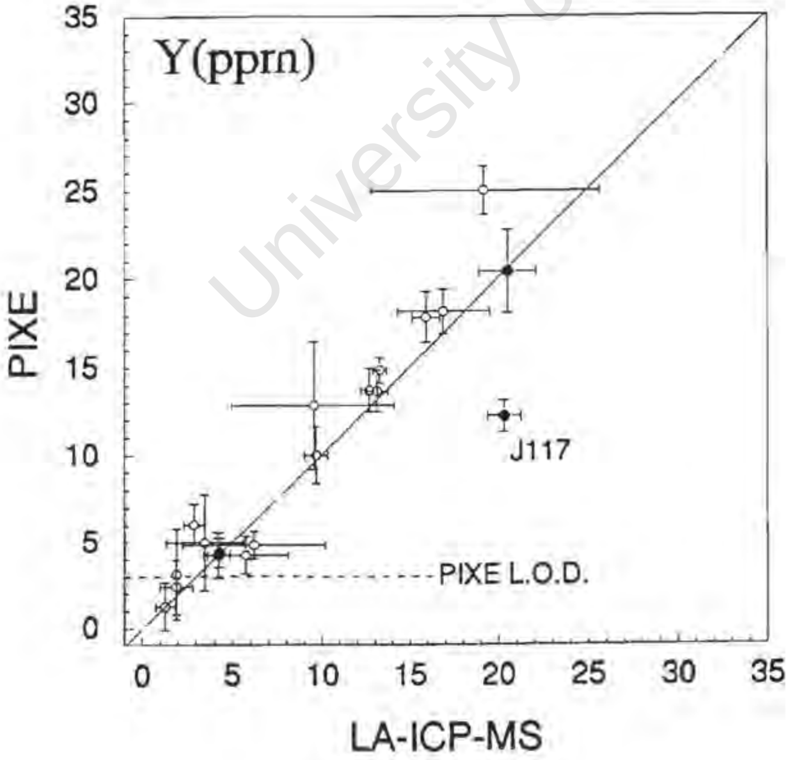

Fig. 4.8. A plot of Y data determined by PIXE and by LA-ICP-MS. The diagonal line, the solid symbols and the error bars are as in Fig. 4.6. The agreement between the two methods is observed even below the lower limit of detection (L.O.D.) of Y in PIXE.

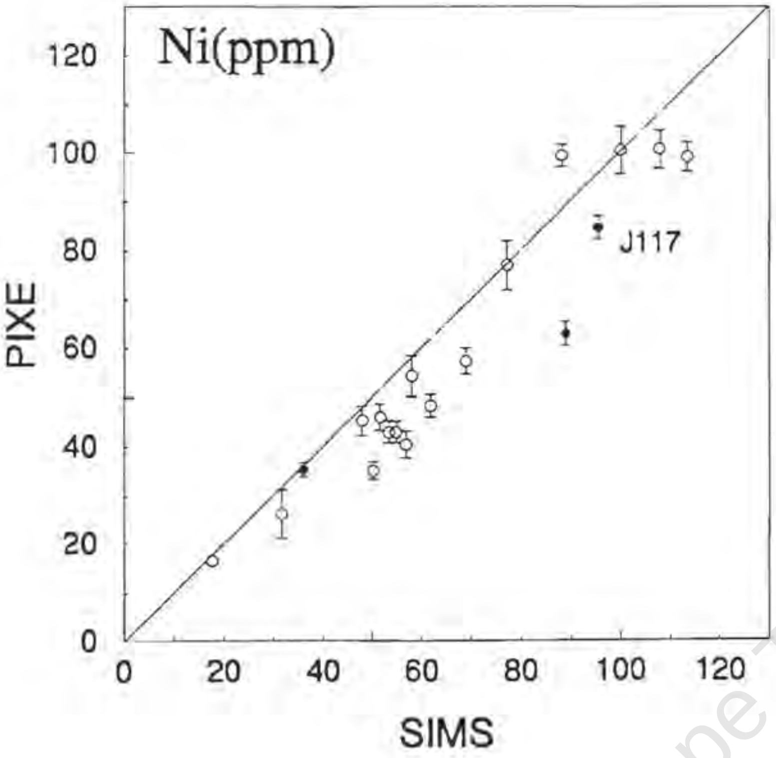

Fig. 4.9. Ni data determined by SIMS plotted against Ni data determined by PIXE. The diagonal line, the solid symbols and the error bars are as in Fig. 4.6. SIMS data are generally lower than PIXE data.

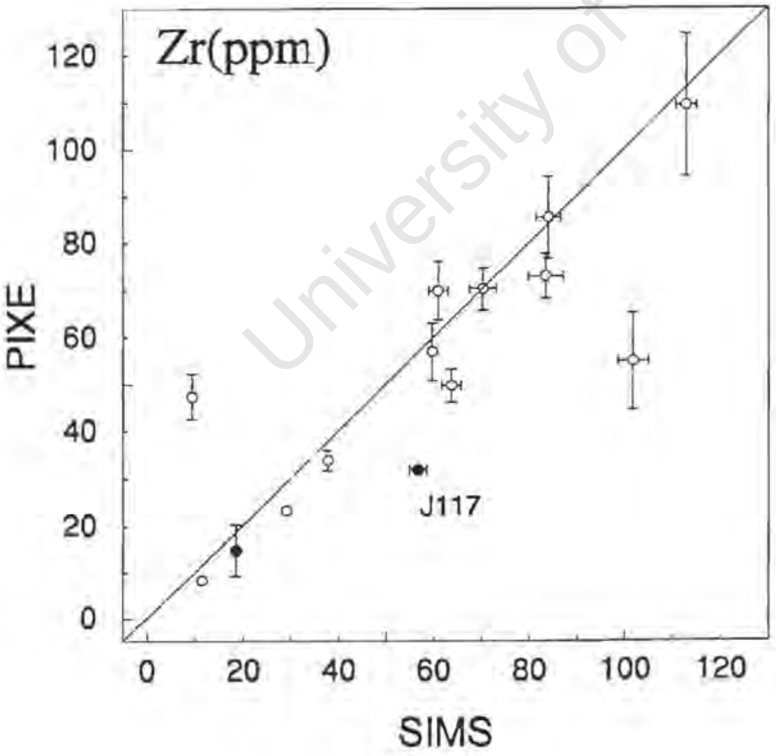

Fig. 4.10. Zr data determined by SIMS plotted against Zr data determined by PIXE. The diagonal line, the solid symbols and the error bars (for PIXE) are as in Fig. 4.6. The error bars for SIMS data are the average of the standard deviations of the means (of counts) for two analyses.

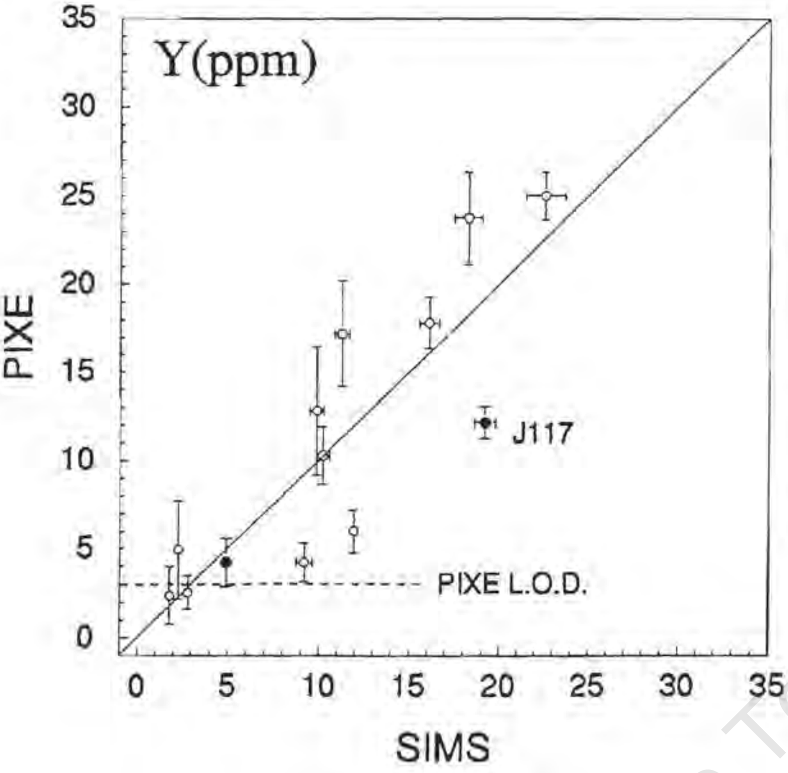

Fig. 4.11. Y data determined by SIMS plotted against Y data determined by PIXE. The diagonal line, the solid symbols and the error bars (for PIXE) are as in Fig. 4.6. The error bars for SIMS data are the average of the standard deviations of the means (of counts) for two analyses. L.O.D. = limit of detection.

laser probe were limited by the size of the garnets. Furthermore, in comparison to the LA-ICP-MS data PIXE data are more precise for all the samples. Therefore, PIXE data were chosen for use in Ni geothermometry for all the samples except the coarse peridotite J117 for which it was decided that the LA-ICP-MS data are more accurate.

The important question for the present study is how much error in temperatures estimated using the Ni geothermometers is due to a 10% error in Ni concentration determination. The answer to this question is illustrated in Table 4.8 for the Ni geothermometer of Ryan *et al.* (1996) (T-Ryan), where temperatures are estimated for a range of Ni concentrations and for the same Ni concentrations minus 10% error. This table shows that 10% error in Ni concentration propagates to only 3 to 4% error in temperature estimates. Therefore, the use of Ni contents determined by PIXE, with 2 to 10 % error, in the evaluation of Ni geothermometers is considered to be valid. However, an error of 4% in temperature could be significant at high temperatures when added to other errors inherent in the Ni geothermometers.

Table 4.8. An illustration of the effect of a 10% error on Ni data on the temperatures calculated using the Ni geothermometer of Ryan *et al.* (1996).

Ni (ppm)	**T^0C(Ryan)**	***Ni(ppm)-10%error***	***T^0 C(Ryan)***	**T^0C(error)**	**T %error**
20	791	*18*	*769*	22	2.8%
40	963	*36*	*934*	30	3.1%
60	1093	*54*	*1057*	36	3.3%
80	1202	*72*	*1160*	42	3.5%
100	1300	*90*	*1252*	48	3.7%
120	1390	*108*	*1337*	53	3.8%

Chapter 5

5. Geothermobarometry *-background*

Abbreviations used:

opx=orthopyroxene; cpx=clinopyroxene; gt=garnet; oliv=olivine; T=temperature in degrees Kelvin; P=pressure in kilobars; R=universal gas constant=8.413; ΔG=change in the Gibbs energy (or the free energy) defined as the sum of the chemical potentials of each component times the number of moles of each for all the components in a phase or a system; ΔH=change in heat content or enthalpy of a phase or system; ΔS=change in entropy of a system or phase (a measure of the degree of disorder or randomness); ΔV=change in volume; ^{0} denotes standard state; M1 and M2 are octahedral sites in pyroxenes; C=CaO, M=MgO, A=Al_2O_3, F=FeO, S=SiO_2, Cr=Cr_2O_3, N=Na_2O; X^i_j = mole fraction of element j in phase i; Ts = Tschermaks

List of geothermometers and geobarometers employed:

Acronym used	*Reaction*	*Reference*
Thermometers		
T-WE77	Diopside-enstatite miscibility	Wells (1977)
T-FB87	Diopside-enstatite miscibility	Finnerty and Boyd (1987)
T-BM85	Diopside-enstatite miscibility	Bertrand and Mercier (1985)
T-BK2px	Diopside-enstatite miscibility	Brey and Kohler (1990)
T-BKCaopx	Ca-in-opx	Brey and Kohler (1990)
T-EG79	Fe^{2+}-Mg exchange, cpx-gt	Ellis and Green (1979)
T-Ai94	Fe^{2+}-Mg exchange, cpx-gt	Ai (1994)
T-KR88	Fe^{2+}-Mg exchange, cpx-gt	Krogh (1988)
T-BE95	Fe^{2+}-Mg exchange, cpx-gt	Berman *et al.* (1995)
T-OW79	Fe^{2+}-Mg exchange, oliv-gt	O'Neill and Wood (1979)
T-HA84	Fe^{2+}-Mg exchange, opx-gt	Harley (1984)
T-Ryan	Ni-Mg exchange, oliv-gt	Ryan *et al.* (1996)
T-Canil	Ni-Mg exchange, oliv-gt	Canil (1994)
Barometers		
P-MG74	gt solubility in opx	McGregor (1974)
P-NG85	gt solubility in opx	Nickel and Green (1985)
P-NI89	gt solubility in opx	Nickel (1989)
P-BK90	gt solubility in opx	Brey and Kohler (1990)
P-Cr	gt solubility in opx	Ryan *et al.* (1996)

5.1 Introduction

A number of mass-balanced reactions can be written in any multiphase rock. These reactions involve components present in the constituent phases. Any or all of these reactions may, in principle, be used to calculate physical properties of the reactions, including pressure and temperature (Wood and Fraser, 1977). Using the exchange reaction between garnet and clinopyroxene as an example:

$$\underset{\text{Pyrope}}{1/3Mg_3Al_2Si_3O_{12}} + \underset{\text{Hedenbergite}}{CaFeSi_2O_6} \Leftrightarrow \underset{\text{Almandine}}{1/3Fe_3Al_2Si_3O_{12}} + \underset{\text{Diopside}}{CaMgSi_2O_6} \qquad 5.1$$

the equilibrium constant K may be defined as:

$$K = \frac{a^{\text{almandine}}_{Fe_3Al_2Si_3O_{12}}{}^{1/3}\; a^{\text{diopside}}_{CaMgSi_2O_6}}{a^{\text{pyrope}}_{Mg_3Al_2Si_3O_{12}}{}^{1/3}\; a^{\text{hedenbergite}}_{CaFeSi_2O_6}} \qquad 5.2$$

where a_i^j is the activity of component *i* in phase *j*. At equilibrium, the standard-state thermodynamic data for reaction 5.1 allow the calculation of K at any pressure and temperature from:

$$\Delta G^0_{P,T} = -RT\ln K \qquad 5.3$$

Taking the standard states of all components to be the pure phases at the pressure and temperature of interest then:

$$-RT\ln K = \Delta H^0_{1bar,T} + T\Delta S^0_T + (1-P)\Delta V^0_{solids} \qquad 5.4$$

assuming that all the phases occur as solids, and thus ΔV^0 is independent of temperature and pressure.

Differentiation of equation 5.4 with respect to pressure at constant temperature (equation 5.5) and with respect to temperature at constant pressure (equation 5.6) gives the following expressions:

$$\left(\frac{\partial \ln K}{\partial P}\right)_T = \frac{-\Delta V^0}{RT} \qquad 5.5$$

$$\left(\frac{\partial \ln K}{\partial T}\right)_P = \frac{+\Delta H_{1bar} + (P-1)\Delta V^0}{RT^2} \qquad 5.6$$

Where the right hand side (RHS) of equation 5.6 is much larger than the RHS of equation 5.5, K is more strongly dependent on temperature than on pressure, and therefore the equilibrium in question is potentially a good geothermometer. A potentially good geobarometer is where the RHS of equation 5.5 is much larger than the RHS of 5.6.

If the phases in equation 5.1 are ideal solid solutions then $a_i^j = X_i^j$, the mole fraction of component i in phase j. Equation 5.2 then becomes:

$$K_{ideal} = \frac{X^{gt}_{Fe} X^{cpx}_{Mg}}{X^{gt}_{Mg} X^{cpx}_{Fe}} = \frac{Fe/Mg^{\,gt}}{Fe/Mg^{\,cpx}} = K_d \qquad 5.7$$

where K_d is the distribution coefficient of Fe and Mg between garnet and clinopyroxene. However, in nature minerals normally occur as non-ideal solid solution systems, and in this case $a = X\gamma$, where γ is the activity coefficient. Thus for non-ideal mineral equilibria K is given as:

$$K_{non\text{-}ideal} = \frac{X\gamma^{\,gt}_{\,Fe}\; X\gamma^{\,cpx}_{\,Mg}}{X\gamma^{\,gt}_{\,Mg}\; X\gamma^{\,cpx}_{\,Fe}} = K\gamma \qquad 5.8$$

Nevertheless, in many equilibria ideality may be assumed and the estimated physical properties may still be reliable. This is due to the following considerations:

- where ΔH^0 and ΔV^0 are very large, the errors due to inadequacies in solid solution assumptions are very small and negligible (Wood and Fraser, 1977); and
- the activity coefficients of most silicates are of similar magnitude and thus cancel each other out in equation 5.8 (Wood and Fraser, 1977).

In summary, the following criteria are useful in the selection of equilibrium reactions that will enable accurate determination of pressure and temperature (Wood and Fraser, 1977):

- accurate standard-state thermodynamic data for the equilibrium reactions must either be available or be estimated from simple system experiments;
- the relationships between activities of the relevant components in complex phases and the compositions of the phases should be as well defined as possible; and
- an equilibrium reaction that has a large value of ΔH is a potential good geothermometer, whereas a good geobarometer should have a large value of ΔV^0.

A substantial number of geothermometers and relatively few geobarometers have been produced. They cannot all be correct, however, since P,T estimates obtained by different methods on the same rock can be in disagreement by hundreds of degrees and tens of kilobars (e.g. Finnerty and Boyd, 1984). These differences in P,T estimates have led to uncertainty in the assessment and interpretation of the results of such geothermobarometry calculations.

Geothermobarometry involves combining at least two subsolidus reactions, one with a strong temperature dependence (a geothermometer) and the other with a strong pressure dependence (a barometer). This combination is used to iteratively derive P,T estimates. On the one hand accuracy of a P,T estimate depends on the position of the intersection of isopleths (isopartition lines) of these reactions in a P,T plot, regardless of the angle of intersection (Finnerty, 1989). It is affected by experimental calibration, effectiveness of counting for compositional effects and extrapolation of results from experimental to natural conditions. Precision of a P,T estimate on the other hand, is affected by the angle of intersection of the isopleths and propagation of analytical uncertainties.

The accuracy of any geothermometer or geobarometer for application to natural mantle assemblages is difficult to assess because there are few invariant reactions that may be used as absolute references for pressure and temperature in typical garnet lherzolites (Finnerty and Boyd, 1987). In addition, almost all geobarometers and geothermometers contain a temperature or pressure correction term respectively, such that any systematic error in either calculated pressure or temperature compounds the error in the other parameter. This is particularly true for available geobarometers.

This chapter provides a brief overview of key geothermometers and geobarometers with the emphasis on those that were chosen for use in this study. Smith (*in prep.*) gives a more comprehensive and recent discussion of geothermobarometry.

5.2 Major Element Geothermobarometry

The minerals that are useful in geothermobarometry of mantle peridotites are olivines, garnets, orthopyroxenes (opx), clinopyroxenes (cpx) and spinels. In general, pairs of minerals in coexistence are used. For accurate determination of P,T estimates, the minerals used must be in internal equilibrium. The evidence for equilibrium includes mineral composition homogeneity, textural equilibrium and isotopic equilibrium between minerals. In addition, agreement between independent[10] geothermobarometers serves as a measure for equilibrium. Rim compositions in minerals showing chemical heterogeneity are more likely to represent equilibrium compositions and are thus used rather than core compositions for P,T estimation.

5.2.1 Pyroxene solvus geothermometry

Several researchers have applied mixing models to the orthopyroxene and clinopyroxene solid solution series to develop temperature formulations based on experimental data for the diopside-enstatite miscibility gap. The basis for this geothermometer is the calibration of the temperature dependence of the reaction between opx and cpx:

$$\underset{\text{opx}}{Mg_2Si_2O_6} \Leftrightarrow \underset{\text{cpx}}{Mg_2Si_2O_6} \qquad 5.9$$

Since the earliest study of this system, undertaken by Davis and Boyd (1966), several experiments on this system have been carried out and various geothermometer formulations have been produced (e.g., Wood and Banno, 1973; Saxena and Nehru, 1975; Lindsley and Dixon, 1976). However, although all these geothermometers are applicable to natural systems, some do not apply very well. The main problem in the application of this system is the lack of knowledge of the Fe^{2+} effect, and to a lesser extent the Al^{3+} effect, on reaction 5.9. In the presence of Fe^{2+}, Ca is strongly decreased in clinopyroxenes and is increased in the coexisting orthopyroxene (Davidson and Lindsley, 1985). The Al^{3+} effect is not very well understood, although recent studies have either found it to be non-existent (Bertrand and Mercier, 1985) or have acknowledged the occurrence thereof, but ignored it on the basis of unavailability of accurate thermodynamic data (Brey and Köhler, 1990).

The first thermodynamically sound attempt to account for non-CMS and non-MAS minor components (Fe, Cr and Mn) in the simple CMS and MAS systems was made by Wood and Banno (1973). These authors developed an empirical approach to take into account the Fe effect on the opx-cpx miscibility gap in natural systems in order to

---

[10] A geothermobarometer is said to be independent of another when the two geothermobarometers are based on different mineral exchange systems.

calculate equilibration temperatures of two pyroxene assemblages. They used the experimental data of Davis and Boyd (1966) at 30 kb to plot $\ln K_d$ vs $1/T$ to formulate a relationship between activity ratio and temperature. An assumption was made that both opx and cpx phases behave as ideal two-site solutions of the $CaMgSi_2O_6$ and $Mg_2Si_2O_6$ components in the formulation of activities. Because of inconclusive experimental data on the effect of Al^{3+} on the solubility of opx in cpx, an assumption was made that Al pyroxene components behaved ideally in multi-component systems of the pyroxene phases.

In the determination of $\ln K_d$, Wood and Banno (1973) assumed a random distribution of Fe^{2+} and Mg^{2+} over the M1 and M2 sites in both clino and orthopyroxene after removing other minor ions (Ca, Na and Mn^{2+} in M1, and Al, Cr and Ti^{4+} in M2). This assumption was made after these authors found no difference between ratios calculated from site occupancy calculations using appropriate values of the ΔG^0 of equation 5.9. The geothermometer from this work is reported to reproduce experimental data to within $\pm 60^0$ C (Wood and Banno, 1973). The pressure effect for this geothermometer, as observed by Davis and Boyd (1966), was neglected since the pressure increase from 1 bar to 30 kb reportedly resulted in a temperature change of not more than 50^0 C (Wood and Banno, 1973).

Lindsley and Dixon (1976) determined the diopside-enstatite miscibility gap in the CMS system by combining their reversed experimental data with those that already existed (Mori and Green, 1975). These authors also found that the enstatite component in the cpx varies with temperature. However, they noticed that the enstatite solvus was so steep that small compositional ranges corresponded to unacceptable temperature uncertainties of $\pm 100^0$ C. Moreover, the Ca content of cpx increased with an increase in pressure, adding a further uncertainty of $\pm 100^0$ C for a 10 kb pressure change at high temperatures (Lindsley and Dixon, 1976). Although the temperature range (850 to 1400^0 C) of this work might be applicable to natural lherzolites, this work was unfortunately done at comparatively low pressures (mainly at 15 and 20 kb but also at 5-35 kb), and thus did not cover the high-pressure range of garnet peridotites. In addition, and more importantly, the Fe effect on the opx-cpx solid solution was not taken into account.

Nickel and Brey (1984) and Brey and Hunt (1984) developed a much better constraint of the pressure effect on the diopside-enstatite miscibility gap, using thirteen reversed experiments at pressures up to 60 kb. Finnerty and Boyd (1987) combined these data with those at lower pressures and fitted the whole dataset to the geothermometer formulation of Lindsley and Dixon (1976) to obtain a pyroxene solvus geothermometer (T-FB87) with an experimentally constrained pressure effect.

Wells (1977) fitted available experimental data in the CMAS system for the diopside-enstatite miscibility gap to a linear relationship between $\ln K_d$ and 1/T using the ideal two-site mixing model of Wood and Banno (1973) to estimate the activity of $Mg_2Si_2O_6$ in opx and cpx. To calibrate the Fe dependence of $\ln K_d$, Wells (1977) used the temperature composition for 43 multicomponent two-pyroxene assemblages. From this calibration it was found that the Ca content of the cpx phase decreased progressively with an increase in Fe content at constant pressure and temperature. Experimental data were reported by Wells (1977) to indicate that for Al_2O_3 contents in cpx of up to 12 wt %, $\ln K_d$ is not related to the amount of Al in the pyroxenes. Thus, to ensure applicability of the geothermometer produced to both Al-bearing and Al-free pyroxenes calibration data used were for cpx with Al_2O_3 concentration of less than 10 wt %. This geothermometer (T-WE77) reproduced experimental data available at the time to within 70^{0}C and is applicable over a temperature range of 800 to 1700^{0}C (Wells, 1977). Temperature estimates derived using T-WE77 deviate markedly from temperature estimates made using the geothermometer of Wood and Banno (1973) for naturally equilibrated Mg-rich opx-cpx assemblages. Wells (1977) attributed these differences to the inapplicability of the latter geothermometer to Mg-rich pyroxenes. Similarly to the suggestion by Wood and Banno (1973), the pressure effect on equation 5.9 was neglected over the pressure range of 1 bar to 40 kb.

Bertrand and Mercier (1985) used data for simple synthetic systems (CMS and MAS) together with data obtained from reversed experiments on natural samples (Akella and Boyd, 1973; Akella, 1976; Mori and Green, 1978) to provide a reliable method of temperature for natural lherzolites, which takes into account the effect of minor elements on equation 5.9. This was achieved by using an iterative procedure in which components present in significant amounts in pyroxenes were added one by one to the simplest system (CMS) to produce a solution model for the opx-cpx solid solution. The resulting model was then tested against the natural system data not used in the calibration of the model. Components that made no significant change to the model of the simplest system were deleted. The next component occurring in significant amounts was added, and the resulting model was tested again. The following results were found from this work:

- *Poor correlation between calculated temperature (T_{calc}) and experimental temperature (T_{expt}) for the CMS system.* This showed that the thermometer developed for the CMS is not applicable to the natural system without appropriate corrections for minor elements.
- *No significant difference between CMS and CMAS experiments.* Thus, no correction for Al on the reaction in equation 5.9 was applied.
- *Slight improvements in the correlation between the synthetic and the natural systems when the theoretical correction for Na (NCMS system) for both pyroxenes was applied.*
- *The best correlation between data for synthetic and the natural systems* was after the inclusion of the Fe correction (CFMS system) in clinopyroxene, in addition to the Na correction. The Na correction is required to account for the fact that Na competes with Ca for substitution with Mg in the M2 site of pyroxenes.

This work produced an equation for temperature calculation (T-BM85) for the CMS system with the empirical correction for Fe in cpx and the theoretical correction for Na in both pyroxenes. The solution model was obtained from data in the P,T range of 810 to 1500^{0}C and 0 to 10 kb, and was reportedly successfully (Bertrand and Mercier, 1985) tested on natural system data with an uncertainty of 2% (corresponding to 20 to 30^{0}C) in the P,T range 950 to 1500^{0}C and 30 to 40 kb.

Brey *et al.* (1990) carried out reversed experiments on natural lherzolitic compositions, in the P,T range from 10-60 kb and 900-1400^{0}C. Such a range in temperature and pressure was selected to make extrapolations unnecessary when dealing with natural systems. In addition, these authors used single-crystal olivines as sample holders to circumvent the Fe-loss problem, which occurs in experiments where metal capsules are used. Opx and cpx compositions were strictly reversed with respect to Al, Cr and Na (cpx) contents and their mutual amounts of enstatite and diopside components. An influence of Na on Ca solubility in cpx was found, similar to the findings of Bertrand and Mercier (1985). Garnet compositions were reversed with respect to Ca, Al, Cr, Ti and Mn. Ca (except in the CMAS system) in garnet was found to be strongly temperature dependent in the natural system.

These experimental data offered an opportunity for simultaneous testing of many geothermobarometers based on different exchange reactions. Brey and Köhler (1990) tested most of the published geothermometers relevant to four-phase peridotites for their ability to reproduce the experimental conditions of Brey *et al.* (1990). Where a systematic discrepancy in either pressure or temperature was observed the geothermobarometer tested was rejected. These authors produced two new geothermometers, a pyroxene solvus geothermometer (T-BK2px) and a Ca-in-orthopyroxene geothermometer (T-BKCaopx). However, they suggested that the latter geothermometer be used with caution because they were not able to devise a reasonable correction scheme for the influence of Na on Ca content of opx from natural mineral compositions.

In formulating T-BK2px Brey and Köhler (1990) adopted the use of $(\ln K_d)^2$ instead of $\ln K_d$ to allow the treatment of the CMS system as ideal. This approach stemmed from the work of Ehrenberg (1979) who found that $\ln K_d$ for reaction 5.9 has a curved relationship with 1/T for the CMS experiments whereas the relationship is linear for $(\ln K_d)^2$ and 1/T. Brey and Köhler (1990) also found the same relationship for the CMAS and CMASCr systems. These authors then fitted midpoints of the experimental brackets for the CMS, CMAS, CMASCr systems and for their natural system to the following equation:

$$T = (a + bP)/(c + (\ln K_d)^2) \qquad 5.10$$

where $K_d = \frac{(1-Ca^{M2})^{cpx}}{(1-Ca^{M2})^{opx}}$ for the synthetic systems, based on the assumption that Ca is restricted to the M2 site of pyroxenes and that $\frac{Mg^{M1}_{cpx}}{Mg^{M1}_{opx}} \approx 1$ (Nickel and Brey, 1984;

Bertrand and Mercier, 1985); a, b and c are fit parameters and are different for each system. For the natural system $K_d = K_d^* = (1 - Ca^*)^{cpx}/(1 - Ca^*)^{opx}$, where $Ca^* = Ca^{M2}/(1\text{-}Na^{M2})$, the Na theoretical correction of Bertrand and Mercier (1985). Brey and Köhler (1990) found that T_{calc} vs T_{expt} was greatly improved by the Na correction, similarly to what was observed by Bertrand and Mercier (1985) with the experimental data of Mori and Green (1978).

The resulting equations for the systems whose data were fitted to equation 5.10 showed the following:

- *Large differences between the equations derived for the CMS and CMAS systems.* Brey and Köhler (1990) suggested that the reason for this difference was the invalidity of K_d (equation 5.10) for the CMAS system. These authors pointed out that contrary to the assumption of Bertrand and Mercier (1985) that Al values in both pyroxenes are about the same, these values are identical only at certain P,T condition: Ca is always lower in orthopyroxene in the presence of Al, but is either lower or higher in clinopyroxene depending on pressure and temperature (Nickel *et al.*, 1985). However, no Al correction could be applied because of a limited number of experiments on the Al-effect (Brey and Köhler, 1990). Therefore, Brey and Köhler, (1990) assumed that the equation derived for the CMS system is applicable to the CMAS system.
- *A close similarity between the equations derived for the CMS and CMASCr systems.*
- *Differences between the CMS and the natural systems.* After establishing that a Cr correction is not required and deciding to ignore the Al effect, the only plausible cause for this difference had to be due to the Fe effect on equation 5.9. Brey and Köhler (1990) used an empirical correction on the equation derived for their experimental synthetic system to correct for the Fe effect. The geothermometer produced is reported by (Brey and Köhler (1990) to have produced the experimental data to $\pm 15^{0}$ C (1σ). No systematic dependence on P and T of this equation was observed. The major difference between T-BK2px and T-BM85 is the Fe correction: In T-BK2px the correction for Fe is applied to both pyroxenes whereas in T-BM85 this correction is applied only to clinopyroxenes. Bertrand and Mercier (1985) assumed the variation of Ca content with Fe in orthopyroxenes is negligible due to the small amounts of Ca present.

5.2.2 Fe^{2+}-Mg geothermometry

Fe^{2+}-Mg exchange geothermometers are based on the partitioning of these elements between coexisting garnet and olivine (O'Neill and Wood, 1979; O'Neill 1980), garnet and clinopyroxene (e.g., Mori and Green, 1978; Ellis and Green, 1979; Krogh, 1988; Berman *et al.*, 1995), and garnet and orthopyroxene (e.g., Mori and Green, 1978; Harley, 1984). In addition to other factors applicable to all geothermometers, these geothermometers are limited by the uncertainty of Fe^{3+}/Fe^{2+} ratios in these minerals.

5.2.2.1 Garnet-Cpx Fe^{2+}-Mg geothermometry

This geothermometry is based on the exchange reaction in equation 5.1 and its K_d is as in equation 5.2.

The gt-cpx geothermometer of Ellis and Green (1979) (T-EG79) has, in the past, been a major method applied in kimberlite xenolith studies. This geothermometer was formulated from experimental data in the CFMAS system at 24 to 30 kb and 750 to 1300^{0}C. The experiments reportedly showed that K_d for reaction 5.1 is dependant on the Ca content of garnet and is independent of Mg# (100Mg/(Mg+Fe)) of both garnet and cpx (Ellis and Green, 1979). The pressure effect on reaction 5.1 was evaluated and quantified using the molar volume data of cpx (Rutstein and Yund, 1969) and garnet (Takahashi and Liu, 1970). This evaluation showed a decrease in molar volume for reaction 5.1 and thus a pressure effect. The K_d for reaction 5.1 was determined as a function of P, T and X_{Ca}^{gt} (=[Ca/(Ca+Mg+Fe)]$_{gt}$) to produce a geothermometer (T-EG79) capable of reproducing P,T estimates of the experiments that are within ±5% (corresponding to 30 to 70^0) (Ellis and Green, 1979) of the experimental data of Hensen (1973); Råheim and Green (1974a and b); Akella (1976); and of Mori and Green (1978) based on experiments in the P,T of 15 to 45 kb and 600 to 1450^{0}C.

Recently, in most mantle studies the geothermometer of Krogh (1988) (T-KR88) has been used. This author used available experimental data (Råheim and Green, 1974; Mori and Green, 1978; Ellis and Green, 1979; Powell, 1985) from experiments at 600 to 1300°C and 30 kb on the partitioning of Fe^{2+} and Mg in reaction 5.1 to construct an expression for a garnet-cpx geothermometer (T-KR88). He used a curvilinear[11] correction for the effect of X_{ca} (Ca/Ca+Mg+Fe+Mn) on $\ln K_d$ in garnet rather than a purely linear correction (e.g. Ellis and Green, 1979). T-KR88 reportedly (Krogh, 1988) generally reproduced the experimental data to within ±50°C.

Ai (1994) used his experimental data (Ai, 1992) in conjunction with published data to evaluate and improve the garnet-cpx geothermometry. The experimental conditions of the published data used ranged from 10 to 60 kb and 600 to 1500°C and the experiments of Ai (1992) were carried out at 25 to 38 kb and 1200 to 1500°C. Ai (1994) basically followed the method of Krogh (1988) but added a Mg# ($100Mg/(Mg+Fe^{2+})$) term, for the correction of this terms negative linear relationship to $\ln K_d$ (Pattison and Newton, 1989). The geothermometer produced (T-AI94) is reported (Ai, 1994) to have reproduced experimental data to within ±100°C and produced temperature estimates that are similar to both temperatures derived using T-KR88 and T-EG79 at temperatures above 1200°C. Below 1200°C T-Ai94 gave temperature estimates that are lower than the estimates made by T-KR88 and T-EG79. Smith (*in prep.*) notes that T-Ai94 has a strong pressure effect, and overestimates temperatures at high pressures.

Berman *et al.* (1995) noted that of the available studies on the Fe^{2+}-Mg exchange between garnet and clinopyroxene, the experiments of Pattison and Newton (1989) were the only investigations that were designed to obtain compositional constraints on the exchange reaction in equation 5.1 using natural crystalline starting materials from a wide range of bulk compositions. This was done to avoid the potential of formation of metastable compositions from rapid crystallisation of glass, which is a problem in experiments utilising synthetic glass materials. However, the geothermometer devised by Pattison and Newton (1989) produced temperatures that are significantly lower than previous calibrations, and which clustered at or below the low temperature limit imposed by other geothermometers, petrogenetic grids and 'petrogenetic intuition'

---

[11] i.e. fitting data with both a quadratic and a linear expression.

(Berman *et al.*, 1995).

In a two part study (Aranovich and Pattison, 1995; Berman *et al.*, 1995) the phase equilibrium data and the geothermometer of Pattison and Newton (1989) were reassessed by reanalyses of 69 of the 125 experimental runs for these data and by thermodynamic analysis of the new data. In the reanalyses wavelength dispersive spectroscopy was used rather than the energy dispersive spectroscopy used by Pattison and Newton (1989). In addition, backscattered secondary electron imaging was used for proper selection of analytical spots on the sample runs. The thermodynamic analysis involved derivation of thermodynamic parameters and activity-composition expressions for reaction 5.1 from the new data, and the testing of the garnet buffering[12] technique used by Pattison and Newton (1989).

From this reassessment a new geothermometer based on the variation of the Fe^{2+}-Mg exchange between garnet and clinopyroxene with temperature was developed, using the new thermodynamic properties. This geothermometer yielded temperatures that are 70-200°C higher than those obtained using the geothermometer of Pattison and Newton (1989) (Berman *et al.*, 1995). However, Berman *et al.* (1995) noted that their thermodynamic data and geothermometer were provisional and that a larger experimental dataset capable of further constraining the thermodynamic properties of garnet and cpx was needed.

5.2.2.2 Garnet-Olivine Fe^{2+}-Mg geothermometry

The distribution of Fe^{2+} and Mg between garnet and olivine is based on the exchange reaction:

$$\underset{\text{Fayalite}}{3Fe_2SiO_4} + \underset{\text{Pyrope}}{2Mg_3Al_2Si_3O_{12}} \Leftrightarrow \underset{\text{Fosterite}}{3Mg_2SiO_4} + \underset{\text{Almandine}}{2Fe_3Al_2Si_3O_{12}} \qquad 5.11$$

---

[12] The technique, first used by Ferry and Spear (1978) for Fe-Mg exchange between garnet and biotite, is based on the concept of garnet buffering and involves the insertion of an overwhelming abundance of garnet relative to the other exchanging phase. This effectively fixes the bulk composition of the system close to that of the garnet composition, allowing the change in composition occurring in the other exchanging phase to be easily monitored.

The garnet-olivine geothermometer (T-OW79) of O'Neill and Wood (1979), corrected by O'Neill (1980), has received wide usage partly because it can be applied to both harzburgitic and lherzolitic assemblages. Smith *(in prep)* has attributed the success of this geothermometer in temperature derivation to the simplicity of the olivine solid solution. The geothermometer resulted from the reversed experiments of O'Neill and Wood (1979), in the FMAS system, at 30 kb and temperatures ranging from 900 to 1400^{0}C. These authors found that $\ln K_d$ of equation 5.11 was a function of temperature, Mg content of olivine and Ca content of garnet. They also found that the simplest kind of non-ideal solution model fitted experimental data adequately and that the use of more complex models did not markedly improve the fit to data.. The simplest model was thus adopted to produce a geothermometer that is most sensitive for temperatures that are below 1300^{0}C to within ±60^{0}C of the experimental value and composition regions where K_d is substantially greater than 1 (O'Neill and Wood, 1979). The pressure effect of equation 5.11 was found to raise the calculated temperature by between 3 and 6^{0}C per kilobar.

5.2.2.3 Garnet-Opx Fe^{2+}-Mg geothermometry

The distribution of Fe^{2+} and Mg between garnet and opx is described by the following exchange reaction:

$$\underset{\text{Pyrope}}{1/3Mg_3Al_2Si_3O_{12}} + \underset{\text{Ferrosillite}}{1/2Fe_2Si_2O_{12}} \Leftrightarrow \underset{\text{Almandine}}{1/3Fe_2Al_2Si_3O_{12}} + \underset{\text{Enstatite}}{1/2Mg_2Si_2O_{12}} \qquad 5.12$$

The mostly used garnet-opx geothermometer is that of Harley (1984) (T-HA84) calibrated from experimental data in the FMAS and CFMAS systems at 5 to 30 kb and 800 to 1500^{0}C. Opx was regarded as an ideal phase, and the effects of Ca content of garnet on K_d were attributed to non-ideal Ca-Mg interactions in garnet. The molar volume data (Matsui *et al.*, 1968; Turnock *et al.*, 1973) were used to calculate ΔV^0 for reaction 5.12 in order to quantify the pressure effect on this equation. Therefore, the expression for T-HA84 incorporated the pressure and composition effects. Harley (1984) pointed out that this geothermometer is limited by large relative errors in experimental and natural rock data used. In addition, the fact that the variation of temperature with K_d is very small makes the accuracy of this geothermometer susceptible to minor element variations (Mn, Cr, Fe^{2+}). However, this geothermobarometer is reported to have reproduced the experimental data in the CFMAS to within ±40°C (Harley, 1984). Brey and Köhler (1990) noted that, based on the tests against the experimental data of Brey *et al.* (1990), T-HA84 overestimates temperatures at low temperatures and underestimates temperatures at high temperatures.

5.2.3 Garnet-opx geobarometry

In most cases garnet-opx geobarometry is based on the pressure-sensitive solubility of garnet in orthopyroxene coexisting with garnet defined by the following exchange reaction:

$$\underset{\text{Enstatite}}{Mg_2Si_2O_6} + \underset{\text{MgTs}}{MgAl_2SiO_6} \Leftrightarrow \underset{\text{garnet}}{Mg_3Al_2Si_3O_{12}} \qquad 5.13$$

Such a barometer was first developed by MacGregor (1974) in a study where he presented experimental data on the Al solubility orthopyroxene in the pressure range of 5 to 40 kb and temperature range of 900 to 1600°C in the simple MAS system. The experimental data showed a large enough pressure-effect to be used as a barometer for garnet peridotites. These experiments were however not reversed and more importantly the geobarometer (P-MG74) produced from these experiments has a substantial temperature effect (Finnerty and Boyd, 1984).

Wood and Banno (1974) attempted to improve this geobarometry by using experiments in the FMAS and CFMAS systems to account for the influence of Ca and Fe on reaction 5.13. These experiments were carried out at over a P,T range of 8 to 30 kb and 800 to 1250°C. The geobarometer developed from this work was reported to reproduce experimental data to within 2 to 3 kb. However, Finnerty and Boyd (1984) noted that the correction schemes used in this geobarometer served to decrease precision without any improvement in accuracy.

In order to refine garnet-opx geobarometry, Nickel and Green (1985) studied the influence of Cr on reaction 5.13. This study produced a geobarometer (P-NG85) based on the solubility of garnet in enstatite, formulated for a multi-component system which most closely approaches that of the natural garnet lherzolite. P-NG85 takes into consideration the presence of minor amounts of Ti, Cr, Na and Mn in both orthopyroxene and garnet, and is based on experiments in the systems CMAS, FMAS, CFMAS, and CMASCr in the pressure range of 10 to 35 kb. This geobarometer reportedly reproduced experimental data to within ±3 kb (Nickel and Green, 1985).

Nickel (1989) used phase equilibria experiments in the CMASCr system at 22.5 to 35 kb and 900 to 1400^{0}C to develop a geobarometer based on the pressure dependence of the Cr solubility in opx coexisting with garnet. This approach is based on the reaction similar to reaction 5.13:

$$\underset{\text{enstatite}}{2Mg_2Si_2O_6} + \underset{\text{MgCrTs}}{2MgCrAlSiO_6} \Leftrightarrow \underset{\text{pyrope}}{Mg_3Al_2Si_3O_{12}} + \underset{\text{knorringite}}{Mg_3Cr_2Si_3O_{12}} \qquad 5.14$$

K_d for this reaction is given by:

$$K_d = \frac{(X_{Mg}^{gt})^6 (X_{Al}^{gt})^2 (X_{Cr}^{gt})^2}{(X_{Mg}^{M2-opx})^4 (X_{Mg}^{M1-opx})^2 (X_{Cr}^{M1-opx})^2} \qquad 5.15$$

Nickel (1989) used the expressions for non-ideal mixing of Ca and Mg on the M2 site and of Mg, Al and Cr on the M1 site of opx (Nickel and Brey, 1984; Brey *et al.*, 1986) to fit values for ΔH^0, ΔS^0 and ΔV^0 for reaction 5.14. The geobarometer expression (P-NI89^1) from this work reportedly adequately reproduced the experimental data in the CMASCCr system (Nickel, 1989). However, Nickel (1989) noted that P-NI89^1 has, amongst other factors, a large number of parameters with large magnitudes and requires a correction for the Fe influence on the mixing of components in garnet and opx. Moreover, some terms in the expression of K_d (equation 5.15) used for P-NI89^1 are raised to the power of 4 and 6. This makes P-NI89^1 prone to analytical uncertainties. To calibrate a simpler geobarometer expression Nickel (1989) used a relationship of pressure and Cr contents of garnet and opx at constant temperature, and the temperature sensitivity of the pressure-dependent X_{Cr}^{gt}/X_{Cr}^{opx} to empirically develop an expression for pressure calculation (P-NI89^2).

Both equation P-NI89^1 and P-NI89^2 reproduced experimental data to within ±3 kb (Nickel, 1989). However, P-NI89^2 is simpler and is said to be applicable to natural garnet lherzolites for Cr concentrations that are higher than 2 wt% and 0.18 wt% respectively in garnet and opx (Nickel, 1989).

Brey and Köhler (1990) tested the aforementioned geobarometers (see section 5.4) against the experimental data of Brey *et al.* (1990) (section 5.2.1) and recognised a need for calibration of a new barometer which is capable of reproducing experimental conditions for all available systems, and over the whole pressure range applicable to natural peridotites. A garnet-opx geobarometer applicable to these conditions, P-BK90, was calibrated using available experimental data for the main systems [MAS from Gasparik and Newton (1984); CMAS from Perkins and Newton (1980), Nickel *et al.*(1985) and Brey *et al.* (1986); FMAS from Kawasaki and Matsui (1983), but only experiments with $(Mg/Mg+Fe)^{opx} \geq 0.5$; CMASCr from Nickel (1989)]. P-BK90 has a simple quadratic form and is reported to have reproduced the natural systems experiments of Brey *et al.* (1990) to within ±2.2 kb (1σ) by Brey and Köhler (1990).

5.3 Single Mineral Geothermobarometry

5.3.1 Ni geothermometry

Griffin *et al.* (1989) and Ryan *et al.* (1996) developed single garnet geothermometry to obviate the need for coexisting mineral phases in the estimation of equilibration P,T conditions of mantle peridotites. This geothermometry is based on the Ni-Mg exchange between garnet and olivine in the reaction expressed as follows:

$$\underset{\text{garnet}}{2Mg_3Al_2Si_3O_{12}} + \underset{\text{olivine}}{3Ni_2SiO_4} \Leftrightarrow \underset{\text{garnet}}{2Ni_3Al_2Si_3O_{12}} + \underset{\text{olivine}}{3Mg_2SiO_4}. \qquad 5.16$$

5.3.1.1 Empirical calibration of the Ni geothermometer

Using proton microprobe analyses of minerals in natural garnet peridotites Griffin *et al.* (1989) showed that the partitioning of Ni between Cr pyrope garnet and olivine is strongly temperature-dependent (temperature based on conventional geothermometers). The analyses also showed that the range of Ni contents in peridotite olivine is relatively small compared to that in peridotite garnet, with the Ni content of olivine being of limited range, 3000±300 ppm and that of garnet ranging from <10 to 120 ppm (Griffin *et al.*, 1989). Based on these data these authors calibrated a geothermometer based on the Ni content of peridotitic garnets.

The samples used in the Griffin *et al.* (1989) calibration covered a wide range of composition and texture, and were from several South African kimberlites, the Garnet Ridge diatreme on the Colorado Plateau (southwest USA) and the Argyle diamonds (garnet-olivine inclusion pairs). The temperature estimates used for correlation with the Ni contents were estimated using T-FB87 and P-MG74. Where T-FB87 was not applicable (for clinopyroxene-free samples) temperature estimates were made using T-OW79.

Griffin et al. (1989) found that garnet accepts more Ni into its structure as temperature increases and that the relationship between log K_d (where K_d = ppm Ni in garnet/ppm Ni in olivine) and 1/T is linear over a temperature range of ~700°C. Assuming an olivine Ni concentration of 3000 ppm in the calculation of K_d these authors formulated a Ni geothermometer of the following form:

$$T(K) = \frac{1000}{-0.435\log_{10}(ppmNi^{gt}/30) + 0.83} \qquad 5.17$$

This geothermometer is reported to have reproduced estimated temperatures (T-FB87 and T-OW79) with an average error of ± 4%, corresponding to ± 50°C (Griffin *et al.*, 1989). The geothermometer appeared to be applicable to a wide range of single garnet compositions, known or assumed to be in equilibrium with olivine. Griffin *et al.* (1989) pointed out the need of a larger sample suite to refine the geothermometer calibration and to ensure applicability to samples from an even wider range of composition and from different geotherms (i.e., pressure conditions).

Ryan *et al.* (1996) used an expanded database involving analyses of more than 100 harzburgites and lherzolites to refine the Ni geothermometer of Griffin *et al.* (1989).

The samples were xenoliths from kimberlites and other volcanic rocks from a range of pressure-temperature conditions and a range of geotherms (i.e., typical cratonic geotherms, elevated geotherms and intermediate geotherms). In this recalibration of the empirical Ni geothermometer only T-OW79 was used for temperature estimation. This was done in order to extend the applicability of the Ni geothermometer to harzburgite compositions, to allow the testing of the reliability of the Ni geothermometer for low-Ca and Ca-saturated garnets.

The refined Ni geothermometer (T-Ryan) is defined by the following expression:

$$T(K) = \frac{1000}{1.506 - 0.189 \ln ppmNi^{gt}} \qquad 5.18$$

Ryan *et al.* (1996) reported that this geothermometer reproduced T-OW79 estimates to within ± 50°C and lowers the temperatures estimated by the calibration of Griffin *et al.* (1989) by ~35°C at low temperatures and by ~90°C at high temperatures.

One possible source of uncertainty in the T-Ryan temperature estimates could be due to the fact that it was calibrated using temperatures derived using T-OW79. O'Neill and Wood (1979) noted that T-OW79 reproduced their experimental data to within ±60°C. However, Brey and Köhler (1990) reported that T-OW79 only reproduced the data of reversed experiments of Brey *et al.* (1990) to within ±113°C. Moreover, more recently, Canil and O'Neill (1996) have noted that differences in T-OW79 temperature estimates can exceed 200°C depending on whether Fe^{3+} content of the phases concerned, garnet in particular, is taken into account or all Fe is assumed to occur as Fe^{2+}. Clearly these errors would compound the ±50°C uncertainty reported by Ryan *et al.* (1996) for T-Ryan.

Another possible contribution to error might be inaccurate determination of Ni abundances in garnet used for the calibration of T-Ryan at levels of tens of ppm. The accuracy of PIXE data reduced using the GeoPIXE software package has been demonstrated in Chapter 4 by comparison to other techniques, including PIXE with data reduced by the GUPIX method. Ni data used by Ryan *et al.* (1996) for the calibration of T-Ryan were reduced by the GeoPIXE software. Therefore, it is considered that errors due to the quality of Ni data are negligible. Moreover, in a study to test the accuracy of the GUPIX software methodology of reducing PIXE data in the determination of Ni content in garnets, Campbell *et al.* (1996) concluded that the GUPIX method of PIXE data reduction is accurate to ±4-6 ppm for Ni concentrations in garnet in the range of 15 to 130 ppm. In addition, it was observed that the divergence of the experimental (section 5.3.1.2) and the empirical Ni geothermometer calibrations at high and low temperatures exceeds the Ni determination uncertainty. An error of 6 ppm can cause a maximum error of 50^0C in temperature, whereas at high and low temperatures the Ni geothermometers differ by more than 50^0C. Consequently, these authors recommended that the refinement of Ni measurement is less important than a resolution of the disparity between the empirical and experimental Ni geothermometer calibrations.

5.3.1.2 Experimental calibration of the Ni geothermometer

Canil (1994) studied the partitioning of Ni between olivine and garnet in two multi-component synthetic compositions as a function of temperature and pressure. This experimental study was prompted mainly by the fact that the empirical calibration of the Ni geothermometer (Griffin *et al.*, 1989) was derived using conventional major element geothermobarometers normally applied to garnet peridotites. These geothermobarometers have many well known flaws and their application is sometimes controversial, with the result strongly dependent on the choice of geothermobarometer used (Finnerty and Boyd, 1987).

Natural mantle peridotite garnets and olivines generally have Ni contents in the region of tens of ppm and less than 4000 ppm, respectively (Canil, 1994). To do *in situ* analyses of such trace amounts in these minerals, in particular garnets, proton probe, ion probe and laser ablation ICP-MS techniques are normally used. Canil (1994) doped the starting compositions with NiO concentrations above natural levels to allow analyses of run products by electron microprobe.

Canil (1994) suggested that the elevated Ni contents, above natural levels, did not change the partitioning model that occurs at trace levels, citing a study by Beattie (1993) of olivine-liquid partitioning data for Ni which demonstrated that Ni substitution in Mg-Fe-Ni olivine obeys Henry's Law[13] to concentrations up to 60 wt% NiO. Furthermore, Canil (1994) carried out two Ni partitioning experiments on a natural fertile peridotite at 1600 and 1700^{0}C. These high temperatures were necessary to ensure that a high enough concentration of NiO was partitioned into garnet for electron microprobe analysis. The distribution coefficients determined from these two experiments were collinear with those determined from the experiments with the synthetic compositions, providing further support that partitioning at elevated Ni concentrations obeys Henry's Law (Canil, 1994).

However, this approach was criticised by Griffin and Ryan (1996) who pointed out that the minimum Ni content of 1700 ppm in Canil's (1994) experimental runs is far removed from natural compositions. These authors noted that of their greater than 20000 proton probe analyses, values above 120 ppm were extremely rare. They also noted that the application of the experimental calibration (equation 5.19 and also see calibration line in Fig. 6.8) to a typical natural lherzolite with an equilibration temperature of ~1400^{0}C would predict a Ni content of ~250 ppm.

In reply to Griffin and Ryan's (1996) criticism Canil (1996) pointed out that the criticism was based on the temperatures estimated using Fe^{2+}-Mg exchange garnet-olivine geothermometry which has been shown by Brey and Köher (1990) to have errors of up to ±113 ^{0}C. If this error is taken into account then the experimental and empirical calibrations of the Ni geothermometer are within error of each other at 1400 ^{0}C (Canil, 1996) and thus if the experimental calibration is in error at 1400 ^{0}C so is the empirical calibration.

To evaluate pressure effects on the Ni partitioning between olivine and garnet Canil (1994) used volume data for reaction 5.16 between the end-member components. From these data the calculated change in volume is very small and thus it

---

[13] Henry's Law states that at high dilution the activity coefficient k_i^j for trace component i in phase j is constant, such that the activity a_i^j of i in j is directly proportional to its concentration, X_i^j in j. This is defined by: $a_i^j = k_i X_i^j$.

was assumed that there are no pressure effects on the partitioning of Ni between garnet and olivine.

The resulting geothermometer (T-Canil) expression from this study is of the form:

$$T(K) = \frac{-10210}{\ln ppmNi^{gt} / ppmNi^{oliv} - 3.59} \qquad 5.19$$

This experimentally derived Ni geothermometer reportedly reproduced 90% of the experimental data to within ± 90^0C and agrees with the empirical Ni geothermometer of Griffin *et al.* (1989) to within ± 50^0C in the temperature range of 900 to 1200^0C. Outside this range the two calibrations differ by more than 50^0C, and in opposite directions, i.e., the experimental calibration gives lower temperature estimates at high temperatures and higher estimates at low temperatures in comparison to the empirical calibration.

5.3.2 Chrome barometry

Ryan *et al.* (1996) used the barometer of Nickel (1989) (P-NI89^1) as a starting point to obtain an expression describing the natural system of xenolith samples they used to developed a "Cr barometer" (P-Cr). P-Cr uses temperatures derived by T-Ryan and Cr-pyrope garnet composition to estimate pressure in an iterative scheme using an algorithm that combines a modified expression of P-NI89^1 (P-NI89^{1}*, discussed below) and the composition of a hypothetical opx assumed to have coexisted with the garnet. An assumption is made that the disaggregated Cr pyrope garnet coexisted with the orthopyoxene under Cr-saturated conditions, which basically means under conditions where chromite was present to buffer Cr in the orthopyroxene.

In developing P-Cr, Ryan *et al.* (1996) modified the fit parameters of the expression for P-NI89^1 by applying a least squares approximation to their xenolith data to correct for the influence of Fe on the ionic mixing in garnet and orthopyroxene. In the algorithm the composition of the hypothetical opx was estimated by inverting the geothermometer expressions of T-HA84 for Mg content

(Mg^{opx}), T-BKCaopx for X_{Ca}^{opx} and the geothermometer of Gasparik (1987) (T-GA87) for X_{Al}^{M1-opx}. Initially, pressure estimates are assumed in these geothermometers, but the assumptions are eventually improved by iteration in the algorithm. X_{Mg}^{M1-opx} and X_{Mg}^{M2-opx} are estimated from Mg^{opx} and site occupancies of Al, Cr and Ca using the following expressions:

$$X_{Mg}^{M1-opx} = \mathrm{Mg}^{opx} \bullet (1 - X_{Al}^{M1-opx} - X_{Cr}^{opx}) \quad 5.20$$

$$X_{Mg}^{M2-opx} = \mathrm{Mg}^{opx} \bullet (1 - X_{Ca}^{opx}) \quad 5.21$$

Minor components of Ti, Fe^{3+}, Mn and Na are neglected. T-GA87 was modified by adjusting the fit parameters by applying a least squares approximation to reduce the large pressure effects due to the addition of significant amounts of Cr to the CFMAS system used to develop this geothermometer.

P-Cr is reported to estimate equilibration pressure of peridotite garnets coexisting (or which once coexisted) with chromite and orthopyroxene to within ±3 kbar by Ryan *et al.* (1996). However, in P-Cr temperature estimates are made using T-Ryan which has its own uncertainties (section 5.3.1.1). In addition, the uncertainties associated with the geothermometers [T-HA84 (section5.2.2.3) and T-BKCaopx (5.2.1)] used to estimate the hypothetical orthopyroxene composition were not accounted for. Certainly these uncertainties would compound the error of 3 kbar. It also be noted that the accuracy of P-NI89^{1*} reported by Ryan *et al.* (1996) was by comparison to P-MG74. As mentioned earlier P-MG74 has a strong temperature effect, which was unaccounted for (section 5.2.3).

5.4 Evaluation of Geothermometers and Geobarometers

5.4.1 Problems in pressure and temperature estimations

Amongst other factors, most of the available experiments in natural systems, on which geothermometers and geobarometers are based, are hampered by one or more of the following:

- the lack of reversed experiments required to ensure that compositional values measured for a forward reaction are equilibrium values by reproducing these values at the same temperature and pressure in a reverse reaction;

- short experimental run times, which do not reflect the longer equilibration periods in natural systems;
- loss of Fe to metal capsules, through diffusion between samples and the capsules, leading to erroneous values for the product samples;
- poor quality of microprobe analyses during calibration of geothermometers and geobarometers;
- the simple nature of synthetic systems used in experiments, with the effects of minor components in natural systems being unknown;
- inaccurate site allocation of Al, specifically joined to the $MgAl_2SiO_6$ component, within the orthopyroxene structure (Carswell, 1991) leading to incorrect pressure estimates using geobarometry based on the Al-solubility in orthopyroxene in the simple MAS system (e.g P-MG74);
- lack of sufficiently accurate thermodynamic data for the formulation of thermodynamic expressions used to correct for the effect of minor elements on mineral equilibria;
- extrapolations, in particular with respect to pressure and temperature, that are often made beyond the experimental limits;
- pressure and temperature are estimated using independent mineral reactions which might have different closure temperatures and thus not record the same equilibration condition; and
- the uncertainty of the actual significance of the calculated pressure or temperature value - pressure and temperature estimates may either record closure of mineral systems after equilibration, or some subsequent heating event, or substantial subsolidus equilibration; also, the pressure and temperature estimates may record deformation, peak metamorphism, or nothing - the composition of minerals may be affected by partial re-equilibration.

5.4.2 Commonly used geothermobarometers

Despite the problems associated with geothermobarometry, several authors (e.g., Finnerty and Boyd, 1984, 1987; Carswell and Gibb, 1980, 1987; Brey and Köhler, 1990; Smith, *in press*) have compared and assessed existing geobarometers and geothermometers, and have reached conclusions on the preferable methods applicable to mantle-derived rocks.

Carswell and Gibb (1980) tested a number of geothermometer and geobarometer formulations in reproducing experimental P,T conditions of natural peridotites. These authors selected five geothermometers, which gave results closest to the average for several geothermometers and suggested that these five geothermometers best estimated the temperature of equilibration. In a later paper, Carswell and Gibb (1987) demonstrated that the most satisfactory geobarometer was P-NG85. These authors reiterated the suggestion of Carswell and Gibb (1980) that equilibration temperatures are best assessed by consideration of a combination of the most satisfactory geothermometer formulations, based on the pyroxene solvus and the Fe^{2+}- Mg exchange reactions between mineral pairs. However, Finnerty and Boyd (1984) objected to this method of temperature determination on the basis that there is no reason to accept the mean temperature from different geothermometers as any more accurate than an estimate from just one geothermometer.

Finnerty and Boyd (1984, 1987) tested the accuracy and precision of a number of geothermobarometer pairs. The accuracy was tested by comparison of P,T estimates for a diamond-bearing and a graphite-bearing xenolith, and phlogopite-bearing xenoliths with the P,T constraints provided by experimental data on the diamond-graphite univariant reaction curve (Kennedy and Kennedy, 1976) and the phlogopite stability curve (Eggler and Wendlandt, 1979). A number of analyses were made on each of four xenoliths selected from a wide range of P,T conditions. The scatter of P,T estimates calculated using these analyses were used to measure precision.

Finnerty and Boyd (1984) recommended the use of the 20kb diopside-enstatite miscibility gap (Lindsley and Dixon, 1976) for temperature estimation and the isopleths for Al dissolved in enstatite coexisting with pyrope (P-MG74) for pressure estimation. These authors recommended that any new geothermometers and geobarometers should be tested against petrological constraints before being routinely used. Finnerty and Boyd (1987) preferred the use of an empirical fit of the diopside limb of the pyroxene miscibility gap, corrected for the pressure effect by the method of Nickel and Brey (1984) to produce T-FB87, for temperature estimation and reaffirmed their preference for the P-MG74.

Carswell and Gibb (1987) denounced the approach of Finnerty and Boyd (1984, 1987), on the basis that the number of samples used to compare with the stability curve of diamond and graphite was very small: only one diamond-bearing peridotite and one graphite-bearing peridotite were used. In addition, Carswell and Gibb (1987) pointed out that, as admitted by Finnerty and Boyd (1984), the P,T location of the phlogopite stability curve used was uncertain.

The issue of the limited number of samples used by Finnerty and Boyd (1984, 1987) has been addressed by Pearson *et al.* (1994). These authors evaluated the possibility of metastable crystallisation of graphite within the diamond stability field. In this study the P,T conditions were calculated for five diamond-bearing and five graphite-bearing lherzolites, using the geothermobarometers of Finnetry and Boyd (1987) (T-FB87_P-MG74) and of Brey and Köhler (1990) (T-BK2px_P-BK90). The P,T estimates were found to be in very good agreement with the experimentally determined diamond-graphite curve of Kennedy and Kennedy (1976), i.e., temperature estimates for diamond-bearing lherzolites plotted within the diamond stability field and the graphite-bearing lherzolites plotted within the graphite stability field .

Brey and Köhler (1990) used the experimental data of Brey *et al.* (1990) to evaluate existing geothermometers and geobarometers. None of the tested geothermometers and geobarometers satisfactorily reproduced the experimental data over the whole P,T conditions (10 to 60 kb and 900 to 1400^0C) of the experiments. Of the garnet-clinopyroxene geothermometers only T-KR88 reproduced the experimental data, although with some scatter. The older versions of the same geothermometer (Ellis and Green, 1979; Powell, 1985) overestimated temperature estimates at low temperature ranges. Brey and Köhler (1990) attributed this better reproduction of data by T-KR88 to the curvilinear approach applied by Krogh (1988) in the correction for X_{Ca} in garnet, as opposed to the linear approach applied in both the studies of Ellis and Green (1979) and of Powell (1985). Although also showing much scatter, the other Fe^{2+}-Mg exchange geothermometer which reproduced the experimental data was the garnet-olivine calibration of T-OW79 However, as mentioned in section 5.3.1.1 the experimental data was reproduced to ±113 °C.

Brey and Köhler (1990) considered pyroxene solvus geothermometry as having the best potential in the reproduction of the experimental data. T-Wells reproduced the experimental data at 900°C but increasingly overestimated the data at higher temperatures. On the other hand T-FB87 reproduced the experimental data at high temperatures but underestimated the data at low temperatures. Brey and Köhler (1990) attributed these discrepancies to the correction for Fe influence hidden in the choice of K_d and in the neglect of the influence of the Na content in clinopyroxene. T-BM85, which has a Na correction term, nevertheless underestimated the experimental data. This underestimation is attributed to the correction of Fe in clinopyroxene, which was determined over a very narrow temperature range of 800 to 1000°C with data having too large a scatter to produce a universally applicable correction factor (Brey and Köhler, 1990).

In their evaluation of geobarometers Brey and Köhler (1990) reached conclusions similar to those of Carswell and Gibb (1987), that is, that the geobarometer P-NG85 reproduces experimental results satisfactorily. This geobarometer reproduced experimental data of Brey *et al.* (1990) very well, but only within the pressure range (10 to 35 kb) of the experiments on which it was based. The geobarometer P-MG74 did not yield satisfactory comparisons with the experimental data. The geobarometer formulated by Köhler and Brey (1990) (P-KB90), based on the exchange of Ca between olivine and clinopyroxene, also adequately reproduced the Brey *et al.* (1990) experimental data.

The geothermobarometer combinations recommended by Brey and Köhler (1990) for the estimation of pressures and temperatures of equilibration are T-BK2px_P-BK90, T-BK2px_P-KB90, T-KR88_P-BK90 and T-OW79_P-BK90.

5.4.3 Inflected geotherms - *are they real?*

Many geothermobarometer combinations yield P,T arrays that are inflected to higher geothermal gradients at depth. The lower limb of these geotherms is generally defined by P,T estimates for low temperature coarse peridotites and is parallel to the continental shield conductive geotherm of Pollack and Chapman (1977). The upper limb is defined by P,T estimates for high temperature deformed peridotites and is inflected to temperatures that are higher than the continental shield geotherm.

Several suggestions for the cause of the inflection of geotherms have been put forward. On the one hand Boyd (1973) and Boyd and Nixon (1975) suggested that, on the basis of textural data and the steeper geothermal gradients beyond the point of inflection, the perturbation of the geotherms was due to shearing of the lowermost section of the rigid upper mantle as it moved over the ductile lower mantle during the break up of Gondwanaland. They proposed the point of inflection represented the top of the low velocity zone and that the inflected geotherm represented ambient thermal conditions of the upper mantle. This model implies that at the time of emplacement of the kimberlites the mantle had stratigraphic layer of deformed peridotite. The "proof" for the lateral extent of this thermal structure was given by Boyd and Nixon (1973) and Boyd (1974) who found similar (inflected) geotherms for, respectively, the northern Lesotho and the Frank Smith kimberlites (Fig. 2.1), which are ~400km apart in Kaapvaal craton. Finnerty and Boyd (1984,1987) and Finnerty (1989) have advocated this model using several independent geothermobarometer combinations.

On the other hand, in other studies it has been suggested that the inflected geotherms are not representations of the ambient thermal conditions of the upper mantle but are due to localised transient thermal disturbances caused by one of the following:

- thermal interactions of the mantle with a rising diapir immediately prior to kimberlite eruption (Green and Guegen, 1974);
- thermal interactions of kimberlites and the mantle (Mitchell, 1978,1984; Mitchell *et al.*, 1980); or
- movement of a continent over a heat source, possibly a hot upwelling convection stream, leading to thermal erosion and thermal perturbations of the lowermost part of

the upper mantle (Nickel and Green, 1985).

However, many other geothermobarometer combinations do not yield inflected geotherms but produce P,T arrays that are almost parallel to the conductive geotherm for the whole P,T range. For example, Mercier and Carter (1975) rejected the model of shearing noting that the expected viscosities and strain rates at the physical conditions where the inflection apparently occurs are too low for shear heating to be significant. They suggested that the inflection of geotherms was an artefact representing variations in the degree of depletion of mantle minerals with depth, which is recorded by variations in minor elements. Such variations in minor elements affect mineral equilibria and are not accounted for by geothermobarometers based on simple MAS and CMS systems. Mercier and Carter (1975) applied corrections for the Fe^{2+} and Mn^{2+} effects on Ca-Mg substitution (as in Wood and Banno, 1973) in pyroxene solvus geothermometry based on the experiments of Davis and Boyd (1966). They also corrected for the effect of divalent (Fe^{2+} and Ca) and non-divalent (Cr^{3+} and Na) cations on the Al solubility in garnet-orthopyroxene geobarometry based on the experimental data of McGregor (1974). Application to natural peridotites of the geothermobarometer with these corrections produced linear geotherms for south African kimberlites (Mercier and Carter, 1975).

Carswell (1991) refuted the existence of inflected geotherms noting that such geotherms are an artefact of the inaccuracies in the manner in which the key composition parameter in garnet-opx geobarometry, i.e. the amount of Al specifically involved in Mg-Tschermaks ($MgAl_2SiO_6$) substitution is treated. He noted that, on application of the Al solubility garnet-orthopyroxene geobarometry to natural systems, it is important to take into account the fact that Al in orthopyroxenes may be linked to Na in the M2 site or to Cr, Ti and Fe^{3+} in the M1 site. Ignoring the effect of these minor elements on Al partitioning has led to incorrect determination of pressures using the geobarometer, P-MG74, used by Finnerty and Boyd (1984, 1987), derived from data in the MAS systems without considering Ca, Cr and Fe influence on Al partitioning (Carswell, 1991).

On using the geothermobarometer combination T-BM85_P-NG85 and algorithms for calculating $X^{M1\text{-}opx}_{Al\text{-}Ts}$, which takes into account the effect of the minor elements in the solubility of Al in orthopyroxene Carswell (1991) found a geotherm which if anything is inflected to lower geothermal gradients at high pressures. Similar results were found by Bertrand *et al.* (1986) who used a combination of T-BM85 and a geobarometer they developed for the CFMAS system. These authors report to have successfully tested this geobarometer, in the P,T range of up to 40 kb and up to 1500^{0}C, against the reversed natural system experimental data of Mori and Green (1978).

Other studies have claimed that because of chemical inequilibrium (Brey, 1991) or different closure temperatures for the garnet-opx and pyroxene solvus exchange systems (Fraser and Lawless, 1978) geotherms derived for the cratonic mantle using the low temperature coarse peridotites are inaccurate. Irving (1976) suggested that there is a genetic link between xenolith formation and magma generation processes, which together involve perturbation of geotherms. He concluded xenoliths do not represent a steady-state geotherm of the upper mantle but rather a localised, highly complex P,T regime associated with magma generation.

The work in the present study cannot resolve the controversies regarding inflected geotherms. Based on textural data of mantle xenoliths and P,T estimates derived using various geothermobarometers, there seems to be no doubt that high temperature deformed peridotites have been affected by some thermal disturbance. However, it is not clear whether the disturbance shifted P,T estimates to higher geothermal gradients (Boyd, 1973; Finnerty and Boyd, 1984, 1987) or to lower geothermal gradients (Bertrand *et al.*, 1986; Carswell, 1991) or to P,T estimates that follow the curvature of the continental geotherm (Mercier and Carter, 1975). Nevertheless, based on the fact that the geothermometer considered the most appropriate for the determination of PT conditions (T-BK2px_P-BK90; section 5.5), does not yield inflected geotherms, it is considered that geotherms are not perturbed in the way suggested by Boyd (1973).

5.5 Conclusion

In this study, T-BK2px_P-BK90 is considered to be the most reliable geothermobarometer. The main reasons for this choice are that:

- the geothermometer, T-BK2px, is based on pyroxene solvus and is thus immune to the "Fe^{3+} uncertainty" problem (Canil and O'Neill, 1996);
- both T-BK2px and the barometer, P-BK90, take into account the effect of minor elements in both pyroxenes, and were calibrated at temperature and pressure conditions (900-1400^{0}C and 10-60 kb; Brey and Köhler, 1990) that are applicable to natural peridotites,
- the geothermobarometer combination T-BK2px_P-BK90 best reproduced experimental data of natural peridotite compositions (Brey and Köhler, 1990);
- T-BK2px_P-BK90 P,T estimates closely approximate the graphite-diamond equilibrium boundary determined by Kennedy and Kennedy (1976) (Pearson *et al.*, 1994); and
- T-BK2px_P-BK90 P,T estimates closely approximate the garnet-spinel peridotite transition at 20 kb and 1000^{0}C (Ionov *et al.*, 1993).

However, in addition to T-BK90_P-BK90 the geothermobarometers recommended by Finnerty and Boyd (1987), Brey and Köhler (1990), Pearson *et al.* (1994) were also used for the following reasons:

- To allow comparison with Ni geothermometry of geothermometers applicable to clinopyroxene-free peridotites;
- To allow comparison with Ni geothermometry of geothermobarometers that give the still contentious inflected geotherms; and
- To evaluate equilibrium of the samples studied by comparing temperature estimates made using geothermometers based on different mineral reactions.

These geothermobarometers, listed in the same order as the reasons why they were used which are mentioned immediately above, are:

- T-OW79_P-BK90, temperature based on the Fe^{2+}-Mg exchange between coexisting garnet and olivine. However, T-OW79_P-MG74 was also used for comparison since this geothermobarometer was used to calibrate T-Ryan;

- T-FB87_P-MG74 and T-BM85_P-NG85, temperature based on pyroxene solvus geothermometry; and
- T-KR88_P-BK90 and T-BE95_P-BK90, temperature based on the Fe^{2+}-Mg exchange between coexisting garnet and clinopyroxene.

The method of Carswell and Gibb (1984, 1987) was not applied here simply because it is based on averages of several geothermobarometers and therefore does not correspond to any one set of experimental data.

Chapter 6

6. Geothermobarometry - *results*

6.1 Introduction

Based on the study of Hops (1989), only samples with a homogeneous major element composition from Jagersfontein were selected. However, cores and rims of the minerals in these samples, including Matsoku samples, were reanalysed. None of the samples showed any significant heterogeneity in major element or Ni abundances. Hence, only core major element abundances for conventional geothermometry and averages of the analyses of several spots on garnet cores and rims for Ni geothermometry were used for temperature calculations. For reasons given in section 5.5, Ni concentrations determined by PIXE were used for the evaluation of Ni geothermometry for all but one (J117) sample for which LA-ICP-MS Ni data were used.

Kjarsgaard (1992) examined the validity of the original empirical Ni geothermometer (Griffin *et al.*, 1989) as a diamond exploration tool by comparing the equilibration temperatures of peridotite xenoliths from Somerset Island, Northwest Territories, Canada, estimated by this Ni geothermometer to the temperature estimates derived using T-BK2px and T-FB87. He found a good correlation (±80°C) between the original Ni geothermometer and T-BK2px when the Ni content of olivines was not assumed to be 3000 ppm. The correlation weakened to ±140°C when olivine Ni abundances were assumed to be 3000 ppm. Temperature discrepancies of up to 238°C were observed when the Ni geothermometer was compared to T-FB87, which was used to estimate reference temperatures in the calibration of the original Ni geothermometer.

The effect of assuming a 3000 ppm Ni abundance for olivines was however not investigated in the present study because, Ryan *et al.* (1996) neither gave the equation of the regression line through data in their ln(ppmNi^{garnet}/ppmNi^{olivine}) vs T plot nor did they report olivine and garnet Ni data used in the calibration of T-Ryan. The equation used in this study is that for ln(ppmNi^{garnet}) vs T plot, as given by Ryan *et al.* (1996).

6.2 Conventional geothermometry

6.2.1 Temperature estimates

Table 6.1 compares temperature estimates by methods mentioned above with the temperatures calculated using T-BK2px. In order to have temperature as the only variable, pressure was calculated using the preferred geobarometer, P-BK90. However, for reasons given in section 5.5 P-NG85 and P-MG74 were also used for pressure estimates and were, respectively, combined with T-BM86 and T-FB87. Conventional geothermometry yielded a narrow temperature range for the Matsoku peridotites. All the geothermometers yielded temperature estimates within a temperature range of 972 to 1182^{0}C. The preferred geothermometer (T-BK2px) yielded a range of 1070 to 1160^{0}C (90^{0}C range). There is no clear division between coarse and deformed peridotites from this locality into, respectively, low and high temperature types, as occurs in some Kaapvaal craton kimberlite localities (Boyd, 1973; Boyd and Nixon, 1975; Nixon and Boyd, 1973; Finnerty and Boyd, 1987).

For the Jagersfontein peridotites, conventional geothermometry yielded a wide temperature range, from 607 to 1415^{0}C. Coarse and deformed peridotites were divided, respectively, into low and high temperature peridotites (Table 6.1). The exception to this rule is a coarse peridotite, sample number J117, which has temperature estimates as high as the deformed peridotites.

Since, for reasons given in section 5.5, the other geothermometers would be compared with the Ni geothermometers their accuracy was evaluated against T-BK2px. A comparison of T-BK2px with the other conventional geothermometers is presented in Figs. 6.1 and 6.3. The other pyroxene solvus geothermometers, T-FB87 and T-BM85, reproduced T-BK2px temperature estimates very well (Fig. 6.1). The difference between T-BK2px and T-FB87 is not more than 50^{0}C for most of the

Table 6.1 Pressure and temperature estimates calculated using Ni geothermometers and conventional geothermobarometers. The samples are listed in ascending order of Ni concentration in garnet determined by PIXE. The missing P,T estimates are for cases where the particular geothermobarometer is not applicable, i.e. for clinopyroxene-free samples and pyroxene-free samples (garnet dunites, LBM20 and JJH23). Failed = see section 6.2.1. TYPE: CP = coarse peridotite; DP = deformed peridotite. Texture: c = coarse, p = porphyroclastic, mp = mosaic porphyroclastic, fmp = fluidal mosaic porphyroclastic. * = determined by LA-ICP-MS.

				Ni geothermometry			Pyroxene solvus geothermometry						Fe-Mg exchange geothermometry							
	Sample No.	TYPE	Texture	Avg.Ni ppm	T(Ryan) deg. C	T(Canil) deg. C	P-BK90 kbar	T-BK90 deg. C	P-MG74 kbar	T-FB87 deg. C	P-NG85 kbar	T-BM85 deg. C	P-MC74 kbar	T-OW79 deg. C	P-BK90 kbar	T-OW79 deg. C	P-BK90 kbar	T-KR88 deg. C	P-BK90 kbar	T-BE95 deg. C
Jagersfontein	JJG1733	CP	c	14	721	860	21	628	Failed	Failed	26	683	24	660	22	650	19	607	22	657
	JJG1716	CP	c	16	751	880							32	788	30	776				
	JJG864	CP	c	26	851	934	38	939	40	921	33	890	39	903	35	881	38	933	39	950
	JJG1728	CP	c	35	927	1003							37	979	28	931				
	JJG1761	CP	c	35	927	1023							45	1025	35	974				
	JJG1767	CP	c	57	1077	1102							58	1213	52	1191				
	JJH1	DP	p	63	1110	1092							57	1195	47	1152				
	JJH36	DP	p	71	1156	1127	54	1199	58	1161	51	1138	63	1241	54	1208	51	1147	49	1115
	JJH23	DP	mp	73	1168	1121														
	JJH9	DP	p	77	1185	1130							53	1071	46	1041				
	JJH6	DP	p	77	1185	1128							58	1127	52	1105				
	JJH28	DP	p	77	1185	1135	57	1260	55	1174	52	1187	58	1214	53	1193	50	1152	50	1152
	JJH29	DP	p	92	1263	1172							54	1164	37	1090				
	JJG1729	DP	mp	94	1271	1176	64	1322	61	1277	54	1193	48	1073	47	1069	58	1240	55	1199
	JJH32	DP	p	98	1289	1178	57	1311	60	1283	50	1254	55	1214	50	1192	48	1169	49	1174
	JJH8	DP	mp	99	1296	1183	54	1304	63	1322	49	1244	52	1144	41	1096	47	1195	45	1166
	JJH10	DP	mp	100	1302	1179	57	1296	60	1301	48	1225	55	1218	50	1199	52	1224	51	1203
	JJH7	DP	mp	101	1304	1207	60	1394	63	1374	49	1332	51	1189	45	1165	56	1341	50	1238
	JJG1710	DP	fmp	102	1309	1192	55	1315	61	1302	49	1268	56	1225	48	1192	48	1198	47	1183
	J117	CP	c	112*	1355	1221	68	1415	63	1359	52	1329	55	1227	56	1231	65	1370	59	1282
Matsoku	LBM32	DP	p	35	927	1008	46	1115	49	1100			44	1019	37	985	45	1096	46	1109
	LBM10	CP	c	41	967	998	51	1125	51	1108	49	1049	51	1106	49	1101	49	1099	47	1062
	LBM8	CP	c	43	985	1010							49	1076	40	1036				
	LBM9	CP	c	43	985	1002	46	1130	50	1100	42	1065	47	1060	40	1025	39	1018	41	1042
	LBM3	CP	c	45	1000	1019	47	1108	48	1041	41	1027	46	1019	40	987	47	1111	46	1089
	LBM17	CP	c	46	1005	1030							48	1053	41	1020				
	LBM16	DP	p	47	1014	1030	47	1160	53	1156	44	1076	51	1128	43	1092	48	1182	47	1153
	LBM36-2	CP	c	48	1021	1016	51	1122	50	1071	42	1020	51	1079	47	1060	45	1030	48	1071
	LBM30	DP	p	48	1021	1081	47	1120	51	1115	43	1030	45	1020	39	991	45	1095	45	1091
	LBM22	DP	p	50	1034	1073							45	1025	41	1003				
	LBM20	DP	p	52	1046	1060														
	LBM36-3	CP	c	54	1058	1040	49	1110	42	973	39	1004	48	1066	44	1045	43	1037	46	1081
	LBM6	CP	c	56	1067	1061	45	1070	51	1072	42	988	49	1042	41	1005	41	1003	41	1014

peridotites (Fig. 6.1a). T-BM85 generally yielded temperatures that are systematically lower, but mostly by not more than 100^{0}C, than those derived using T-BK2px (Fig. 6.1b). T-FB87_P-MG74 failed at low temperatures, yielding a very low temperature estimate (311^{0}C) and an unreasonably low pressure estimate (0.3 kb), hence the missing data point (for JJG1733) at low temperatures in Figs. 6.1a and c and Table 6.1. The failure of the geothermometer (T-FB87) is due to its inapplicability to peridotites with high [14]Ca#$_{cpx}$'s; clinopyroxenes in JJG1733 have a Ca# of 0.50. The failure of the geobarometer is due to the low temperature estimates (311^{0}C, T-FB87) used to calculate pressure. Using the temperature of 628^{0}C, derived using T-BK2px, the pressure estimate using P-MG74 is 22 kb, in accord with the other geobarometers.

A good correlation was also observed between T-BM85 and T-FB87 (Fig. 6.1c). Therefore, pyroxene solvus geothermometers used here are in agreement to one another.

The Fe^{2+}-Mg exchange geothermometers correlate well with one another at low temperatures and fairly at high temperatures (Fig. 6.2). The difference between T-BE95 and T-KR88 temperature estimates is less than 50^{0}C for all but two high temperature peridotites (Fig. 6.2a). Correlation between the garnet-clinopyroxene geothermometers, T-BE95 and T-KR88, with the garnet-olivine geothermometer T-OW79_P-BK90 is good at low temperature and poor for some of the high temperature peridotites (Fig. 6.2b and c). Temperature estimates calculated by T-OW79_P-MG74, which was used to calibrate T-Ryan, are generally slightly higher than those calculated using T-OW79_P-BK90 at high temperatures (Fig. 6.2d). However, the difference between these two geothermobarometers (T-OW79_P-MG74 and T-OW79_P-BK90) is not more than 50^{0}C for all but one sample.

All the Fe^{2+}-Mg exchange geothermometers only reproduced the T-BK2px temperature estimates at low temperatures. Above 1200^{0}C (T-BK2px_P-BK90) the Fe^{2+}-Mg exchange geothermometers yielded lower temperature estimates than T-BK2px (Fig. 6.3); by up to 230^{0}C when T-OW79 is used and by up to 150^{0}C when T-

---

[14] Ca# = atomic [Ca/(Ca+Mg)]

KR88 or T-BE95 are used. This seemingly systematic difference in temperature estimates at high temperatures might be due to one or more of the factors that affect the accuracy of all geothermometers, including those listed in section 5.4. However, the one factor that is common to all Fe^{2+}-Mg exchange geothermometers is the assumption that all Fe in the minerals concerned occurs as Fe^{2+}. In the section below, the effects of this assumption on the resultant temperature are investigated.

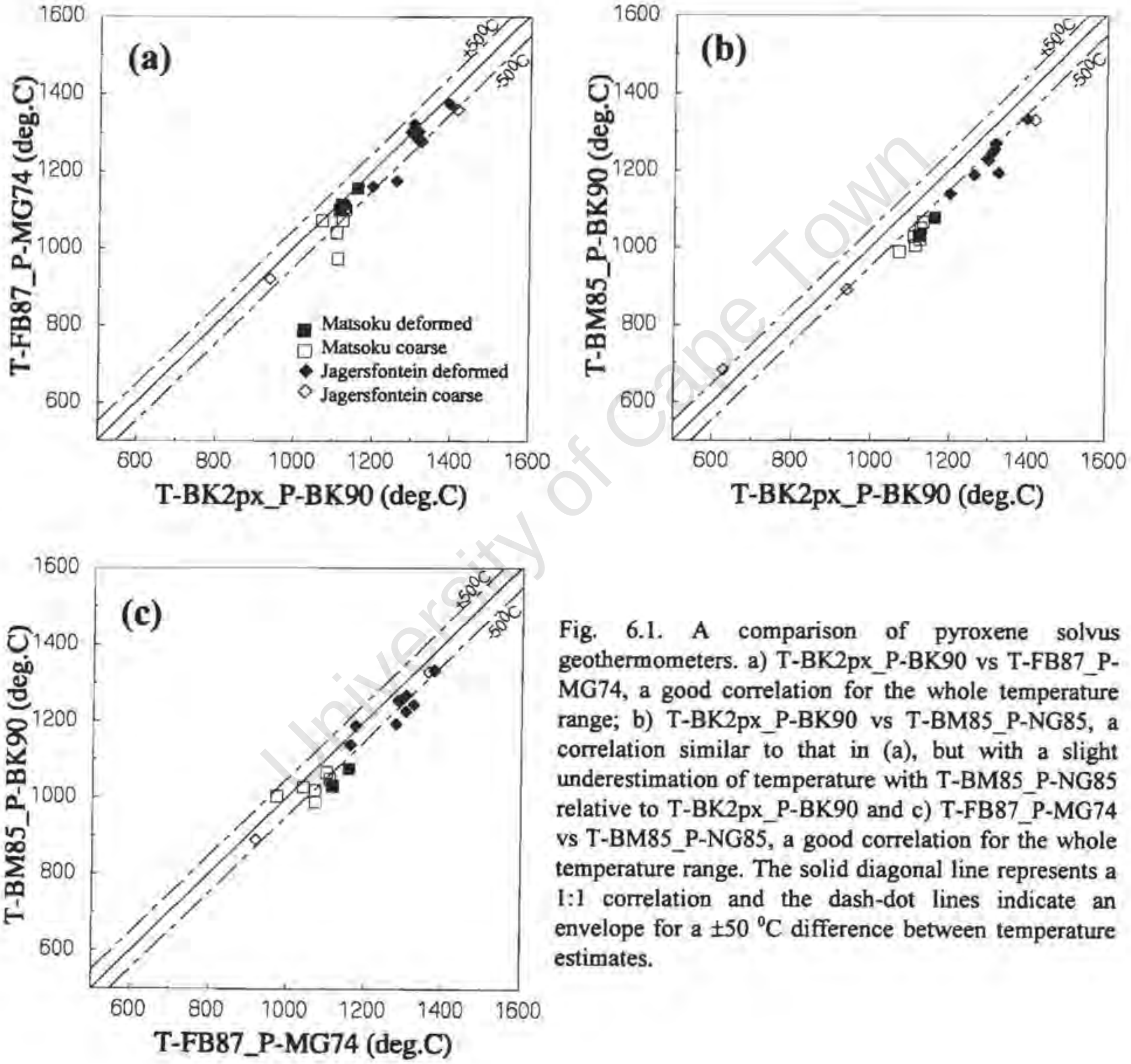

Fig. 6.1. A comparison of pyroxene solvus geothermometers. a) T-BK2px_P-BK90 vs T-FB87_P-MG74, a good correlation for the whole temperature range; b) T-BK2px_P-BK90 vs T-BM85_P-NG85, a correlation similar to that in (a), but with a slight underestimation of temperature with T-BM85_P-NG85 relative to T-BK2px_P-BK90 and c) T-FB87_P-MG74 vs T-BM85_P-NG85, a good correlation for the whole temperature range. The solid diagonal line represents a 1:1 correlation and the dash-dot lines indicate an envelope for a ±50 °C difference between temperature estimates.

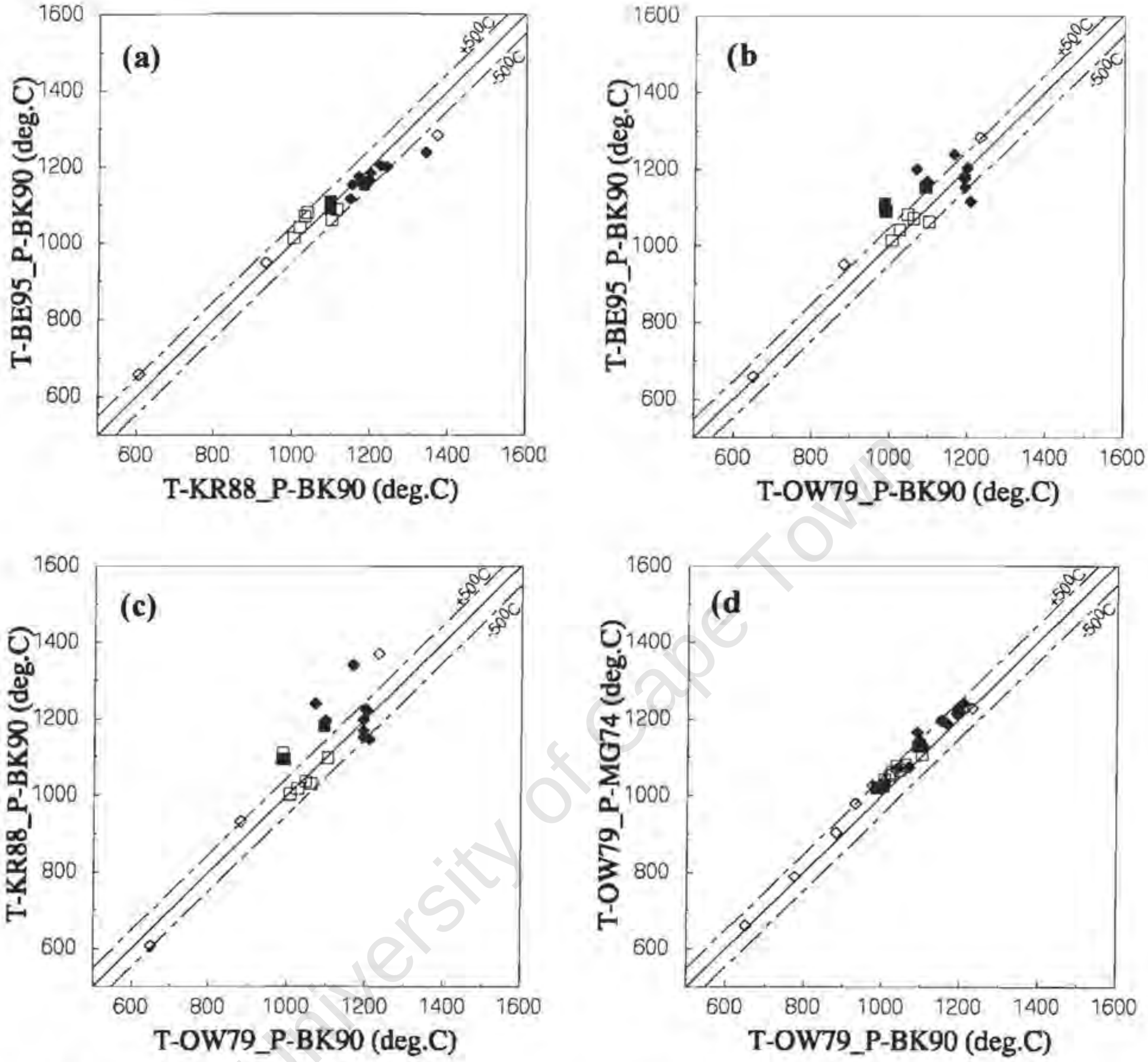

Fig. 6.2. A comparison of Fe^{2+}-Mg exchange geothermometers. a) T-KR88_P-BK90 vs T-BE95_P-BK90, a good correlation for all but two peridotites for these garnet(gt)-clinopyroxene(cpx) geothermometers; b) and c) a good correlation of the gt-cpx geothermometers with the gt-olivine geothermometer (T-OW79) at low temperatures and a poor correlation at high temperatures for a few of the peridotites; d) a comparison of the T-OW79 combined with P-BK90 with the same geothermometer combined with P-MG74, when combined with P-MG74 T-OW79 yielded slightly higher temperatures than when it is combined with P-BK90. The symbols and lines are as in Fig. 6.1.

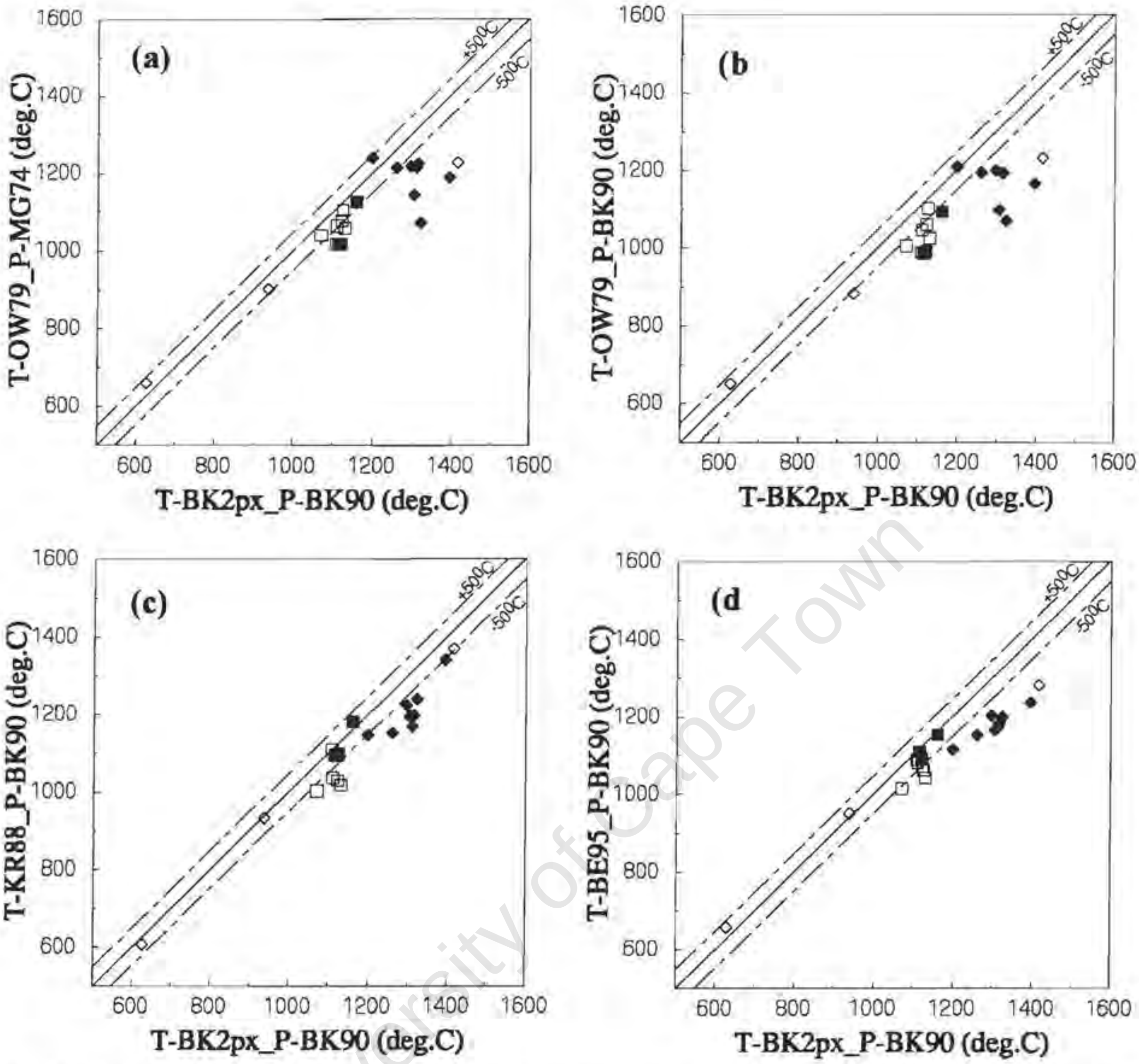

Fig. 6.3. A comparison of the Fe^{2+}-Mg exchange geothermometers with T-BK2px. These geothermometers correlate well with T-BK2px only at temperatures lower than 1200°C (T-BK2px_P-BK90). At temperatures that are higher than 1200°C the Fe^{2+}-Mg geothermometers underestimate the temperatures calculated by T-BK2px_P-BK90. The symbols and lines are as in Fig. 6.1.

6.2.2 The effect of Fe^{3+} in conventional geothermometry

All the Fe^{2+}-Mg exchange geothermometers selected for use in this study have one thing in common: they are all based on the Fe^{2+}-Mg exchange between garnet and a coexisting mineral phase. This mineral phase is olivine in T-OW79, and clinopyroxene in T-KR88 and T-BE95. Thus, it appears that whatever mineral phase is coupled with garnet in Fe^{2+}-Mg exchange geothermometry the same correlation with pyroxene solvus geothermometry is observed. This is supported by the correlation shown by T-HA84, a geothermometer based on the Fe^{2+}-Mg partitioning between garnet and orthopyroxene (Harley, 1984), with T-BK2px (Fig. 6.4). Although poor, the correlation has a similar shape to that when T-BK2px is compared to the other Fe^{2+}-Mg exchange geothermometers.

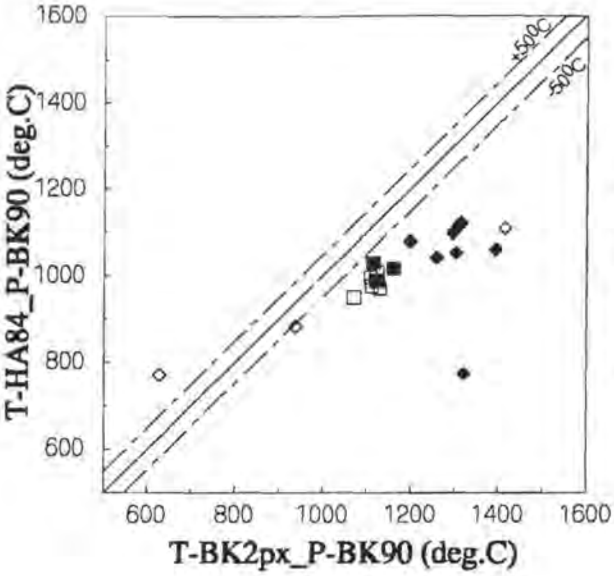

Fig. 6.4. A comparison of T-BK2px and a garnet-orthopyroxene Fe^{2+}-Mg geothermometer, T-HA84_P-BK90. A poor correlation occurs for the whole temperature range. However, the shape of the correlation is the similar to that in Fig. 6.3, with the correlation being worse at temperatures greater than 1200^{0}C (T-BK2px_P-BK90). The symbols and lines are as in Fig 6.1.

In Fe^{2+}-Mg exchange geothermobarometry Fe^{3+} is either considered to be zero and all Fe assumed to occur as Fe^{2+}, or Fe^{3+} values are estimated by stoichiometric calculations using electron microprobe analyses. However, stoichiometric calculations are good for spinels but poor for garnets and pyroxenes (Canil and O'Neill, 1996). In the study of Luth *et al.* (1990), $Fe^{3+}/\Sigma Fe$ ratios for garnets calculated from stoichiometry diverge considerably from those measured by Mössbauer spectroscopy. Similar observations were made by Virgo *et al.* (1988) for ilmenites and McGuire *et al.* (1989) for clinopyroxenes (augites). Therefore, based on the findings of these studies no stoichiometric calculations were made for the samples studied here.

Several authors have reported Fe contents measured by Mössbauer spectroscopy for upper mantle minerals during studies of the mantle oxidation state (e.g. Luth *et al.*, 1990; McGuire, *et al.*, 1991; Luth and Canil, 1993; Canil and O'Neill, 1996). Luth *et al.* (1990) reported a bimodal distribution of $Fe^{3+}/\Sigma Fe$ ratios for garnets from garnet peridotites. These authors found that garnets from low temperature peridotites have $Fe^{3+}/\Sigma Fe$ ratios ranging from 0.048 to 0.057 and those from high temperature peridotites have $Fe^{3+}/\Sigma Fe$ ratios ranging from 0.107 to 0.118. Luth and Canil (1993) found $Fe^{3+}/\Sigma Fe$ ratios between 0.04 and 0.14 for orthopyroxenes, and between 0.12

and 0.24 for clinopyroxenes. Canil and O'Neill (1996), however, found a continuous positive correlation between $Fe^{3+}/\Sigma Fe$ ratios and temperature for mantle garnets, and approximately constant ratios for pyroxenes, with values of 0.1 for orthopyroxenes and 0.41 for clinopyroxenes. Only negligible amounts of Fe^{3+} are found in olivines (Canil and O'Neill, 1996).

The essential term in Fe^{2+}-Mg exchange geothermometry formulations, to which estimated temperature is directly or inversely proportional, is the partition coefficient of Fe^{2+} and Mg between mineral phases, $\ln K_d(Fe^{2+}\text{-}Mg)$, calculated from the Fe^{2+}/Mg ratio of the mineral phases concerned. If significant amounts of Fe^{3+} in garnet are ignored and all Fe is assumed to occur as Fe^{2+} $\ln K_d$ would be overestimated in garnet-olivine geothermometry (T-OW79): $\ln K_d^{gt\text{-}oliv} = \ln[(Fe^{2+}/Mg)_{gt}/(Fe^{2+}/Mg)_{oliv}]$. Consequently, estimated temperatures would be underestimated, because temperature is proportional to $1/\ln K_d$ in the T-OW79 formula. The situation is more complicated in garnet-clinopyroxene geothermometry, where in addition to garnets, clinopyroxenes can have significant Fe^{3+}contents. The $(Fe^{2+}/Mg)_{gt}/(Fe^{2+}/Mg)_{cpx}$ ratio can either be underestimated or overestimated depending on the Fe^{3+} content in garnet relative to that in clinopyroxene. The effect might also cancel out in the ratio in this case.

The effect of Fe^{3+}contents on P,T estimates has been assessed by McGuire *et al.* (1989), and Luth and Canil (1993) in garnet-clinopyroxene geothermometry and by Luth *et al.* (1990) in garnet-olivine geothermometry. In these studies, significant differences in P,T estimates were observed between ignoring Fe^{3+} and taking it into consideration. Canil and O'Neill (1996) examined the effect of Fe^{3+}contents in all coexisting mantle phases on P,T estimates on the same samples, using different geothermobarometer combinations. They found that, depending on whether Fe^{3+} contents are considered or not in the calculation of K_d, differences between T-OW79 values can exceed 200^{0}C and can exceed 300^{0}C between temperature values estimated by garnet-clinopyroxene geothermometry.

An empirical test, similar to that done by Canil and O'Neill (1996) where temperature estimates calculated with and without Fe^{3+} on the same rocks were compared, was conducted on seven of the peridotites in this study (Fig. 6.5). To investigate the worst case scenario, the estimated Fe^{3+}contents used were the highest values reported in the studies discussed above: $Fe^{3+}/\Sigma Fe = 0.12$ for high temperature peridotite garnets, 0.05 for low temperature peridotite garnets, and, respectively, 0.4 and 0.1 for all clino- and orthopyroxenes.

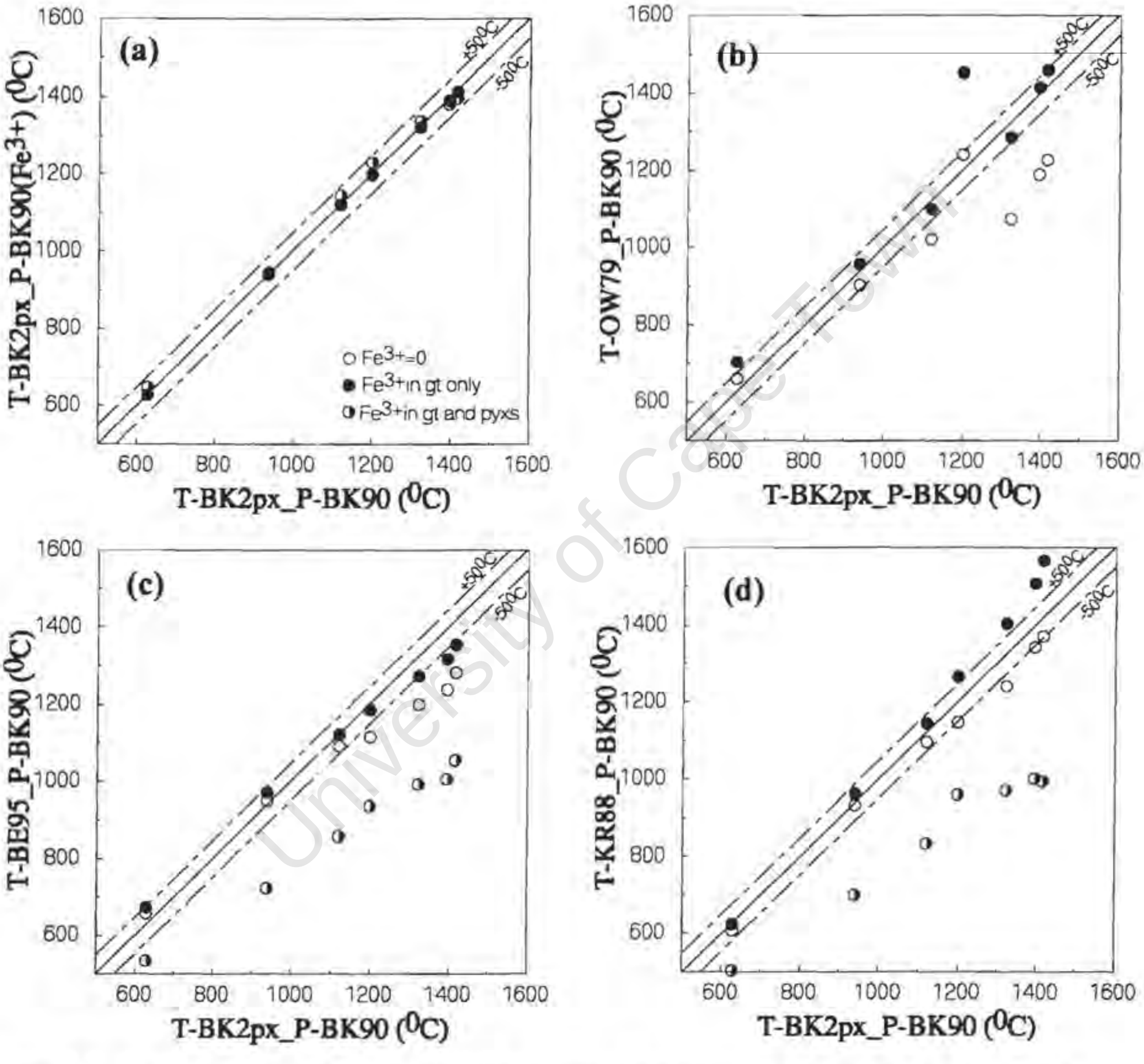

Fig. 6.5. A comparison of the conventional temperature estimates with and without taking the Fe^{3+} content of garnets and pyroxenes into consideration. a) A plot of T-BK2px_P-BK90 (without taking Fe^{3+} contents into account) against the same geothermometer, taking into account Fe^{3+} contents in garnets (filled circles), and both in garnet and pyroxenes (half filled circles); **note** that there are no open circles here because T-BK2px is compared against itself. b) T-OW79_P-BK90, without Fe^{3+} contents (open circles) and with Fe^{3+} contents in garnets (filled circles) is compared to T-BK2px_P-BK90. c) and d) respectively represent comparisons of T-BE95_P-BK90 and T-KR88_P-BK90 with T-BK2px_P-BK90. The lines are the same as in Fig. 6.1, gt = garnet, pyxs = pyroxenes.

The temperature estimates made using T-BK2px_P-BK90, with or without considering Fe^{3+} contents, in garnet only or in both garnets and pyroxenes, are the same (Fig. 6.5a). This further supports the choice of the T-BK2px_P-BK90 as the preferred geothermobarometer. Similar results were found by Luth and Canil (1993), and Canil and O'Neill (1996). In contrast, for Fe^{2+}-Mg exchange geothermometry, major shifts in temperature estimates are observed when Fe^{3+} is taken into account. The correlation between T-BK2px and T-OW79 (Fe^{2+}-Mg exchange between garnet and olivine) at high temperatures is improved (Fig. 6.5b), contrary to the observations reported by Canil and O'Neill (1996), who found an increase in the divergence between T-BK2px and T-OW79 when Fe^{3+} contents were taken into account. The reason for this is unclear when Fe^{3+} contents of the garnets produced from the experiments of O'Neill and Wood (1979) and for garnets used in this study are not known. For instance, if the garnets used in the formulation of T-OW79 had Fe^{3+} values that are similar to those in the samples used by Canil and O'Neill (1996), then taking Fe^{3+} contents into account in the samples used by Canil and O'Neill (1996) would weaken the correlation between T-OW79 and T-BK2px. On the other hand if the garnets used in the formulation of T-OW79 were different from the garnets studied here, then taking Fe^{3+} contents into account in the samples in this study would improve correlation between T-BK2px and T-OW79 in the manner shown in Fig. 6.5.

Similar improvements are observed for the correlation between T-BK2px and T-BE95 (Fe^{2+}-Mg exchange between garnet and clinopyroxene), when Fe^{3+} is estimated only for garnet (Fig. 6.5c). Large disparities between temperature estimates made using T-BK2px and T-BE95 are observed when Fe^{3+} contents are estimated for both garnets and clinopyroxenes. Similar shifts in temperature estimates are observed for T-KR88 (Fe^{2+}-Mg exchange between garnet and clinopyroxene) (Fig. 6.5d) which however, worsened the disparity between T-KR88 and T-BK2px for samples with the highest temperature estimates.

These temperature shifts should not be taken as accurate because the Fe^{3+} values used have not been measured on minerals from the rocks under study. For example, correlation of temperature estimates for one sample was weakened by the use of the estimated $Fe^{3+}/\Sigma Fe$ values in the calculation of temperature (Fig. 6.5b). Moreover, the

$Fe^{3+}/\Sigma Fe$ values used for pyroxenes are the highest values found by Canil and O'Neill (1996) for pyroxenes in their study. However, the results demonstrate the effect that ignoring significant amounts of Fe^{3+} can have on temperatures calculated using Fe^{2+}-Mg geothermometry.

The anomalous results found when Fe^{3+} in pyroxenes is taken into account (Fig. 6.5 c and d) can either be due to the inaccuracy of the garnet-clinopyroxene geothermometers or the use of inaccurate Fe^{3+} values. On one hand the good correlation that garnet-clinopyroxene geothermometry (T-KR88 and T-BE95) shows with pyroxene solvus geothermometry at low temperatures and with garnet-olivine geothermometry (T-OW79) for the whole temperature range suggests that garnet-clinopyroxene geothermometry is as accurate as the other conventional geothermometers.

On the other hand, the amount of Fe^{3+} in pyroxenes can be affected by an oxidation-dehydroxylation reaction of the form: $Fe^{3+} + O^{2-} + \frac{1}{2}H_2 = Fe^{2+} + OH^-$ (Skogby and Rossman, 1989). Pyroxenes and garnets, like most mantle phases, contain small amounts of hydrogen, structurally bound as hydroxyl (OH^-) (Bell and Rossman, 1992a). Pyroxenes are the most hydrous mantle phase, containing ~200-500 ppm H_2O by weight (Bell and Rossman, 1992a). Thus, if a significant amount of OH^- was removed from (or added to) the clinopyroxene structure since the equilibration of garnet and clinopyroxene, then the Fe^{3+} values measured by Mössbauer spectroscopy probably do not represent the Fe^{3+} at equilibration. Garnet Fe^{3+} values will not be significantly affected if the garnets were subjected to the same oxidation-dehydroxylation reaction. This is due to the fact that garnets in garnet peridotites generally contain only ~1 to 50 ppm H_2O by weight (Bell and Rossman, 1992a), with values as high as 135 ppm H_2O by weight in Cr-poor garnet megacrysts (Bell and Rossman, 1992b). Therefore, the use of inaccurate Fe^{3+} values rather than the inaccuracy of the garnet-clinopyroxene geothermometers is the most probable cause for the anomalous values in Fig. 6.5 c and d.

Therefore, it can be concluded that in comparison to T-BK2px, Fe^{2+}-Mg exchange geothermometers, including T-OW79, the geothermometer used in the calibration of

T-Ryan, probably underestimate equilibration temperatures by about 100 to 200°C at high temperatures (Fig. 6.3 and 6.5b), when Fe^{3+} in garnet is not taken into account.

6.3 Nickel geothermometry

Both the Ryan *et al.* (1996) and Canil (1994) Ni geothermometer calibrations yielded a wide range of temperature estimates for the Jagersfontein peridotites and a narrow range of temperature estimates for the Matsoku peridotites, similar to conventional geothermometry (Table 6.1). The two calibrations differed by not more than ±50°C for most of the samples and not by more than ±75°C for all peridotites with Ni abundances in garnet in the range of 38 to 90 ppm (Figure 6.6). This "38-90 ppm Ni content" range is equivalent to about 900 to 1200°C. Outside this range the two calibrations differed by between 75 and 150°C.

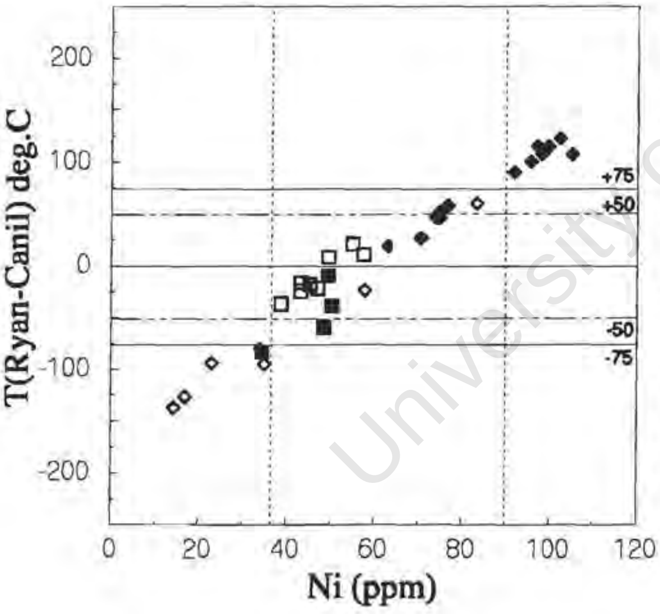

Fig. 6.6. A comparison of the Ni geothermometers, T-Ryan and T-Canil. The geothermometers agree, within error, at a Ni concentration range in garnet of 38 to 90 ppm. Above 90 ppm T-Ryan yields higher temperature estimates, but yields lower temperatures below 38 ppm in comparison to T-Canil. The apparent trend is due to the nature of the calibration lines for T-Ryan and T-Canil (e.g in Fig. 6.8): the calibration lines cross over at a Ni concentration of ~60 ppm; below and above this 60 ppm temperatures derived using the two calibrations increasingly differ as Ni, respectively, decrease and increase. Symbols are the same as in Fig. 6.1. The vertical lines mark the '38 to 90 ppm' Ni concentration range. The horizontal solid and dash-two dot lines respectively envelop the agreement to within ±75°C and ±50°C. Ni (ppm) = Ni concentration in garnet.

T-Canil gave Matsoku peridotites temperature estimates ranging from 998 to 1081°C (83°C range) , whereas T-Ryan yielded temperature estimates ranging from 927 to 1067°C (140°C range). However, there is no significant difference between T-Canil and T-Ryan temperature estimates for Matsoku peridotites: the difference between Ni geothermometry temperature estimates for all but one (LBM32) peridotites is not more than ±50°C (Fig. 6.6). This is due to the fact that these temperatures are well within the temperature range (~900 to 1200°C) where the two calibrations are in agreement.

T-Ryan yielded temperature estimates ranging from 721 to 1355°C (634°C range), whereas T-Canil yielded a more confined temperature range of 860 to 1221°C (361°C range) for Jagersfontein peridotites. These Ni geothermometers divided the Jagersfontein peridotites into high and low temperature peridotites, corresponding to deformed and coarse peridotites, respectively (Table 6.1). Similarly to the findings of Hops (1989) who used conventional geothermometry, Ni geothermometry estimates are positively correlated to increasing degree of deformation as indicated by textures. This is illustrated in Table 6.1 where samples are listed in increasing order of Ni concentration in garnet, and hence temperature. In general, with the exception of the dunite (JJH23) and the coarse J117, textures change from coarse to porphyroclastic to mosaic-porphyroclastic to fluidal mosaic porphyroclastic with increasing temperature.

6.4 Comparison of Ni and Conventional Temperature Estimates

A decision on which of the two Ni geothermometer calibrations agrees more with T-BK2px and the other conventional geothermometers should be mainly based on the assessment of the difference between the Ni geothermometers' temperature estimates and the conventional geothermometers' estimates outside the "38-90 ppm Ni content" range. This is where the discrepancy between these calibrations is most apparent (Fig. 6.6).

The first approach followed in this study involved an assessment of the ability of the Ni geothermometers to reproduce temperature estimates made using T-BK2px_P-BK90 and the other conventional geothermobarometers for each of the peridotites studied. The second approach involved looking at the peridotites as a group, and plotting conventional geothermobarometer temperature estimates against garnet Ni content determined by PIXE. Regression lines through data, using the method of least squares on all data points, were then compared to the calibration lines of the two Ni geothermometers. In effect this investigated the affect that using T-BK2px and the other geothermometers might have if used to calibrate the Ni geothermometer.

6.4.1 Ni geothermometers vs pyroxene solvus geothermometers

T-Ryan reproduced T-BK2px temperature estimates better than did T-Canil. For all the peridotites with greater than 50 ppm Ni in garnet, T-Ryan reproduced T-BK2px_P-BK90 temperature estimates to within ±75^{0}C and to within ±50^{0}C for the majority of these peridotites (Fig. 6.7a). However, below 50 ppm the difference between T-Ryan and T-BK2px temperatures is up to 200^{0}C. T-Canil is in poor agreement with T-BK2px_P-BK90, yielding temperatures that are 80 to 200^{0}C lower than T-BK2px temperature estimates for most of the peridotites (Fig. 6.7b). The regression line through temperatures estimated using T-BK2px_P-BK90 has a slope similar to that of the T-Ryan calibration line for Ni concentration of less than 100 ppm (Fig. 6.8a). Above this Ni concentration this regression line would yield temperatures that are 75^{0}C or more, higher than the T-Ryan calibration line temperature estimates.

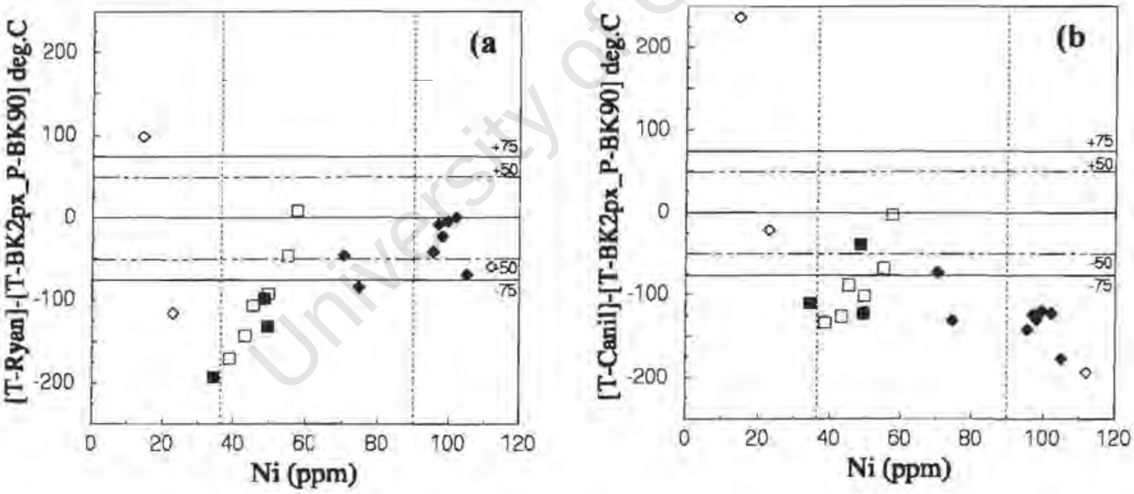

Fig. 6.7. A comparison of Ni geothermometry with T-BK2px_P-BK90 temperature estimates. The symbols are the same as in Fig. 6.1. The lines are the same as in Fig. 6.6. Ni (ppm) = Ni. concentration in garnet.

The correlation between T-FB87_P-MG74 and T-Ryan temperature estimates (Fig. 6.9a) is similar to the correlation between T-BK2px and T-Ryan (Fig. 6.7a). The difference between T-FB87 and T-Ryan is insignificant (<50^{0}C) for peridotites with greater than 55 ppm Ni concentrations in garnet. Below this Ni concentration differences of up to 175^{0}C between the temperatures estimates were observed. T-

Canil is in poor correlation with T-FB87 for Ni concentrations in garnet of more than 90 ppm (Fig. 6.9b); the temperature differences between the temperature estimates calculated by these geothermometers are between 90 and 160°C. For Ni abundances that are less than 90 ppm the correlation between T-Canil and T-FB87 is good for most of the peridotites (difference in temperature estimates of less 50°C) but poor for a few of the samples (difference in temperature estimates of between 90 and 150°C). The regression line through temperatures estimated using T-FB87 has a slope similar to that of the T-Ryan calibration line for Ni-in-garnet of greater than 30 ppm (Fig. 6.10a). Below 30 ppm the two lines deviate markedly.

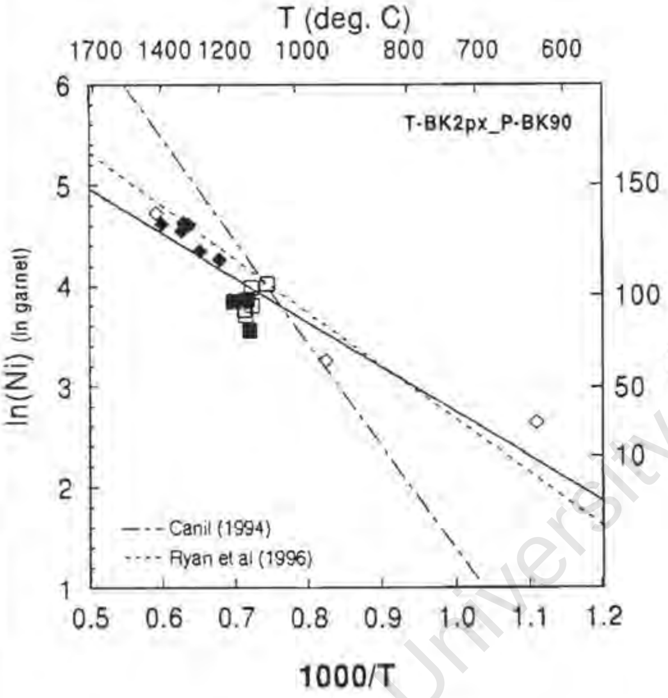

Fig. 6.8. A comparison of the calibration lines of the Ni geothermometers with the regression line (the solid line) through temperature estimates made using T-BK2px_BK90. The equation of this regression is as follows:

$$\mathbf{T(K) = -4367 \div [\ln(ppmNi_{gt}) - 7.13]}$$

The symbols are the same as in Fig. 6.1. The dash-three dot line represents the T-Canil calibration line and the dash line represents the T-Ryan calibration line as plotted by Griffin and Ryan (1996).

Although T-BM85_P-NG85 is in good agreement with T-Ryan (Fig. 6.9c), it is also, except at the lowest temperature end, in agreement with T-Canil (Fig. 6.9d). The regression line through temperatures calculated by T-BM85 has a slope that is the same as that of the T-Ryan calibration line for the whole Ni concentration range studied (Fig. 6.10b).

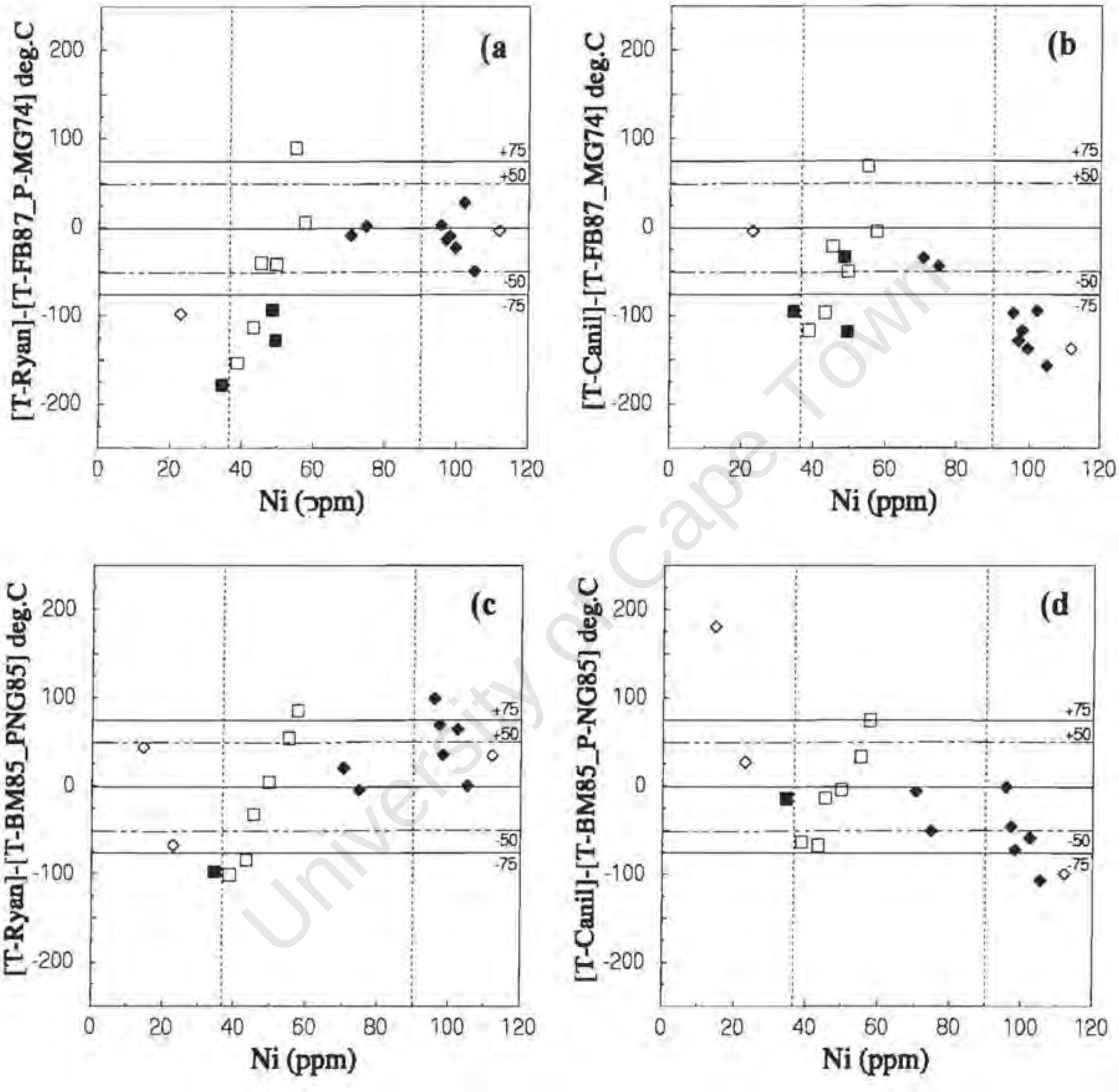

Fig. 6.9. A comparison of Ni geothermometry with pyroxene solvus geothermometry. a) T-Ryan is compared to T-FB87_P-MG74; b) T-Canil is compared to T-FB87_P-MG74; c) T-Ryan is compared to T-BM85_P-NG85; and d) T-Canil is compared to T-BM85_P-NG85. The symbols are the same as in Fig. 6.1. The lines are the same as in Fig. 6.6. Ni (ppm) = Ni concentration in garnet.

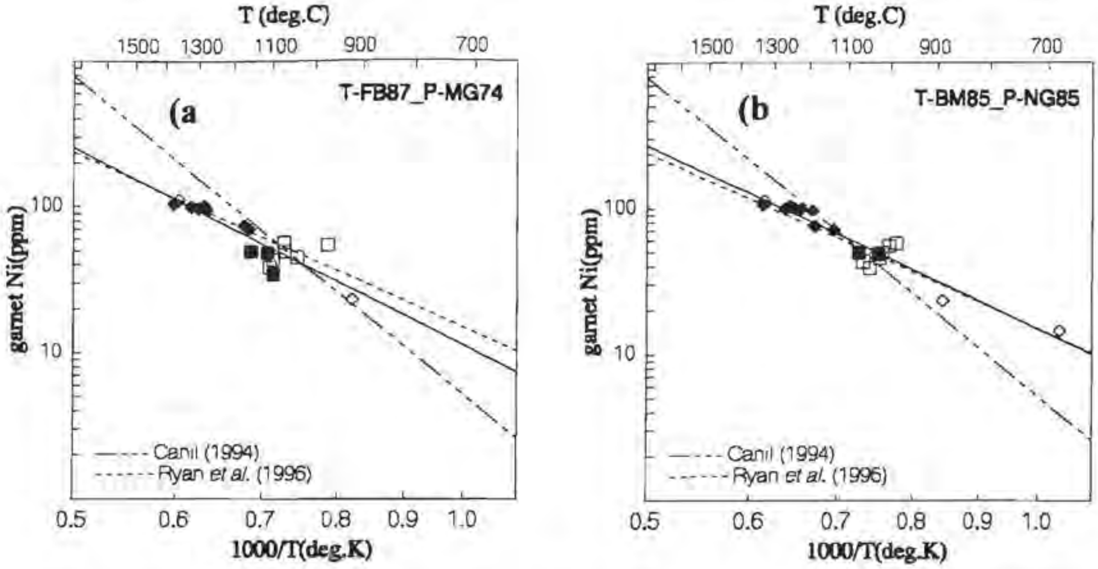

Fig. 6.10. A comparison of the calibration lines of the Ni geothermometers with the regression lines (the solid lines) through temperature estimates made using pyroxene solvus geothermometry; a) T- FB87_P-MG74 and b) T-BM85_P-NG85. The symbols are the same as in Fig. 6.1. The dash-three dot line and the dash line are the same as in Fig. 6.8.

6.4.2 Ni vs Fe^{2+}-Mg exchange geothermometers

Although not entirely satisfactory, T-Canil temperature estimates are in better agreement with the temperatures derived using T-KR88_P-BK90 (Fig. 6.11b) than are the temperatures derived using T-Ryan (Fig. 6.11a). The regression line through temperatures estimated using T-KR88_P-BK90 has a slope similar to that of the T-Ryan calibration line (Fig. 6.12a). However, it should be noted that the slope of this regression line is to a large degree controlled by data points at the low and high ends of the temperature range.

T-Canil correlates reasonably well with T-BE95_P-BK90. The difference between the temperature estimates is not more than 75^{0}C for the majority of the peridotites (Fig. 6.11d). In contrast, a poor agreement exists between T-Ryan and T-BE95_P-BK90 (Fig. 6.11c), especially outside the "38 to 90 ppm Ni content" range where the difference between the temperature estimates are up to 190^{0}C. The regression line through T-BE95_P-BK90 temperature estimates has a slope that is similar to that of the T-Ryan calibration line (Fig. 6.12b). However, this regression line is also to a great degree controlled by data points at the lowest and highest ends of the temperature range.

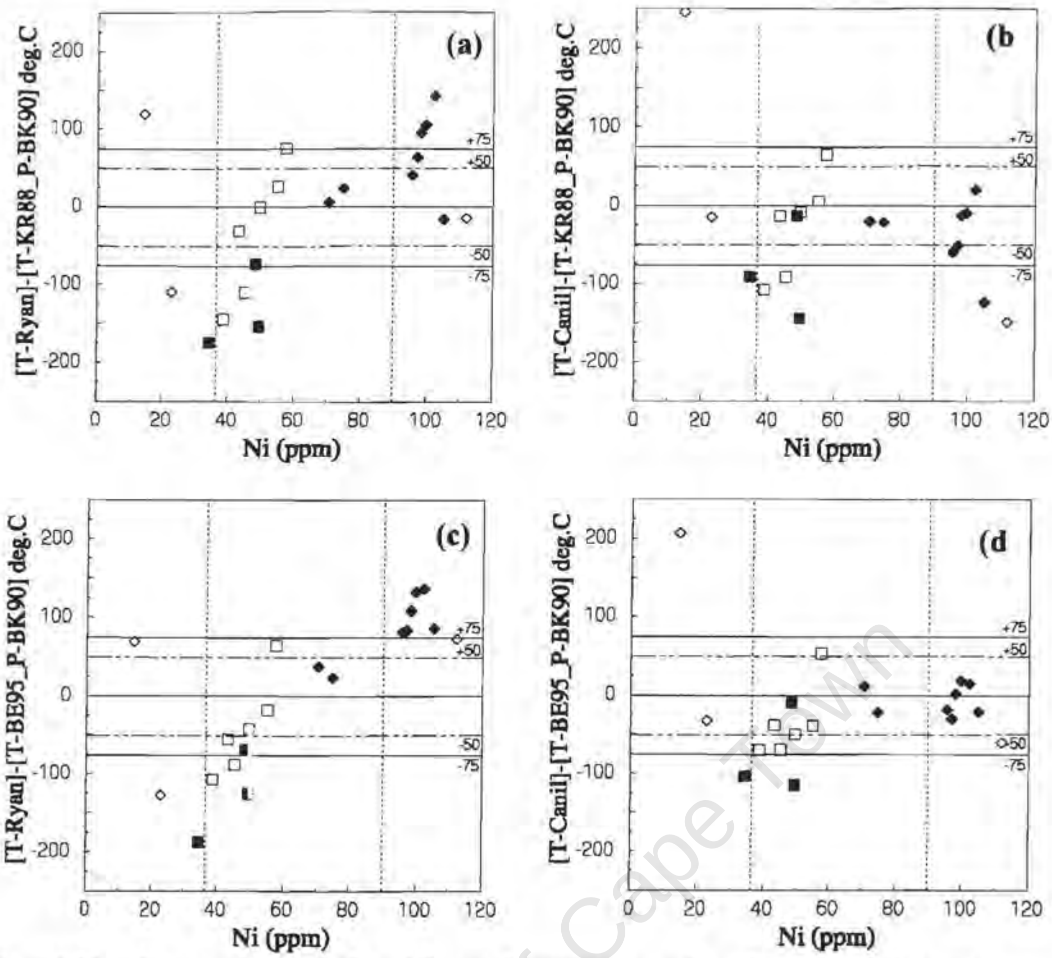

Fig. 6.11. A comparison of Ni geothermometry with the garnet-clinopyroxen geothermometry. a) T-Ryan is compared to T-KR88_P-BK90; b) T-Canil is compared to T KR88_P-BK90; c) T-Ryan is compared to T-BE95_P-BK90; and d) T-Canil is compared to T BE95_P-BK90. The symbols are the same as in Fig. 6.1. The lines are the same as in Fig. 6.6 Ni (ppm) = Ni concentration in garnet.

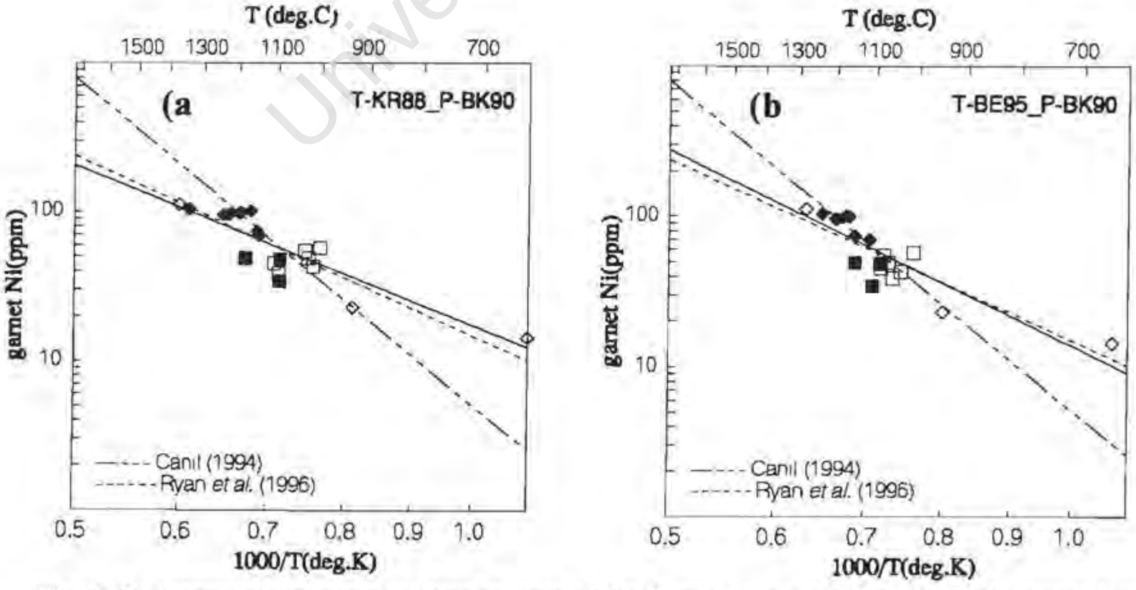

Fig. 6.12. A comparison of the calibration lines of the Ni geothermometers with the regression lines (the solid lines) through temperature estimates made using the garnet-clinopyroxene geothermometers, a) T-KR88_P-BK90 and b) T-BE95_P-BK90. The symbols are the same as in Fig. 6.1. The lines are the same as in Fig. 6.8.

Temperatures estimated using the garnet-olivine geothermometer of O'Neill and Wood (1979, 1980), T-OW79, were used in the empirical calibration of T-Ryan. Thus T-Ryan was expected to reproduce temperatures calculated by T-OW79 for the whole Ni concentration range. However, for the samples in this study, a correlation between T-OW79 and T-Ryan is best only for peridotites with less than 38 ppm Ni concentrations in garnet, good for Ni concentrations in the 38 to 90 ppm range, and poor for Ni concentrations of greater than 90 ppm (Fig. 6.13a). With the exception of one peridotite, the difference between T-Canil and T-OW79_P-MG74 temperature estimates is less 50^0C for greater than 90 ppm Ni concentrations in garnet (Fig. 6.13b).

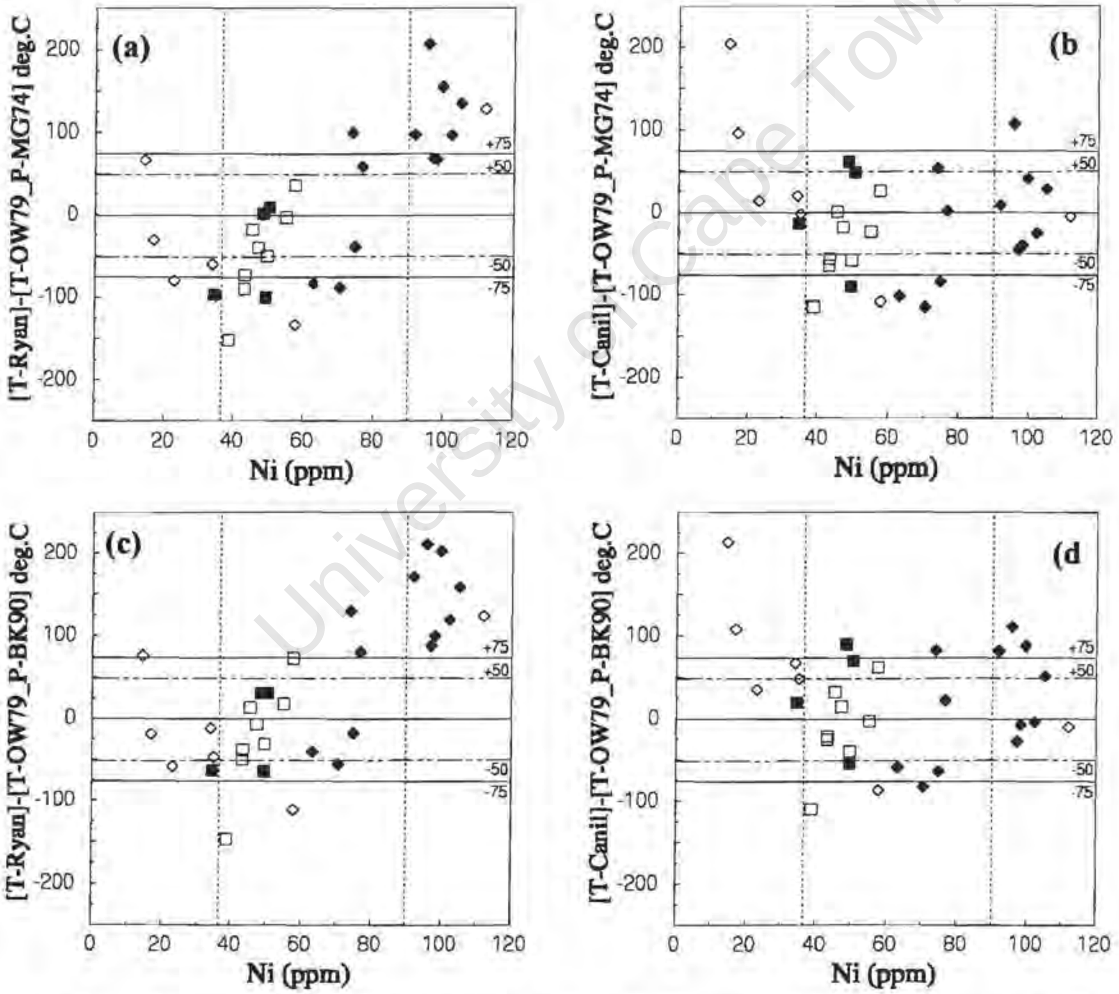

Fig. 6.13. A comparison of Ni geothermometry with the garnet-olivine geothermometry of O'Neill and Wood (1979, 1980); a) and b) Ni geothermometers are compared to T-OW79_P-MG74; c) and d) Ni geothermometers are compared to T-OW79_P-BK90. The symbols are the same as in Fig. 6.1. The lines are the same as in Fig. 6.6. Ni (ppm) = Ni concentration in garnet.

For less than 90 ppm Ni concentrations the correlation between T-Canil and T-OW79_P-MG74 is poor and temperature differences are up to 200^0C at the lowest end of the Ni concentration range. Similar results were found when the Ni geothermometers were compared to T-OW79_P-BK90, with a slight improvement in the correlation for less than ~60 ppm Ni concentration (Figs. 6.13c and d). As expected, the regression line through T-OW79_P-MG74 temperature estimates mimics the T-Ryan calibration line (Fig. 6.14a). This regression is to a large degree controlled by the low temperature data points. However, as noted by Canil (1996), the $\pm113^{0}$C uncertainty associated with T-OW79 (Brey and Köhler, 1990) could shift the calibration line towards the T-Canil calibration line (Fig. 6.14a). Using T-OW79_P-BK90 causes a slight deviation between these two lines at high temperatures (Fig. 6.14b).

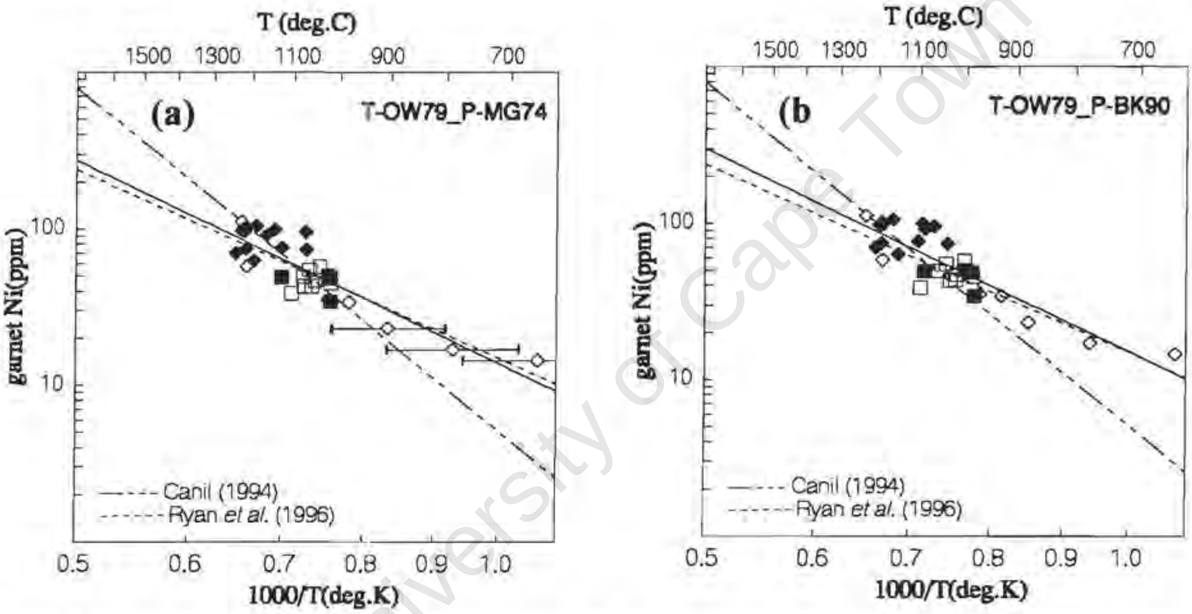

Fig. 6.14. A comparison of the calibration lines of the Ni geothermometers with the regression line (the solid line) through temperature estimates made using the garnet-olivine geothermometer of O'Neill and Wood (1979, 1980), a) T-OW79_P-MG74 and b) T-OW79_P-BK90. The symbols are the same as in Fig. 6.1. The lines are the same as in Fig. 6.7. The error bars in (a) are $\pm113^{0}$C uncertainty associated with T-OW79 (Brey and Köhler, 1990).

6.5 Discussion

It has been shown that when applied to the peridotites under study, results obtained by Fe^{2+}-Mg exchange and by pyroxene solvus geothermometry display a disparity similar to that observed between T-Canil and T-Ryan at high temperatures (> 1200^{0}C; > 90 ppm Ni-in-garnet) (Figs. 6.3, 6.11 and 6.13). At these temperatures T-Canil correlates very well with Fe^{2+}-Mg geothermometry (T-OW79, Fig. 6.13b and d; T-KR88, Fig. 6.11b; T-BE95, Fig. 6.11d). In contrast, T-Ryan is in good correlation with pyroxene solvus geothermometry (T-BK2px, Fig. 6.7a; T-FB87, Fig. 6.9a; T-BM85, Fig 6.9c). Thus, it seems the divergence of the Ni geothermometers at high temperatures may be resolved by an assessment of the accuracy of pyroxene solvus and Fe^{2+}-Mg geothermometry at these temperatures.

It was also conclude that Fe^{2+}-Mg exchange geothermometers probably underestimate temperatures by ~100 to 200^{0}C at high temperatures. If this 'underestimation' is added to the temperatures derived using the Fe^{2+}-Mg exchange geothermometers the correlation of these geothermometers with T-Ryan at high temperatures can be improved markedly. This is of course dependent on the results found on only seven of the samples in this study and more importantly on how close the Fe^{3+} estimates used are to the real values in the samples. This "improvement" would be surprising for T-OW79 since Ryan *et al.* (1996) did not determine Fe^{3+} contents of the samples they used to develop T-Ryan. It is again[14] impossible to speculate on the reasons for this observation when the Fe^{3+} values for the samples used in this study, for the samples used the T-OW79 experiments and for the samples used in the development of T-Ryan are not known. However, it does appear that T-Ryan is in agreement at high temperatures with pyroxene solvus geothermometry and with Fe^{2+}-Mg exchange geothermometry corrected for the 'underestimation'. In contrast, the addition of the temperature 'underestimation' could weaken the correlation between T-Canil and Fe^{2+}-Mg geothermometry in Figs. 6.11b, 6.11d and 6.13b.

Only two of the low temperature (<900^{0}C) peridotites used in this study contain clinopyroxene. Therefore, an evaluation of Ni geothermometry at low temperatures using pyroxene solvus geothermometry cannot be conclusive. However, pyroxene solvus geothermometry yields temperatures that correlate well (within ±50 ^{0}C) with Fe^{2+}-Mg exchange geothermometry estimates for both these samples (Fig. 6.3). This suggests that geothermometry based on Fe^{2+}-Mg exchange is as accurate at low temperatures as the pyroxene solvus geothermobarometry and can thus be used to assess Ni geothermometry.

---

[14] See section 6.2.2

It was shown earlier that at low temperatures T-OW79 is in better agreement with T-Ryan than with T-Canil (Figs. 6.13). This agreement indicates that at low temperatures T-Ryan is in agreement with both the Fe^{2+}-Mg exchange and the pyroxene solvus geothermometry.

Finally, regression lines through temperature estimates made using T-BK2px and all the other conventional geothermometers chosen for use in this study are closely in agreement with the T-Ryan calibration line and not with the T-Canil calibration line. However, regression lines should be applied with caution in the intermediate range of a dataset because they tend to be biased towards data at the lowest and highest extremes of a data range. Considering that the two Ni geothermometer calibrations yield temperature estimates that increasingly differ at the lowest and highest temperature extremes (Fig. 6.6), regression lines should work well for the present study. Therefore, the use of any of the geothermometers chosen for this study in the calibration of the Ni geothermometer would produce a calibration line that has a slope that is relatively closer to that of the T-Ryan calibration line than to that of the T-Canil calibration line.

Chapter 7

7. Discussion and Conclusions

7.1 Introduction

Pressure-temperature (P,T) arrays have been widely used as representations of the thermal state of the mantle at the time of the eruption of host kimberlites and other alkaline volcanic rocks. From these P,T arrays or geotherms, the depth from which the xenoliths were sampled by kimberlites can be calculated. This information places in a spatial context petrographic and geochemical data of mantle phases and their host rocks. Furthermore, geotherms calculated in this manner can play a major role in target area selection during diamond exploration.

In Chapter 6 it was shown that the empirical calibration of the Ni geothermometer (T-Ryan) best reproduced temperatures derived using the geothermometer preferred in this study (T-BK2px) and other commonly used geothermometers. In contrast, the experimental calibration of the Ni geothermometer (T-Canil) did not adequately reproduce these temperatures. One approach of assessing the usefulness of T-Ryan and P-Cr is to evaluate geotherms produced by this geothermometer and compare them with the geotherms derived using the generally accepted conventional geothermobarometers ("xenolith-derived geotherms"[16]).

Xenolith-derived geotherms were calculated using the preferred geothermobarometer, T-BK2px_P-BK90, and the other combinations applied in Chapter 6. Matsoku peridotites were sampled from the same depth and have similar temperature estimates (Chapter 6) and thus P,T arrays for the xenoliths from this locality cannot, on their own, define a geotherm. However, there are reasons to believe that both Matsoku and Jagersfontein kimberlites sampled a mantle with the same thermal structure: Matsoku and Jagersfontein are both Group I kimberlites, have

---

[16] Geotherms that are defined using P,T estimates derived using geothermobarometers based on element exchange between coexisting mineral phases.

similar intrusion ages, and both intruded close to the edge of the Kaapvaal craton (Chapter 2). Thus the P,T estimates for these two localities were plotted and interpreted concurrently.

7.2 Geothermal Gradients

7.2.1 Xenolith-derived Geotherms

Although showing some scatter, the preferred geothermobarometer combination, T-BK2px_P-BK90 and the other geothermobarometers recommended by Brey and Köhler (1990) (T-KR88_P-BK90 and T-OW79_P-BK90, section 5.4) yielded P,T arrays that are consistent with a geotherm that is slightly elevated to higher temperatures relative to the 40 mW/m^2 continental geotherm of Pollack and Chapman (1977) (Fig 7.1). The P,T estimates scatter around a ~43 mW/m^2 geotherm, without an inflected high temperature section.

Using T-BK2px_P-BK90 (Fig. 7.1a) the coarse peridotite, J117, has the highest P,T estimates, and is placed at a depth of ~220 km. The temperature estimate for the modally metasomatised peridotite, JJG1733, made using the same combination, is outside the temperature range (900-1400^{0}C) of the experiments of Brey *et al.* (1990). Nevertheless, this xenolith has P,T estimates that placed it on the ~43 mW/m^2 geotherm (Fig. 7.1a).

The biggest scatter in data was observed when P,T estimates were made using the T-OW79_P-BK90 geothermobarometer combination (Fig. 7.1c). However, the geotherm produced is similar to the geotherms yielded by the other two geothermobarometer combinations above, with most of the P,T estimates plotting close to a ~43 mW/m^2 continental geotherm.

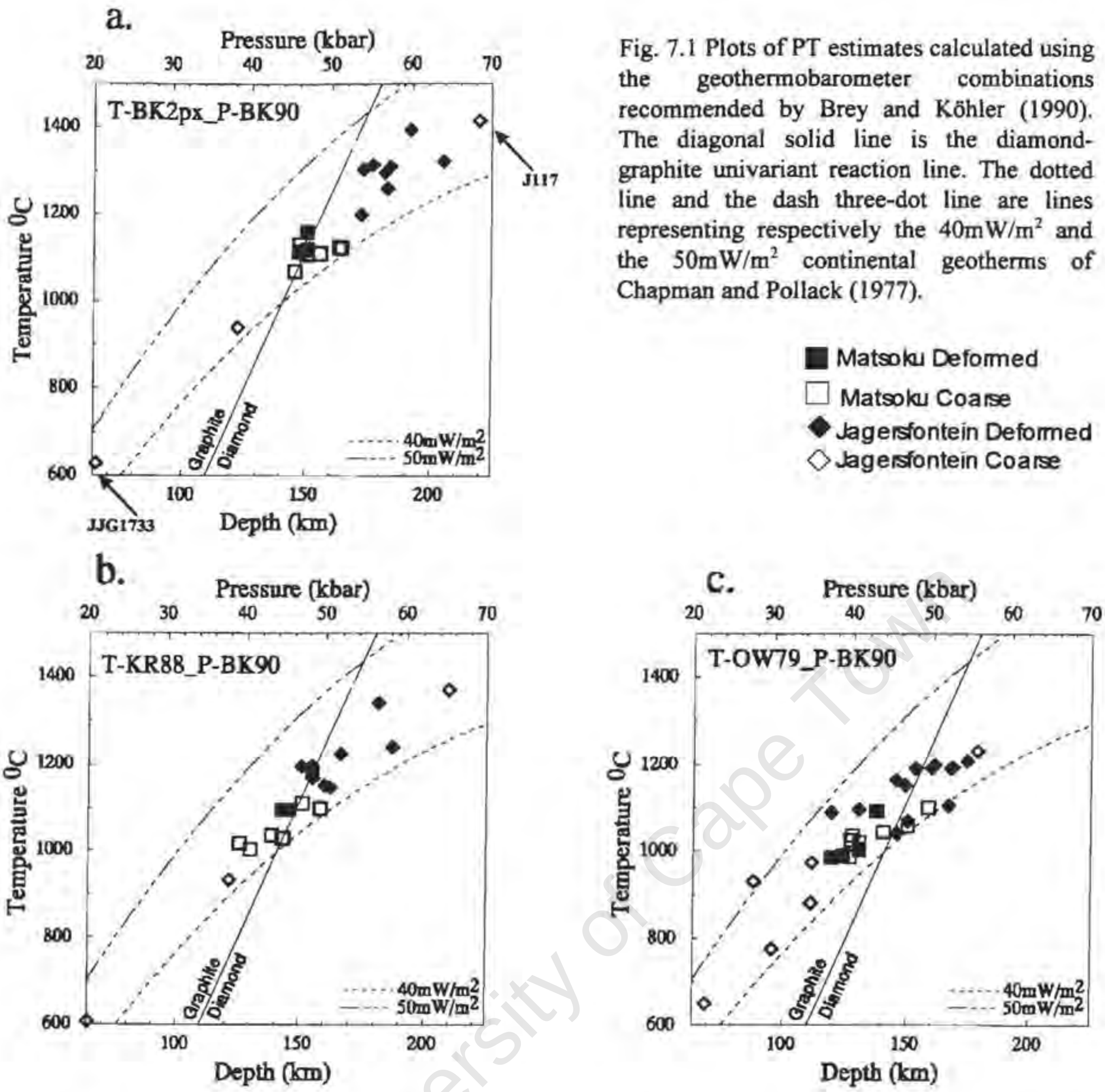

Fig. 7.1 Plots of PT estimates calculated using the geothermobarometer combinations recommended by Brey and Köhler (1990). The diagonal solid line is the diamond-graphite univariant reaction line. The dotted line and the dash three-dot line are lines representing respectively the 40mW/m^2 and the 50mW/m^2 continental geotherms of Chapman and Pollack (1977).

The geothermobarometer combination T-FB87_P-MG74, recommended by Finnerty and Boyd (1987), produced an 'inflected' geotherm (Fig. 7.2a). The point of inflection occurs at about 190 km. The low temperature peridotites plotted on the 40 mW/m^2 continental geotherm. The high temperature peridotites plotted at a confined pressure range (60 to 63 kb) and temperatures that are elevated to higher temperatures from the 40 mW/m^2 continental geotherm.

The combination T-BM85_P-NG85 produced a P,T array which is consistent with a ~43 mW/m^2 geotherm for low temperature peridotites (Fig. 7.2b). High temperature peridotites had a confined pressure estimates (49 to 54 kb) but varying temperature estimates, producing an inflected geotherm with a point of inflection at a depth of ~160 km. The combination T-OW79_P-MG74 yielded a P,T array that is consistent with the 40 mW/m^2 geotherm (Fig. 7.2c). The geothermobarometer T-BE95_P-BK90 produced P,T estimates that scatter around a ~43 mW/m^2 geotherm (Fig. 7.2d).

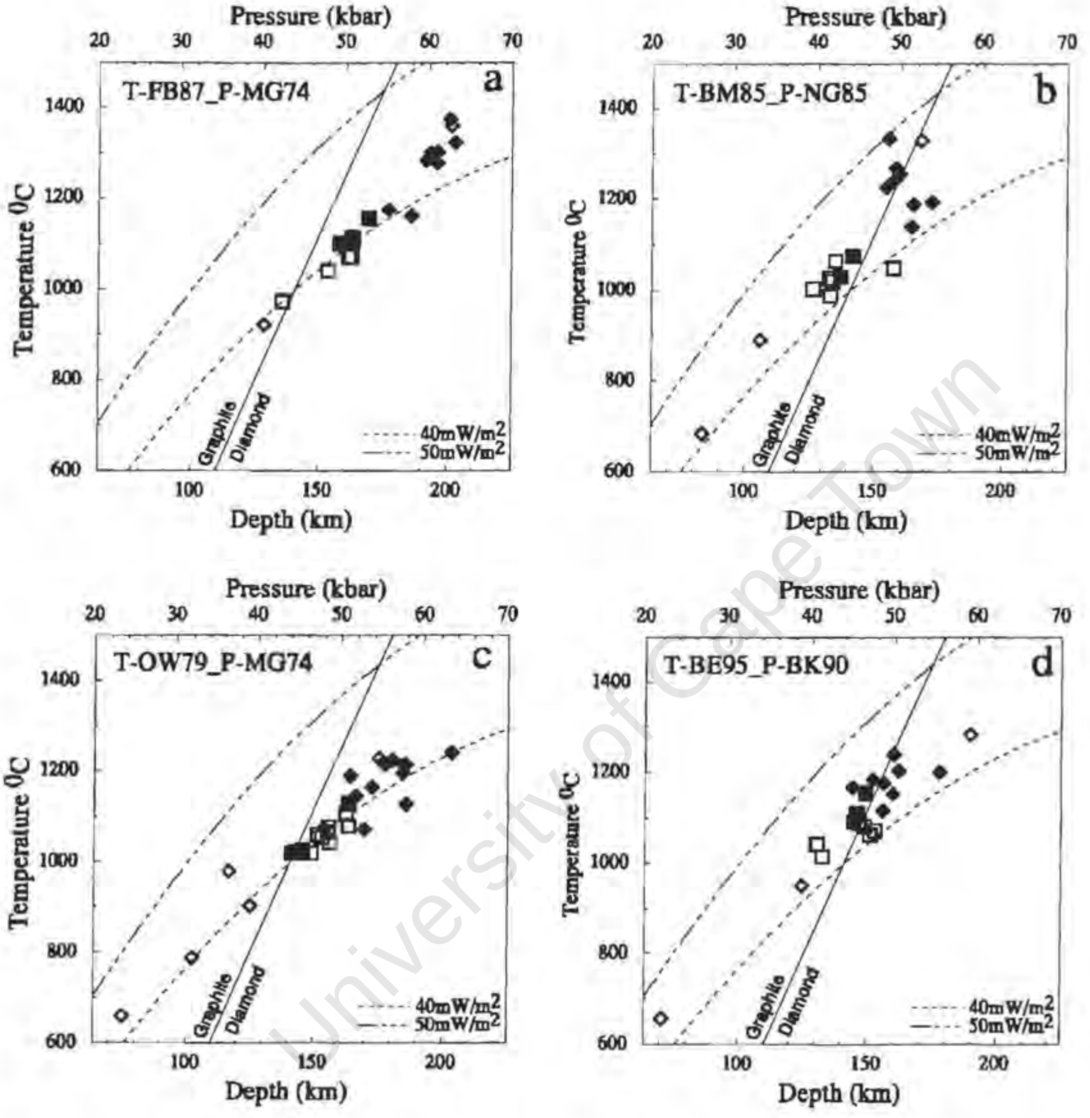

Fig 7.2 PT plots with T estimates calculated using pyroxene solvus geothermometry (a and b) and Fe-Mg geothermometry (c and d). The lines and the symbols are as in Fig. 7.1.

7.2.2 The 'Garnet Geotherm'

The 'garnet geotherm' is produced by plotting P,T estimates calculated using the chrome barometer, P-Cr and T-Ryan. Following this method, the locus of the maximum pressure estimates derived using P-Cr over the calculated temperature range is taken to define a local geotherm. The pressure estimates are only accurate for

Cr pyrope garnets that coexisted with orthopyroxene in Cr-saturated conditions, i.e. where chromite was present to buffer Cr in orthopyroxene (Ryan *et al.*, 1996). Therefore, the method produces realistic pressure estimates only for chromite-bearing peridotites and underestimates pressures (Ryan *et al.*, 1996) for chromite-free peridotites. 'True' pressure estimates for the chromite-free peridotites can be found by projecting their T-Ryan temperatures onto the 'garnet geotherm' (Ryan *et al.*, 1996).

For the peridotites under study the locus of maximum pressures is defined by three coarse chromite-bearing peridotites, and produced a P,T array that is consistent with the 40 mW/m^2 continental geotherm (Fig. 7.3). However, three other chromite-bearing peridotites do not plot on the 40 mW/m^2 geotherm. Two of these peridotites plot on a higher geotherm (~43 mW/m^2). The third one has a pressure estimate that is too low for its temperature estimate. However, using this limited number of samples the 'garnet geotherm' appears to be consistent with a geotherm that has a heat flow of between 40 and 43 mW/m^2.

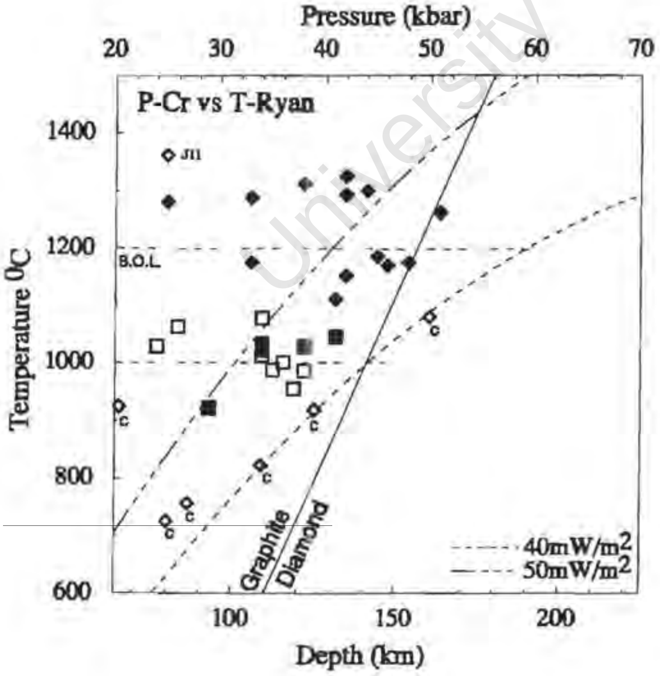

Fig. 7.3 A PT plot of the Cr barometer pressure estimates against the temperature estimates derived using the experimental Ni geothermometer. "B.O.L." = base of lithosphere (section 7.3 and Fig. 7.5). The horizontal three-dot lines envelopes the 'diamond window' (section 7.3). The other lines and symbols are the same as in Fig. 7.1. C = chromite-bearing peridotite.

This geotherm is defined only up to ~1100 ^{0}C. Griffin and Ryan (1995) and Ryan *et al.* (1996) noted that chromite-bearing rocks are rare in the cratonic mantle at temperatures greater than 1100 ^{0}C. These authors suggested that as pressure increases Cr is progressively incorporated into garnets and pyroxene, until the rock is Cr-undersaturated and chromite disappears. Therefore, it is unlikely that high temperature deformed peridotites will contain chromite, and thus this method will not produce realistic pressure estimates for such peridotites.

For further assessment, temperatures calculated using T-Ryan were used to estimate pressures using the preferred geobarometer, P-BK90. These temperatures were plotted against the resultant pressure estimates to determine the palaeogeotherm (Fig. 7.4). The P,T estimates are scattered at temperatures that are higher than the 40 mW/m^2 continental geotherm but are on average consistent with 43 mW/m^2 geotherm.

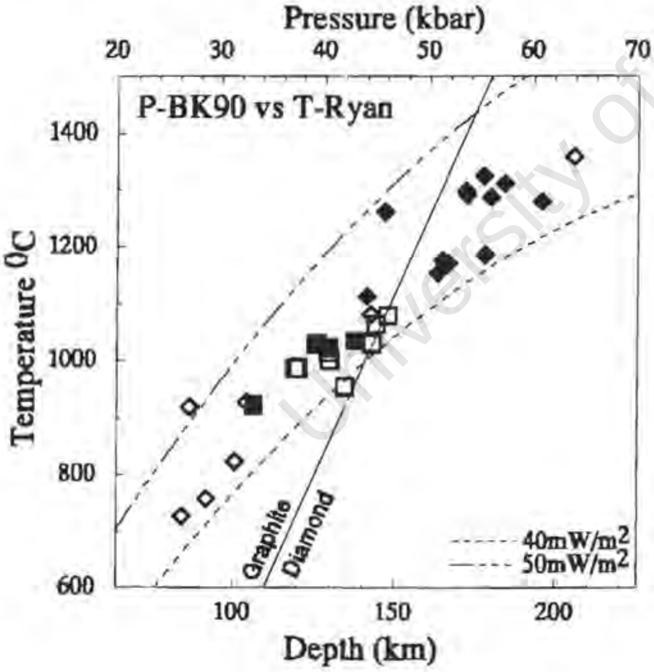

Fig. 7.4 PT plots of P-BK90 pressure estimates, calculated at T-Ryan against the Ni geothermometer temperature estimates. The lines and the symbols are the same as in Fig. 7.1.

7.3 'Use' of trace elements in diamond exploration

Griffin and Ryan (1995) noted that depleted levels of Zr, Y and Ti occur in Cr pyrope garnets from low temperature peridotites, whereas elevated levels occur in Cr pyrope garnets from high temperature peridotites. The trace (and major) element enrichment signatures in high temperature garnets have been interpreted as a manifestation of the interaction of asthenospheric metasomatic melts with mantle peridotite wall rocks just before the entrainment of the peridotites to the Earth's surface (e.g., Griffin *et al.*, 1989b; Smith and Boyd, 1987).

Griffin and Ryan (1995) suggested that, in temperature-chemistry plots, a distinct edge formed by a line marking the highest temperature at which the depleted Cr pyropes occur, represents the temperature at the base of the lithosphere ("B.O.L."). They also noted that where data are available, the "B.O.L." corresponds to the kink in inflected xenolith-derived geotherms, and to the highest temperature at which Cr-rich garnets are found. They then defined a 'diamond window' as a P,T range above the intersection of the graphite-diamond univariant reaction line (Kennedy and Kennedy, 1976) and the local geotherm, but below the temperature at the "B.O.L." (Fig. 7.3).

The manner in which kimberlites sample the mantle on their way to surface is not well understood and the range of xenoliths found in each kimberlite does not necessarily represent the whole lithology of the mantle traversed by the kimberlite. Examples of some of the extreme cases of limited depth of sampling are the Matsoku kimberlite where xenoliths recovered are from essentially the same P,T conditions, and the Roberts Victor kimberlite where more than 90% (Hatton, 1978) of the xenoliths found are eclogites. Mantle phases occurring as xenocrysts in kimberlites and recovered as heavy mineral concentrates from stream sediment and soil samples or from the mineral separates of kimberlite samples can usually be geochemically classified to various mantle rock types, including those not found as xenoliths in the same kimberlite that hosted the xenocrysts (Boyd and Gurney, 1986). Thus, a full assessment of the mantle material sampled by a kimberlite and the determination of the "B.O.L" should not be based on the examination of xenolith samples but rather on the study of mineral concentrate material.

However, the wide range in P,T conditions of equilibration of the Jagersfontein peridotites may indicate these peridotites closely represent the majority of the various parts of the mantle traversed by this kimberlite. Therefore, using the method of

Griffin and Ryan (1995), the "B.O.L." beneath Jagersfontein is at a T-Ryan temperature estimate of ~1200^{0}C (Fig. 7.5). At this temperature a distinct division between Ti-enriched (TiO_2 > 0.3 wt %) and Ti-depleted (TiO_2 < 0.2 wt %) Cr pyropes was observed (Fig. 7.5a). This 'B.O.L. is not evident when plots of T-Ryan against Zr and Y are used (Figs. 7.5b and c).The "B.O.L." defined by Ti-enrichment approximates the points of inflection derived using T-FB87_P-MG74 and T-BM86_P-NG85 geothermobarometers (Figs. 7.2a and b). As shown in Chapter 6, Matsoku peridotites are from a very restricted temperature range and this method of determining the "B.O.L." would not work for this locality.

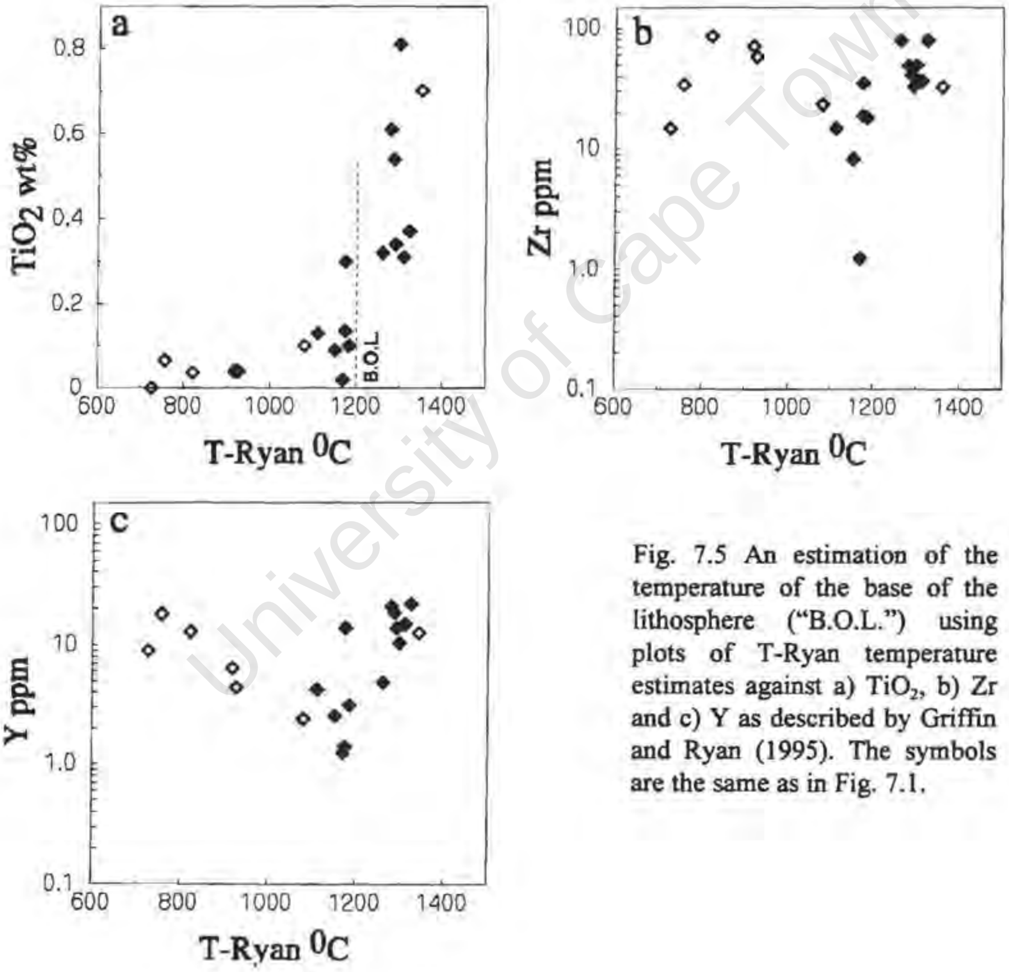

Fig. 7.5 An estimation of the temperature of the base of the lithosphere ("B.O.L.") using plots of T-Ryan temperature estimates against a) TiO_2, b) Zr and c) Y as described by Griffin and Ryan (1995). The symbols are the same as in Fig. 7.1.

Griffin and Ryan (1995) have also developed a method of target selection and evaluation based on the trace element content of Cr pyropes from disaggregated mantle peridotites recovered as mineral concentrates. They suggested that, when combined with the local geotherm, Ni geothermometry can be used to qualitatively indicate whether a kimberlite or other intrusive is likely to be diamond-bearing or not.

After the determination of the local geotherm and the 'diamond window' the method of Griffin and Ryan (1995) of target selection involves the assessment of the diamond potential using Cr pyrope garnets that were sourced from within the 'diamond window'. This includes an assessment of the proportion of the garnets that plot inside the "diamond window" and an evaluation of the Zr content of these garnets which, according to Griffin and Ryan (1995), serves as an indication of metasomatism and possible destruction of diamonds.

Griffin and Ryan (1995) thus defined a parameter Ω, which they claim reflects both the degree of sampling of potentially diamondiferous mantle and the destructive effects of the interaction of metasomatic (asthenospheric) melts with the wall rock mantle. Ω is defined as [(% of garnets with T-Ryan plotting in the 'diamond window') - (% of garnets with T-Ryan > the 'diamond window')]. Griffin and Ryan (1995) claim that the higher the Ω value the better the diamond grade. These authors also report to have found a negative linear relationship between grade and the *median Zr* content of garnets in the 'diamond window': high *median Zr* values were associated with low grades. As pointed out earlier, the samples used in this study do not fully represent the mantle traversed by the kimberlites studied and thus cannot be used to assess the this method on the two localities under study.

However, the variation of Zr (and Ga, Ti and Y) in garnets (and in other phases) may be related to metasomatism and/or depletion (Griffin *et al.*, 1992) of peridotites. On one hand metasomatic melts infiltrating the peridotite lithosphere may bring in these trace elements, thereby enriching the peridotites. On the other hand, removal of partial melts from the peridotite mantle may deplete the peridotites in these trace elements. Therefore, low Zr values (and thus low *median Zr* values) may exist in highly depleted peridotites and may have nothing to do with the degree of metasomatism and diamond destruction or preservation.

Moreover, diamond destruction or resorption has been associated with the oxygen fugacity (oxygen activity) of its host rocks estimated using the composition of ilmenite (Mitchell, 1986). High oxygen activity (and thus oxidising conditions) in the carrier magma provides sufficiently rapid kinetics of the reactions required for conversion of diamond to graphite or CO_2 (Gurney and Moore, 1991). These redox conditions have been estimated using the Fe^{3+}/Fe^{2+} ratios in ilmenites: low Fe^{3+}/Fe^{2+} ratios occur in richer kimberlites, whereas high Fe^{3+}/Fe^{2+} ratios are found in ilmenites from barren kimberlites (Gurney and Moore, 1991). High Zr contents [and high temperatures, as noted by Kjarsgaard (1992)], do not necessarily imply high oxygen fugacities.

7.4 Summary of Conclusions

The main objectives of this study have been met using the two well characterised sample suites from Matsoku and Jagersfontein kimberlites. The one main objective, i.e. to obtain a high quality Ni in garnet dataset, has been met by comparison of data determined by PIXE, LA-ICP-MS and SIMS. These data were then used in Ni geothermometry, to meet the other main objective, which was to compare Ni and conventional geothermometers. The conclusions of this study can be summarised as follows:

- Under the analytical conditions used, LA-ICP-MS analyses are superior in terms of rapidity of analysis and ease and quick sample change. However, PIXE has an advantage of smaller beam width (5-10 μm in comparison to ~ 60 μm in LA-ICP-MS) allowing several repeat analyses on each garnet and analysis of small (<60μm) garnet grains.
- There is a strong agreement between PIXE and LA-ICP-MS in the determination of trace Ni, Zr and Y abundances.
- The poor quality of SIMS data (in terms of the number of repeat analyses) prevented proper comparison of these data with data determined by the other techniques. However, the results are promising in particular for trace Ni determination by SIMS, which has in the past been avoided because of spectral interferences.

- The empirical calibration of the Ni geothermometer, T-Ryan, reproduced temperatures determined by the preferred geothermobarometer, T-BK2px_P-BK90, and by the other geothermobarometers based on pyroxene solvus geothermometry, T-BM85_P-NG85 and T-FB87_P-MG74. This Ni geothermometer also reproduced temperatures determined by geothermobarometers based on Fe^{2+}-Mg exchange geothermometry (T-BE95_P-BK90; T-KR88_P-BK90; T-OW79_P-BK90), if these geothermometers are assumed to underestimate temperatures at high temperatures.
- The experimental calibration of the Ni geothermometer, T-Canil, did not adequately reproduce these temperatures. In comparison to T-Ryan and T-BK2px, T-Canil underestimates temperatures at high temperatures and overestimates temperatures at low temperatures.
- Using T-BK2px to calibrate the Ni geothermometer (as suggested by Kjarsgaard, 1992) would yield similar results as when T-OW79 is used (in T-Ryan) (Fig. 6.8).

- Using T-BK2px_P-BK90, the palaeogeothermal gradient of the two localities studied is consistent with a 43mW/m^2 conductive geotherm without an inflected high temperature portion. Inflected geotherms produced by T-FB87_P-MG74 and T-BM86_P-NG85 are possibly due to errors in P-MG74 and P-NG85 at high temperatures. T-OW79_P-MG74 does not produce an inflected geotherm (Fig. 7.2c) because T-OW79 underestimates temperatures (section 6.2) thereby cancelling out the error in P-MG74.
- Although defined by only five samples, the 'garnet geotherm' is consistent with a geotherm that has a heat flow of between 40 to 43mW/m^2, similarly to the xenolith derived geotherms. Ryan *et al.* (1996) noted that, although subjective, the 'garnet geotherm' produces geotherms comparable to the xenolith-derived ones to within ~1-2 mW/m^2 for most localities they looked at.

REFERENCES

AI, Y. (1992). *Major and minor element systematics in the lherzolite system: a petrological and experimental study* Ph.D. thesis (unpubl.), Univ. Tasmania.

AI, Y. (1994). A revision of the garnet-clinopyroxene Fe^{2+}- Mg exchange geothermometer. *Contrib. Mineral. Petrol.*, **115**, 467-473.

AKELLA, J. (1976). Garnet-pyroxene equilibria in the system $CaSiO_3$-Al_2O_3 and in a natural mineral mixture. *Amer. Mineral.*, **61**, 589-598.

AKELLA, J. and Boyd, F.R. (1974). Petrogenetic grid for garnet peridotites *Carnegie Inst. Washing Yrbk.*, **73**, 269-273.

ARANOVICH, L.Y. and Pattison, D.R.M. (1995). Reassessment of the garnet-clinopyroxene Fe-Mg exchange thermometer: I. Evaluation of the Pattison and Newton (1989) experiments. *Contrib. Mineral. Petrol.*, **119**, 16-29.

BEATTIE, P. (1993). On the occurrence of apparent non-Henry's Law behaviour in experimental partitioning studies. *Geochim. Cosmochim. Acta*, **57**, 47-55.

BELL, D.R. and Rossman, G.R. (1992a). The distribution of hydroxyl in garnets from the subcontinental mantle of southern Africa. *Contrib. Mineral. Petrol.*, **111**, 161-178.

BELL, D.R. and Rossman, G.R. (1992b). Water in earth's mantle: the role of nominally anhydrous minerals. *Science*, **255**, 1391-1397.

BERMAN, R.G., Ya Aranovich, L. and Pattison, D.R.M. (1995). Reassessment of the garnet-clinopyroxene Fe-Mg exchange thermometer: II. Thermodynamic analysis. *Contrib. Mineral. Petrol.*, **119**, 30-42.

BERTRAND, P. and Mercier, J-C.C. (1985). The mutual solubility of coexisting ortho- and clinopyroxene: toward an absolute geothermometer for the natural system? *Earth Planet. Sci. Letters*, **76**, 109-122.

BERTRAND, P., Sotin, C., Mercier, J-C.C., and Takahashi, E. (1986). From the simplest chemical system to the natural one: garnet peridotite barometry. *Contrib. Mineral. Petrol.*, **93**, 168-178.

BICKLE, M.J. (1990). Mantle Evolution. *In*: Hall R.P. and Hughes D.J. (Eds.), *Early Precambrian Basic Magmatism.* Blackie, New York, 111-135.

BOYD, F.R. (1973). A pyroxene geotherm. *Geochim. Cosmochim. Acta*, **37**, 2533-2546.

BOYD, F.R. (1974). Ultramafic nodules from the Frank Smith kimberlite pipe, South Africa. *Carnegie Inst. Washing. Yrbk.*, **73**, 282-285.

BOYD, F.R. and Gurney, J.J. (1986). Diamonds and the African lithosphere. *Science*,

232, 2533-2546.

BOYD, F.R. and Nixon, P.H. (1973). Structure of the upper mantle beneath Lesotho. *Carnegie Inst. Wash. Yrbk.*, **72**, 431-445.

BOYD, F.R. and Nixon, P.H. (1975). Origins of ultramafic nodules from some kimberlites of northern Lesotho and the Monastery mine, South Africa. *Phys. Chem. Earth*, **9**, 431-454.

BOYD, F.R., Gurney, J.J. and Richardson, S.H. (1986). Evidence for a 150-200 km thick Archaean lithosphere from diamond inclusion geothermobarometry. *Nature*, **315**, 387-389.

BREY, G.P. (1989). *Geothermobarometry for lherzolite: experiments from 10 to 60 kb, new thermobarometers and application to natural rocks.* Habilitations Thesis, Technische Hochschule Darmstadt, p. 303.

BREY, G.P. (1991). Fictive conductive geotherms beneath the Kaapvaal craton: Extended abstracts, Fifth International Kimberlite Conference, Araxá, Brazil. *CPRM Special Publication* **2/91**, 23-25.

BREY, G.P. and Huth, J. (1984). The enstatite-diopside solvus to 60 kbar. *Proc. 3rd Int. Kimberlite Conf.*, **2**, 257-264.

BREY, G.P., and Köhler T. (1990). Geothermobarometry in four-phase lherzolites II: New thermobarometers, and practical assessment of existing thermobarometers. *J. Petrol.*, **31**, 1353-1378.

BREY, G.P., Köhler, T. and Nickel, K.G. (1990). Geothermobarometry of four-phase lherzolites I: Experimental results from 10 to 60 kb. *J. Petrol.*, **31**, 1313-1352.

BREY, G.P., Nickel, K.G. and Kogarko, L. (1986). Garnet-pyroxene equilibria in the system CaO-MgO-Al_2O_3-SiO_2 (CMAS): prospects simplified ('T-independent') lherzolite barometry. *Contrib. Mineral. Petrol.*, **92**, 448-455.

CAMPBELL, J.L., Teesdale, W.J. and Halden, N.M. (1995). Theory, practice and application of micro-PIXE analysis and element-distribution maps. *Can. Mineral.*, **33**, 279-292.

CAMPBELL, J.L., Teesdale, W.J., Kjarsgaard, B.A. and Cabri, L.J. (1996). Micro-PIXE analysis of silicate reference standards for trace Ni, Cu, Zn, Ga, Ge, As, Rb, Sr, Y, Zr, Nb, Mo and Pb, with emphasis on Ni for application of the Ni-in-garnet geothermometer. *Can. Mineral.*, **34**, 37-48.

CANIL, D. (1994). An experimental calibration of the "nickel in garnet" geothermometer with applications. *Contrib. Mineral. Petrol.*, **117**, 410-420.

CANIL, D. (1996). An experimental calibration of the nickel in garnet geothermometer with applications: reply. *Contrib. Mineral. Petrol.*, **124**, 219-223.

CANIL, D. and O'Neill, H. St. C. (1996). Distribution of Ferric Iron in some Upper-Mantle Assemblages. *J. Petrol.*, **37**, 607- 635.

CARSWELL, D.A. (1975). Primary and secondary phlogopites and clinopyroxenes in garnet lherzolite xenoliths. *Phys. Chem. Earth*, **9**, 417-429.

CARSWELL, D.A. (1991). The garnet-orthopyroxene Al barometer: problematic application to natural garnet lherzolite assemblages. *Min. Mag.*, **55**, 19-31.

CARSWELL, D.A. and Gibb, F.G.F. (1980). Geothermometry of garnet lherzolite nodules with special reference to those from the kimberlite of northern Lesotho. *Contrib. Mineral. Petrol.*, **74**, 403-416.

CARSWELL, D.A., and Gibb, F.G.F. (1987). Evaluation of mineral thermometers and barometers applicable to garnet lherzolite assemblages. *Contrib. Mineral. Petrol.*, **95**, 499-511.

COX, K.G., Gurney, J.J. and Harte, B. (1973). Xenoliths from the Matsoku pipe. *In*: Nixon P.H., *Lesotho Kimberlites*. Lesotho Nat. Dev. Corp., Maseru, 76-100.

DANCHIN, R.V. and Boyd, F.R. (1976). Ultramafic nodules from the Premier Kimberlite Pipe, South Africa. *Carnegie Inst. Wash. Yrbk.*, **75**, 531-538.

DAVIDSON, P.M. and Lindsley, D.H. (1985). Thermodynamic analysis of quadrilateral pyroxenes. Part II: Model calibration from experiments and applications to geothermometry. *Contrib. Mineral. Petrol.*, **91**, 390-404.

DAVIS, B.T.C. and Boyd, F.R. (1966). The join $Mg_2Si_2O_6$-$CaMgSi_2O_6$ at 30 kb pressure and its application to pyroxenes from kimberlite. *J. Geophys. Res.*, **71**, 3567-3576.

DAWSON, J.B. and Stephens, W.E. (1975). Statistical classification of garnets from kimberlites and associated xenoliths. *J. Geology.*, **83**, 589-607.

EGGLER, D.H. and Wendlandt, R.F. (1979). Experimental studies on the relationship between kimberlite magmas and partial melting of peridotites. *In*: Boyd, F.R. and Meyer, H.O.A. (Eds.), *Kimberlites, diatremes and diamonds; their geology, petrology and chemistry.* (Proc. Int. Kimberlite Conf., No. 2, Vol 1), Washington D.C., American Geophysical Union, 330-338.

EHRENBERG, S.N. (1979). Garnetiferious ultramafic inclusions in minette from the Navajo Volcanic Field: *In*: Boyd, F.R., and Meyer, H.O.A., (Eds.), *The mantle sample: inclusions in kimberlites and other volcanics.* (Proc. Int. Kimberlite Conf., No. 2, Vol 2), Washington DC, American Geophysical Union, 330-334.

ELLIS, D.J. and Green, D.H. (1979). An experimental study of the effect of Ca upon garnet-clinopyroxene Fe-Mg exchange equilibria. *Contrib. Min. Petrol.*, **71**, 13-22.

FEDOROWICH, J.S., Jain, J.C., Kerrich, R. and Sopuck, V. (1995). Trace element analysis of garnet by laser-ablation microprobe ICP-MS. *Can. Mineral.*, **33**, 469-480.

FERRY, J.M. and Spear, F.S. (1978). Experimental calibration of the partitioning of Fe and Mg between biotite and garnet. *Contrib. Mineral. Petrol.*, **66**, 113-117.

FIELD, S.W., Haggerty, S.E. and Erlank, A.J. (1989). Subcontinental metasomatism in the region of Jagersfontein, South Africa. *In*: Kimberlites and Related Rocks, Volume 2: The mantle/crust setting, diamonds and diamond exploration. *Geological Society of Australia Special Publication*, **14**, 771-783.

FINNERTY, A.A. (1989). Inflected mantle geotherms from xenoliths are real: Evidence from olivine barometry. *In*: Kimberlites and Related Rocks, Volume 2: The mantle/crust setting, diamonds and diamond exploration *Geological Society of Australia Special Publication*, **14**, 883-900.

FINNERTY, A.A. and Boyd F.R. (1984). Evaluation of thermobarometers for garnet peridotites. *Geochim. Cosmochim. Acta*, **48**, 15-27.

FINNERTY, A.A. and Boyd, F.R. (1987). Thermobarometry for garnet peridotites: basis for the determination of thermal and compositional structure of the upper mantle. *In*: Nixon, P.H. (Ed.), *Mantle Xenoliths*. John Wiley and Sons Ltd., Great Britain, 381-402.

FRASER, D.G. and Lawless, P.J. (1978). Palaeogeotherms: implications of disequilibrium in garnet lherzolite xenoliths. *Nature*, **273**, 220-221.

GANGULY, J. and Bhattacharya, P.K. (1987). Xenoliths in Proterozoic kimberlites from southern India: petrology and geophysical implications. *In*: Nixon P.H. (Ed.), *Mantle Xenoliths*. John Wiley and Son Ltd, Great Britain, pp. 249-265.

GASPARIK, T. (1987). Orthopyroxene thermobarometry in simple and complex systems. *Contrib. Mineral. Petrol.*, **96**, 357-370.

GASPARIK, T. and Newton, R.C. (1984). The reversed Al-contents of orthopyroxene in equilibrium with spinel and forsterite in the system $MgO-Al_2O_3-SiO_2$. *Contrib. Mineral. Petrol.*, **85**, 186-196.

GREEN, H.W. and Guegen, Y. (1974). Origin of kimberlite pipes by diapiric upwelling in the upper mantle. *Nature*, **249**, 617-619.

GRIFFIN, W.L. and Ryan, C.G. (1995). Trace element in indicator minerals: area selection and target evaluation in diamond explration. *J. Geochem. Explor.*, **53**, 311-337.

GRIFFIN, W.L. and Ryan, C.G. (1996). An experimental calibration of the "nickel in garnet" geothermometer with applications, by D. Canil: discussion. *Contrib. Mineral. Petrol.*, **124**, 216-218.

GRIFFIN, W.L., Cousens, D.R., Sie, S.H. and Suter, G.F. (1989a). Ni in chrome garnet: a new geothermometer. *Contrib. Mineral. Petrol.*, **103**, 199-202.

GRIFFIN, W.L., Smith, D., Boyd, F.R., Cousens, D.R., Ryan, C.G., Sie, S.H. and Suter, G.F. (1989b). Trace-element zoning in garnets from sheared mantle xenoliths. *Geochim. Cosmochim. Acta*, **53**, 561-567.

GRIFFIN, W.L., Gurney, J.J. and Ryan, C.G. (1992). Variations in trapping temperatures and trace elements in peridotite-suite inclusions from African diamonds: evidence for two inclusion suites, and implications for lithosphere stratigraphy. *Contrib. Mineral. Petrol.*, **110**, 1-15.

GRIFFIN, W.L., Ryan, C.G. and Win T.T. (1995). Mapping the earth's mantle in 4D using the proton microprobe. *Nuclear Instrument and Methods in Physics Research*, **B104**, 456-463.

GURNEY, J.J. and Moore, R.O. (1991). Geochemical correlations between kimberlitic indicator minerals and diamonds on the Kalahari craton. *Geol. Geofisika*

GURNEY, J.J. and Switzer, G.S. (1973). The discovery of garnets closely related to diamond in the Finsch pipe, South Africa. *Contrib. Mineral. Petrol.*, **39**, 103-116.

GURNEY, J.J. and Zweistra, P. (1995). The interpretation of the major element compositions of mantle minerals in diamond exploration. *J. Geochem. Explor.*, **53**, 293-309.

GURNEY, J.J., Harte, B. and Cox, K.G. (1957). Mantle xenoliths in the Matsoku kimberlite pipe. *Phys. Chem. Earth*, **9**, 507-523.

HARLEY, S.L. (1984). Comparison of the garnet-orthopyroxene geothermobarometer with recent experimental studies and applications to natural assemblages. *J. Petrol.*, **25**, 697-712.

HARTE, B. (1977). Rock nomenclature with particular relation to deformation and recrystallisation textures in olivine-bearing xenoliths. *J. Geol.*, **85**, 279-288.

HARTE, B. and Gurney, J.J. (1975). Ore mineral and phlogopite mineralisation within ultramafic xenoliths from the Matsoku kimberlite pipe, Lesotho. *Carnegie Inst. Wash. Yrbk.*, **74**, 528-536.

HARTE, B. and Gurney, J.J. (1982). Compositional and textural features of peridotite nodules from the Jagersfontein kimberlite pipe, South Africa. *Terra Cognita*, **2**, 256-257.

HARTE, B., Cox, K.G. and Gurney, J.J. (1975). Petrography and geological history of upper mantle nodules from the Matsoku kimberlite pipe. *Phys. Chem. Earth*, **9**, 477-506.

HARTE, B., Winterburn, P.A. and Gurney, J.J. (1987). Metasomatic and enrichment phenomena in garnet peridotite facies nodules from the Matsoku kimberlite pipe, Lesotho. *In*: Menzies, M.A. and Hawkesworth, C.J. (Eds.), *Mantle Metasomatism.* Academic press, London, 145-220.

HATTON, C.J. (1978). *The geochemistry and the origin of the xenoliths from the Roberts Victor mine.* Ph.D. thesis (unpubl.), University of Cape Town.

HELMSTAEDT, H. H. and Gurney, J.J. (1995). Geotectonic controls of primary diamond deposits: implications for area selection. *In*: Griffin, W.L. (Ed.), Diamond Exploration: Into the 21st Century. *J. Geochem. Explor.*, 125-144.

HENSON, B.J. (1973). Pyroxenes and garnets as geothermometers and geobarometers. *Carnegie Inst. Wash. Yrbk.*, **72**, 527-534.

HOPS, J.J. (1989). *Some aspects of the geochemistry of the high temperature and megacrysts from the Jagersfontein kimberlite pipe, S.A.* Ph.D. thesis (unpubl.), University of Cape Town.

IONOV, D.A., Ashchepkov, I.V., Stoch, H.-G., Witt-Eickschen, G. and Seck, H.A. (1993). Garnet peridotite xenoliths from the Vitim Volcanic Field, Baikal Region: the nature of the garnet-spinel peridotite transition zone in the continental mantle. *J. Petrol.*, **34**, 1141-1175.

IRVING, A.J. (1976). On the validity of paleogeotherms determined from xenolith suites in basalts and kimberlites. *Amer. Mineral.*, **61**, 638-642.

LINDSLEY, D.H. and Dixon, S.A. (1976). Diopside-enstatite equilibria at 850-1400^{0}C, 5-35 kb. *Amer. J. Sci.*, **276**, 1285-1301.

LUTH, R.W. and Canil, D. (1993). Ferric iron in mantle-derived pyroxenes and a new oxybarometer for the upper mantle. *Mineralogy and Petrology*, **99**, 44-48.

LUTH, R.W., Virgo, D., Boyd, F.R. and Wood, B.J. (1990). Ferric iron in mantle derived garnets: implications for thermobarometry and for the oxidation state of the mantle. *Contrib. Mineral. Petrol.*, **104**, 56-72.

KAWASAKI, T. and Matsui, Y. (1983). Thermodynamic analyses of equilibria involving olivine, orthopyroxene and garnet. *Geochim. Cosmochim. Acta*, **47**, 1661-1179.

KENNEDY, C.S. and Kennedy, G.C. (1976). The equilibrium boundary between graphite and diamond. *J. Geophys. Res.*, **81**, 2467-2470.

KÖHLER, T.P. and Brey, G.P. (1990). Calcium exchange between olivine and clinopyroxene calibrated as a geothermobarometer for natural peridotites from 2 to 60kb with applications. *Geochim. Cosmochim. Acta*, **54**, 2375-2388.

KRAMERS, J.D. and Smith, C.B. (1983). A feasebility study of U-Pb and Pb-Pb dating using groundmass mineral fractions and whole rock samples. *Isotope Geoscience*, **1**, 23-35.

KROGH, E.J. (1988). The garnet-clinopyroxene Fe-Mg geothermometer – a reinterpretation of existing experimental data. *Contr. Mineral. Petrol.*, **99**, 44-48.

KJARSGAARD, B.A., 1992. Is Ni in chrome pyrope garnet a valid diamond exploration tool? *Geol. Surv. Can., Paper* **92-1E**, 315-322.

MATSUI, Y., Syono, Y., Akimoto, S. and Kitayama, K. (1968). Unit cell dimensions of some synthetic orthopyroxene group solid solutions. *J. Geochem.*, **2**, 61-70.

MAXWELL, J.A., Campbell, S.L. and Teesdale, W.J. (1989). The Guelph PIXE software package. *Nucl. Instr. Meth. Phys. Res.*, **B43**, 218-230.

MERCIER, J-C. and Carter, N. (1975). Pyroxene geotherms. *J. Geophys. Res.*, **80**, 3349-3362.

McGUIRE, A.V., Dyar, M.D. and Ward, K.A. (1989). Neglected Fe^{2+}/Fe^{3+} ratios: a study of the Fe^{3+} content of megacrysts from alkali basalts. *Geology*, **17**, 687-690.

McGUIRE, A.V., Dyar, M.D. and Nielson, J.E. (1991). Metasomatic oxidation of upper mantle peridotite. *Contrib. Mineral. Petrol.*, **109**, 252-264.

McGREGOR, I.D. (1974). The system $MgO-Al_2O_3-SiO_2$: solubility of Al_2O_3 in enstatite for spinel and garnet peridotite compositions. *Amer. Mineral.*, **59**, 110-119.

MITCHELL, R.H. (1978). Garnet lherzolites from Somerset Island, Canada and aspects of nature of perturbed geotherms. *Contrib. Mineral. Petrol.*, **72**, 205-217.

MITCHELL, R.H. (1984). Garnet lherzolites from the Hanaus-I and Louwrensia kimberlites of Namibia. *Contrib. Mineral. Petrol.*, **86**, 178-188.

MITCHELL, R.H. (1986). *Kimberlites.* Plenum Press, New York, 422pp.

MITCHELL, R.H., Carswell D.A., and Clarke D.B. (1980). Geological implications and validity of calculated equilibration conditions for ultramafic xenoliths from the Pipe 200 kimberlite, Northern Lesotho. *Contrib. Mineral. Petrol.*, **119**, 16-29.

MORGAN, P. (1995). Diamond exploration from the bottom up: regional geophysical signatures of lithosphere conditions favorable for diamond exploration. *In*: Griffin, W.L. (Ed.), Diamond Exploration: Into the 21st Century. *J. Geochem. Explor.*, **53**, 145-165.

MORI, T. and Green, D.H. (1975). Pyroxenes in the system $Mg_2Si_2O_6$ - $CaMgSi_2O_6$ at high pressure. *Earth Planet. Sci. Letters*, **26**, 277-286

MORI, T., and Green, D.H. (1978). Laboratory duplication of phase equilibria observed in natural garnet lherzolites. *J. Geol.*, **86**, 83-97.

NICKEL, K.G. (1989). Garnet-pyroxene equilibria in the system SMACCr (SiO_2-MgO-Al_2O_3-CaO-Cr_2O_3): The Cr-geobarometer. *Spec. Publ. Geol. Soc. Aust.*, **14**, 901-912.

NICKEL, K.G. and Brey, G..P.(1984). Subsolidus orthopyroxene-clinopyroxene systematics in the system $CaO-MgO-SiO_2$ to 60 kb: a re-evaluation of the regular solution model. *Contrib. Mineral. Petrol.*, **87**, 35-42.

NICKEL, K.G. and Green, D.H. (1985). Empirical geothermobarometry for garnet peridotites and implications for the nature of the lithosphere, kimberlites and diamonds. *Earth Planet. Sci. Letters*, **73**, 158-170.

NICKEL, K.G., Brey G.P., and Kogarko, L. (1985). Orthopyroxene-clinopyroxene equilibria in the system $CaO-MgO-Al_2O_3-SiO_2$ (CMAS): new experimental results and implications for two-pyroxene thermometry. *Contrib. Mineral. Petrol.*, **81**, 44-53.

NIXON, P.H. and Boyd, F.R. (1973). Petrogenesis of the granular and sheared ultrabasic nodule suite in kimberlites. *In*: Nixon, P.H. (Ed.), *Lesotho Kimberlites*. Lesotho National Development Corporation, 48-56.

NORMAN, M.D., Pearson, N.J., Sharma, A. and Griffin, N.L. (1996). Quantitative analysis of trace elements in geological materials by laser ablation ICP-MS: Instrumental operating conditions and calibration values of NIST glasses. *Geostandard Newsletter*, **20**, 247-261.

O'NEILL, H. St-C. (1980) An experimental study of Fe-Mg partitioning between garnet and olivine and its calibration as a geothermometer: corrections. *Contrib. Mineral. Petrol.*, **72**, 337.

O'NEILL, H. St-C. and Wood, B.J. (1979). An experimental study of Fe-Mg partitioning between garnet and olivine and its calibration as a geothermometer. *Contrib. Mineral. Petrol.*, **70**, 59-70.

PATTISON, D.R.M. and Newton, R.C. (1989). Reversed experimental calibration of the garnet-clinopyroxene Fe-Mg exchange thermometer. *Contrib. Mineral. Petrol.*, **101**, 87-103.

PEARSON, D.G., Boyd, F.R., Haggerty, S.E., Pasteris, J.D., Field, S.W., Nixon, P.H. and Pokhilenko, N.P. (1994). The characterisation and origin of graphite in cratonic lithospheric mantle: a petrological carbon isotope and Raman spectroscopic study. *Contrib. Mineral. Petrol.*, **115**, 449-466.

PERKINS III, D. and Newton, R.C. (1980). The composition of coexisting pyroxenes and garnet in the system $CaO-MgO-Al_2O_3-SiO_2$ at $900-1100^0C$ and high pressures. *Contrib. Mineral. Petrol.*, **75**, 291-300.

POUCHOU, J.L. and Pichoir, F. (1984). A new model for quantitative X-ray microanalysis, Part 1: Application to the analysis of homegeneous samples. *La Rech. Aérosp.*, **5**, 13-38.

POLLACK , H.N., and Chapman, D.S. (1977). On the regional variation of heat flow, geotherms and lithospheric thickness. *Tectonophysics*, **38**, 279-296.

POWELL, R. (1985). Regression diagnostics and robust regression in geothermometer/ geobarometer calibrations: the garnet-clinopyroxene geothermometer revisited. *J. Metam. Geol.*, **3**, 231-243.

PROZESKY, V.M., Przybylowicz, W.J., van Achterbergh, E., Churms, C.L., Pineda, C.A., Springhorn, K.A., Pilcher, J.V., Ryan, C.G., Kritzinger, J., Schmitt, H. and Swart, T. (1995). The NAC nuclear microprobe facility. *Nucl. Instr. Meth. Phys. Res.*, **B 104**, 36-42.

RÅHEIM, A. and Green, D.H. (1974). Experimental determination of the temperature and pressure dependence of the Fe-Mg partition coefficient for coexisting clinopyroxene and garnet. *Contrib. Mineral. Petrol.*, **48**, 179-203.

RICHARDSON, S.H., Gurney, J.J., Erlank, A.J. and Harris, J.W. (1984). Origin of diamonds in old enriched mantle. *Nature*, **310**, 198-202.

RUDNICK, R.L., McDonough, W.F. and O'Connell R.J. (1998). Thermal structure, thickness and composition of continental lithosphere. *Chem. Geol.*, **145**, 395-411.

RUTSTEIN, M.S. and Yund, R.A. (1969). Unit-cell parameters of synthetic diopside-hedenbergite solid solutions. *Amer. Mineral.*, **54**, 238-245.

RYAN, C.G. and Jamieson, D.N. (1993). Dynamic analysis: On-line quantitative PIXE micro-analysis and its use in overlap-resolved elemental mapping. *Nucl. Instr. and Meth. Phys. Res.*, **B77**, 203-214.

RYAN, C.G., Cousens, D.R., Sie, S.H., Griffin, W.L., Suter, G.F. and Clayton, E. (1990). Quantitative PIXE microanalysis of geological material using the CSIRO proton microprobe. *Nucl. Instr. Meth. Phys. Res.*, **B47**, 55-71.

RYAN, C.G., Griffin, W.L. and Pearson, N.J. (1996). Garnet geotherms: Pressure-temperature data from Cr-pyrope garnet xenocrysts in volcanic rocks. *J. Geophys. Res.*, **101**, 5611-5625.

SAXENA, S.K. and Nehru, C.E. (1975). Enstatite-diopside solvus geothermometry. *Contrib. Mineral. Petrol.*, **49**, 259-267.

SHIMIEU, N. (1997). Principles of SIMS and modern ion microprobes. *In*: Gill, R. (Ed.), *Modern analytical geochemistry: an introduction to quantitative chemical analysis for earth, environmental and materials scientists.* Longman, Harlow, England, 329pp.

SMITH, C.B. (1983). Pb, Sr and Nd isotopic evidence for sources of southern African Cretaceous kimberlites. *Nature*, **304**, 51-54.

SMITH, C.B., Allosop, H.L., Kramers, J.D., Hutchinson, G. and Roddick, J.C. (1985a). Emplacement ages of Jurassic-Cretaceous South African kimberlites by the Rb-Sr method on phlogopite and whole-rock samples. *Transactions of the Geological Society of South Africa*, **88**, 267-280.

SMITH, D. (in prep.) Temperatures and pressures of mineral equilibration in peridotite xenoliths: Review, discussion, and implications.

SMITH, D. and Boyd, F.R. (1987). Compositional heterogeneities in a high temperature nodule and implications for mantle processes. *In*: Nixon, P.H. (Ed.), *Mantle Xenoliths*. John Wiley and Sons, New York, 551-561.

SKOGBY, H. and Rossman, G.R.(1989). OH^- in pyroxene: an experimental study of incorporation mechanisms and stability. *Amer. Mineral.*, **74**, 1059-1069.

TAKAHASHI, T. and Liu, L.G. (1970). Compression of ferromagnesian garnets and the effect of solid solutions on the bulk shear modulus. *J. Geophys. Res.*, **71**, 5757-5766.

TURNOCK, A.C., Lindsley, D.H. and Grover, J.E. (1973). Synthesis and unit cell parameters of Ca-Mg-Fe pyroxenes. *Amer. Mineral.*, **58**, 50-59.

VAN ACHTERBERGH, E. (1994). *The development of the National Accelerator Centre - proton microprobe as an analytical tool in geochemistry.* M.Sc thesis (unpubl.), University of Cape Town.

VAN ACHTERBERGH, E., Ryan, C.G., Gurney, J.J. and le Roex, A.P. (1995). PIXE profiling, imaging and analysis using the NAC proton microprobe: Unravelling mantle eclogites. *Nucl. Instr. Meth. Phys. Res.*, **B77**, 203-214.

VIRGO, D., Luth, R.W., Moats, M.A. and Ulmer, G.C. (1988). Constraints on the oxidation state of the mantle: an electrochemical and ^{57}Fe Mössbauer study of mantle-derived ilmenites. *Geochim. Cosmochim. Acta*, **52**, 1781-1794.

WELLS, P.R.A. (1977). Pyroxene thermometry in simple and complex systems. *Contrib Mineral. Petrol.*, **62**, 129-139.

WINTERBURN, P.A. (1987). *Geochemical studies of peridotite xenoliths from southern African kimberlites.* Ph.D. thesis (unpubl.), University of Edinburgh.

WINTERBURN, P.A. and Harte, B. (1987). Metasomatism in coarse peridotite nodules from the Jagersfontein kimberlite pipe. *Terra Cognita*, **7**, 395-396.

WILSON, M.A. (1972). *International Diamonds Number 2.* Diamond Annual (Pty) Ltd., South Africa, p. 35.

WOOD, B.J. and Banno, S. (1973). Garnet-orthopyroxene and orthopyroxene-clinopyroxene relationships in simple and complex systems. *Contrib. Mineral. Petrol.*, **42**, 109-124.

WOOD, B.J. and Fraser, D.G. (1977). *Elementary thermodynamics for geologists.* Oxford University Press, Great Britain, p. 303.

YANG, A. (1994). A revision of the garnet-clinopyroxene Fe^{2+}-Mg exchange geothermometer. *Contrib. Mineral. Petrol.*, **115**, 467-473.

Appendix A

Petrography

Brief petrographic descriptions of each sample are given. Cox et al. (1973), Winterburn (1987) and Hops (1989) have described most of these samples in detail. The textural classification used is that of Harte (1977). Samples are classified as lherzolites on the presence of clinopyroxene even if clinopyroxene modal abundances are less than 5%. Similar samples are described as a unit. opx = orthopyroxene, cpx = clinopyroxene; percentages in brackets are modal percentages.

Jagersfontein Xenoliths

J 117

Garnet lherzolite with a coarse texture

Olivine (65%) dominates the mineralogy and has serpentinised fractures and grain edges. Garnet (15%) has two concentric kelyphite rims: the inner rim is dark brown and microscopically unidentifiable. The slightly more coarse-grained outer rim is composed of phlogopite and spinel. Opx (10%) and olivine show undulose extinction. Cpx (10%) has 'spongy' grain edges.

JJG 1710

Garnet lherzolite with a fluidal mosaic-porphyroclastic texture

The mineralogy is dominated by olivine neoblasts (65%) with serpentinised grain boundaries. Opx (20%) is serpentinised along fractures and is recrystallised to neoblasts along grain edges. Garnet (15%) is up to 5 mm in longest dimension with dark brown kelyphite rims occasionally with a thin phlogopite outer rim. Cpx occurs in trace amounts as anhedral grains with 'spongy' grain edges.

JJG1716

Amphibole-bearing garnet harzburgite with a coarse texture

Olivine (45%) is up to 6 mm in size and has fractures filled with serpentine. Opx (35%) has grain sizes that are up to 8 mm in longest dimension, with serpentine veins cutting across the grains. Garnet (10%) has light brown kelyphite rims and forms a broken 'necklace' texture. Amphibole (10%) partially and sometimes completely encloses garnets. Spinel occurs as anhedral grains in trace amounts. The sample has straight 120^{0} triple point grain boundaries.

JJG 1728

Garnet lherzolite with a coarse texture

Olivine (50%) and opx (30%) dominate the mineralogy. Most grain boundaries are filled with serpentine and phlogopite. Olivine is up to 4mm and has fractures filled with serpentine. Opx is anhedral and up to 3 mm in longest dimension. Garnet (10%) is up to 1 mm and has a thin dark brown kelyphite rim surrounded by thin phlogopite outer rims. Cpx (10%) occurs as anhedral grains. Spinel occurs as anhedral grains in trace amounts. The sample has straight 120^{0} triple point grain boundaries.

JJG 1729

Garnet lherzolite with a mosaic-porphyroclastic texture

Olivine (60%) dominates, occurring mostly as neoblasts. Extensive serpentinisation occurs within fractures and grain boundaries of the olivines. Opx porphyroclasts (10%) have been recrystallised to neoblasts at grain edges. Opx and olivine porphyroclasts show undulose extinction. Garnet (20%) has very thick kelyphite rims with some of the garnets completely replaced by kelyphite. Cpx (10%) occurs as anhedral grains with 'spongy grain edges.

JJG 1733

Coarse lherzolite with a coarse texture

The mineralogy is dominated by intensely serpentinised olivine (60%). The more prominent veins in grain boundaries contain phlogopite and oxides. Opx (25%) is highly altered and serpentinised along grain edges. Some of the opx is completely serpentinised. Garnet (15%) occurs between olivine and opx forming a poorly formed 'necklace' texture. The garnet seems to have formed by a reaction between olivine and opx. Spinel occurs as anhedral grains in trace amounts. Cpx occurs as a trace mineral.

JJG 1757

Garnet harzburgite with a coarse texture

Olivine (80%), with a size of up to 8 mm longest dimension, dominates the mineralogy of this sample. The olivine is intensely fractured, with the fractures filled with serpentine and phlogopite. Garnet (15%) is purple in colour, up to 8 mm longest dimension and has dark brown kelyphite rims surrounded by phlogopite-spinel outer rims. Opx (5%) occurs as a minor mineral. The sample has straight 120^0 triple point grain boundaries. Spinel occurs as anhedral grains in trace amounts.

JJG 1761

Garnet harzburgite with a coarse texture

The mineralogy is dominantly olivine (80%). The olivine is up to 10 mm in longest dimension and is intensely fractured with fractures showing intense serpentinisation. Occasionally phlogopite occurs in olivine fractures. Garnet (15%) is up to 5 mm longest dimension and purple in colour with a dark brown kelyphite rim surrounded by a phlogopite-spinel outer rim. Opx (5%) occurs as a minor mineral. Spinel occurs in trace amounts. The sample has straight 120^0 triple point grain boundaries.

JJG 864

Garnet lherzolite with a coarse texture

Olivine (40%) in this sample is highly fractured and serpentinised. Opx (52%) has olivine inclusions and is serpentinised at grain edges. Garnet (5%) has two concentric rims and has a size range of 2 to 6 mm in longest dimension. Cpx (3%) occurs as anhedral grains and shows no signs of internal strain. Spinel occurs in trace amounts. The sample has straight 120^0 triple point grain boundaries.

JJH 1, JJH28, JJH35

Garnet harzburgite with a porphyroclastic texture

Olivine (50%) dominates, mostly occurring as neoblasts. Opx (30%) occurs as elongated porphyroclasts with neoblasts at grain edges. Olivine and opx show undulose extinction. Garnets (20%) are up to 3 mm in longest dimension with two concentric kelyphite rims as in J117. In JJH1, the smaller garnets (1 to 2 mm) are completely replaced by kelyphite.

JJH 10

Garnet lherzolite with a mosaic porphyroclastic texture

Olivine (70%) dominates the mineralogy, occurring mainly as neoblasts. Opx (10%) occurs mainly as porphyroclasts, but some grains are recrystallised to neoblasts along grain boundaries and along major fractures. Some opx grains are almost completely recrystallised. Garnet (12%) is up to 1 mm in longest dimension and has dark brown kelyphite rims. Cpx (8%) occurs as anhedral grains with 'spongy' grain edges.

JJH23

Garnet dunite with a mosaic porphyroclastic texture

Olivine (90%) dominates the mineralogy of this extensively serpentinised sample. Olivine occurs mostly as strain free olivine platelets and occasionally as deformed porphyroclasts showing undulose extinction. Opx (5%) is almost completely replaced by serpentine. Garnet (5%) occurs as 1 mm round grains with two kelyphite rims as in J117.

JJH29

Garnet harzburgite with a mosaic-porphyroclastic texture

Olivine (60%) dominates the mineralogy, occurring mostly as neoblasts. Opx (15%) is highly serpentinised and recrystallised to neoblasts. Some of the opx has been totally recrystallised to neoblasts. Olivine and opx porphyroclasts show undulose extinction. Garnet (15%) is intensely fractured and has thin dark brown kelyphite rims.

JJH 32

Garnet lherzolite with a mosaic-porphyroclastic texture

Olivine (70%) dominates the mineralogy, occurring mostly as neoblasts. Opx (20%) occurs mostly as porphyroclasts but was occasionally recrystallised to neoblasts along grain boundaries and major fractures. Garnets (10%) show less fracturing and have dark brown kelyphite rims. Cpx occurs in trace amounts as anhedral grains with 'spongy' grain edges.

JJH 6

Garnet harzburgite with a fluidal mosaic-porphyroclastic texture

Olivine neoblasts (60%) dominate. Olivine porphyroclasts occur as thin lenticles. Opx (25%) occurs as elongate porphyroclasts joined by thin lenticles of opx neoblasts. Garnet (15%) has thick dark brown kelyphite rims.

JJH7, JJH8

Garnet lherzolite with a mosaic-porphyroclastic texture

Olivine (50%) is completely recrystallised to neoblasts. Opx (30%) occurs as fractured and serpentinised porphyroclasts, recrystallised to neoblasts at grain edges and shows undulose extinction. Some of the opx occurs as thin lenticles, completely recrystallised to neoblasts. Garnets (20%) have two concentric kelyphite rims as in J117. Some of the garnets are completely replaced by kelyphite. Cpx occurs in trace amounts as anhedral grains with 'spongy' grain edges.

JJH9

Garnet harzburgite with a porphyroclastic texture

Olivine (60%) dominates, occurring mostly as neoblasts, but also as elongate porphyroclasts. Opx (20%) occurs as elongate porphyroclasts joined by thin lenticles of opx neoblasts. The opx porphyroclasts show undulose extinction. Garnet (20%) has two concentric kelyphite rims as in J117. Some of the garnets are completely replaced by kelyphite.

Matsoku Xenoliths

LBM 10

Garnet lherzolite with a coarse texture

Olivine (60%) dominates the mineralogy and has intense fracturing filled with serpentine. Mostly, the olivine has straight grain boundaries with 120^0 triple points and a grain size of up to 5 mm. Opx (25%) occurs as anhedral grain with sizes of up to 3 mm. Cpx (10%) occurs as strain-free subhedral grains with an average grain size of 1 mm. Garnet (5%) has dark brown kelyphite rims.

LBM 16

Garnet lherzolite with a porphyroclastic texture

Olivine (55%) dominates the mineralogy, occurring mostly as porphyroclasts. Opx (30%) occurs as 1-2 mm anhedral laths. Garnet (10%) varies in size from less than 1 mm to 5 mm with dark brown kelyphite rims. In some places garnets occur as streaks of small altered round grains. Cpx (5%) occurs as anhedral grains with 'spongy' grain edges.

LBM 17

Garnet harzburgite with a coarse texture

The mineralogy is dominantly olivine (50%). The olivine has a grain size of up to 5 mm and substraight grain boundaries with occasional 120^0 triple points. Opx (40%) is extensively serpentinised in most cases. Garnet (10%) has a double rim as in J117.

LBM20

Garnet dunite with a coarse texture

Olivine (99%) dominates this essentially monomineralic rock. The olivine has substraight to irregular grain boundaries. Occasionally the grain boundaries form 120^0 triple points. Although this sample has an average coarse texture, olivine is occasionally recrystallised at grain edges. There is virtually no serpentinisation in this sample. Garnet (1%) occurs as small (0.5 mm) round grains with two kelyphite rims as in J117.

LBM22

Garnet harzburgite with a porphyroclastic texture

Olivine (50%) shows undulose extinction and mostly occurs as porphyroclasts, with the neoblasts forming at grain edges. Opx (40%) has grain sizes of up to 5 mm, shows minimum amount of strain and has inclusions of olivine. Garnet (10%) is drawn into streaks of rounded altered grains.

LBM 3

Garnet lherzolite with a coarse texture

Olivine (50%) dominates with a grain size of up to 5 mm and showing undulose extinction. Opx (45%) is up to 3 mm and sometimes has olivine (?) inclusions. Garnet (3%) has dark-brown kelyphite rims. Cpx (2%) occurs as anhedral grains in minor amounts.

LBM 30

Garnet lherzolite with porphyroclastic texture

Dominantly olivine (60%), occurring mostly as highly fractured olivine porphyroclasts showing undulose extinction. Fractures are filled with serpentine. Neoblasts are mainly restricted to grain boundaries and major fractures of the mainly 3 mm olivine porphyroclasts. Cpx (25%) is anhedral and up to 1 mm. Opx (10%), like olivine, shows undulose extinction. Garnet (5%) is normally less than 1 mm in size and mostly almost completely altered. Garnet kelyphite rims are dark brown and occasionally occur with phlogopite in association.

LBM 32

Garnet orthopyroxenite with a mosaic-porphyroclastic texture

Opx (30%) dominates with a size of up to 4 mm. Some of the opx grains have cpx (?) inclusions. Olivine (25%) occurs mostly as neoblasts. Garnet (25%) is highly altered along grain boundaries and fractures. Some of the garnet grains are almost completely replaced by kelyphite. Cpx (15%) mainly occurs with olivine neoblasts and is of the same size as the olivine (1-2 mm). Phlogopite (5%) appears to be associated with the alteration of garnet.

LBM 36

Banded garnet pyroxenite with a coarse texture

Two thin section were cut from the different units of this banded pyroxenite. The bands are distinguished by the relative modal proportions of the primary mineralogy: [*LBM36-3:- opx 40%, olivine 30%, garnet 15%, cpx 15%; LBM36-2:- olivine 40%, cpx 30%, opx 20%, garnet 10%*].

Olivine has irregular grain boundaries and show undulose extinction (indicating deformation). The olivine is occasionally recrystallised to neoblasts at grain boundaries. Opx has olivine inclusions and also shows undulose extinction. Cpx is up to 5 mm in size and has 'spongy' grain edges. Garnet is normally highly altered and up to 5 mm in size. Garnet has two concentric kelyphite rims as in J117.

LBM 6

Garnet lherzolite with a coarse texture

Opx (60%) dominates the mineralogy and occasionally has olivine inclusions. Olivine (30%) occurs mainly along opx grain boundaries and major cracks. Garnet (10%) has dark brown kelyphite rims surrounded by a phlogopite outer rim. Cpx occurs as small anhedral grains in trace amounts.

LBM 8

Garnet harzburgite with a coarse texture

The mineralogy is dominated by intensely fractured olivine (60%) with a long dimension which are up to 3 mm. Opx (35%) occurs as anhedral 3 mm grains. Garnet (5%) occurs as fractured 1 mm grains with dark brown kelyphite rims surrounded by a phlogopite outer rim.

LBM 9

Garnet lherzolite with a coarse texture

Opx (50%) dominates the mineralogy, occurring as subhedral to anhedral grains that are up to 3 mm. Olivine (40%) is anhedral and up to 5 mm. Garnet (7%) is up to 2 mm and has dark-brown kelyphite rims, occasionally surrounded by phlogopite rims. Cpx (3%) shows some association with the alteration of garnet.

Appendix B

Analytical Methods

B1. Analytical Conditions for the electron microprobe

Instrument: Cameca Camebax Microbeam electron microprobe
Accelerating Potential: 15 kV
Beam Current: 40 nA
Beam Diameter: 1 µm
Counting Time: 10 seconds for all elements and 30 seconds for Ni in olivine

Analysing crystals:

TLAP for Na, Mg, Si and Al
LIF200 for Fe, Mn and Ni
PET for Ca, K, Ti and Cr

Standards and errors:

	Garnet		Pyroxenes		Olivine	
	Std	**1sigma**	**Std**	**1sigma**	**Std**	**1sigma**
Si	K-P	0.21	DIOP	0.22	M-OL	0.21
Ti	RUT	0.01	RUT	0.02	RUT	0.01
Al	K-P	0.16	K-P	0.04	K-P	0.02
Cr	CHRO	0.03	CHRO	0.03	CHRO	0.02
Fe	K-P	0.18	K-P	0.09	M-OL	0.14
Mn	RHOD	0.04	RHOD	0.03	RHOD	0.02
Mg	K-P	0.13	DIOP	0.24	K-P	0.26
Ca	K-P	0.07	DIOP	0.11	—	—
Na	—	—	K-H	0.06	—	—
K	—	—	K-H	0.01	—	—
Ni	—	—	—	—	NISI	0.02

B2. The NAC proton microprobe

The NAC proton microprobe facility was purchased from Oxford Instruments and as such most of the main parts are standard Oxford features. These features include the standard Oxford triplet of lenses, scanning coils, object and halo slit assemblies, lens and steering coil power supplies, and sample target chamber (Prozesky *et al.*, 1995).

The PMP is schematically shown in Fig. B.1. A Van de Graaff generator accelerates ions vertically downwards. After energy stabilisation and beam selection, made by a 90^0 analysing magnet, the ions travel through a ±15m-flight path to the target (Prozesky *et al.*, 1995). Although this long flight path offers opportunities for the achievement of ultimate beam spot sizes, it also makes the PMP more susceptible to beam instabilities. The energy of the ions is stabilised by slits in front of the main beamstop. After passing through these slits, the ions pass through a quadrupole doublet for focusing of the beam at the object slits. The rest of the flight path is just 7.5m, with the halo slits situated 1m before the target (Prozesky *et al.*, 1995).

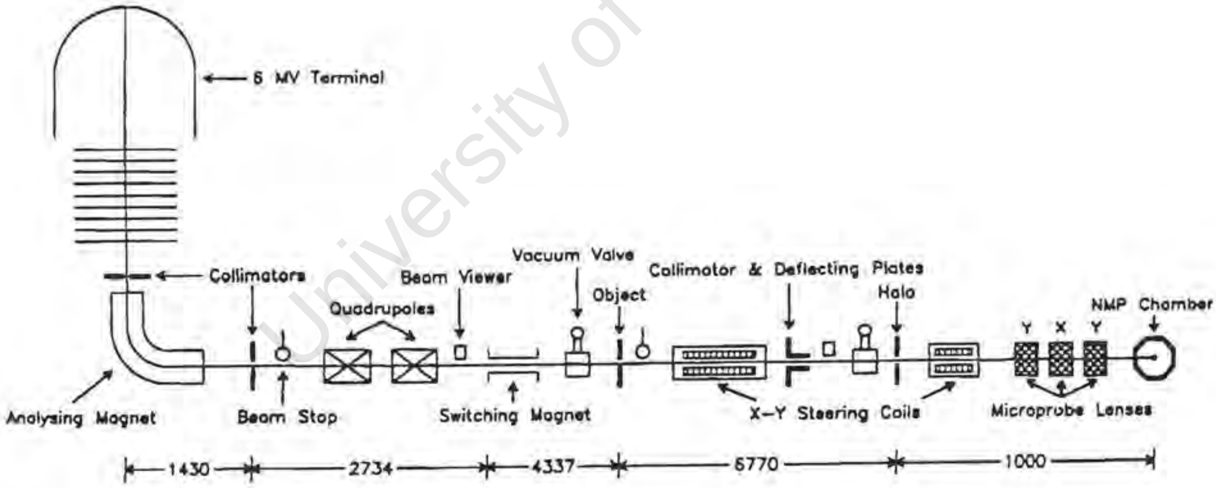

Fig. B.1. A schematic representation of the Van de Graaff accelerator with the proton microprobe layout at NAC showing the most important features with distances between key points in mm (not to scale). Taken from Prozesky *et al.* (1995).

The sample is positioned using the stepper motor control with the X, Y and Z-axes. Co-ordinate readings of the mouse and scanning regions are indicated on the screen, allowing area identification and distance calibration. The sample is viewed using a high-magnification optical microscope placed at an angle of 45^0 to the sample surface (Fig. B.2). There are two light sources in the sample chamber, in front of and behind the sample, respectively, for the illumination of reflected and transmitted light.

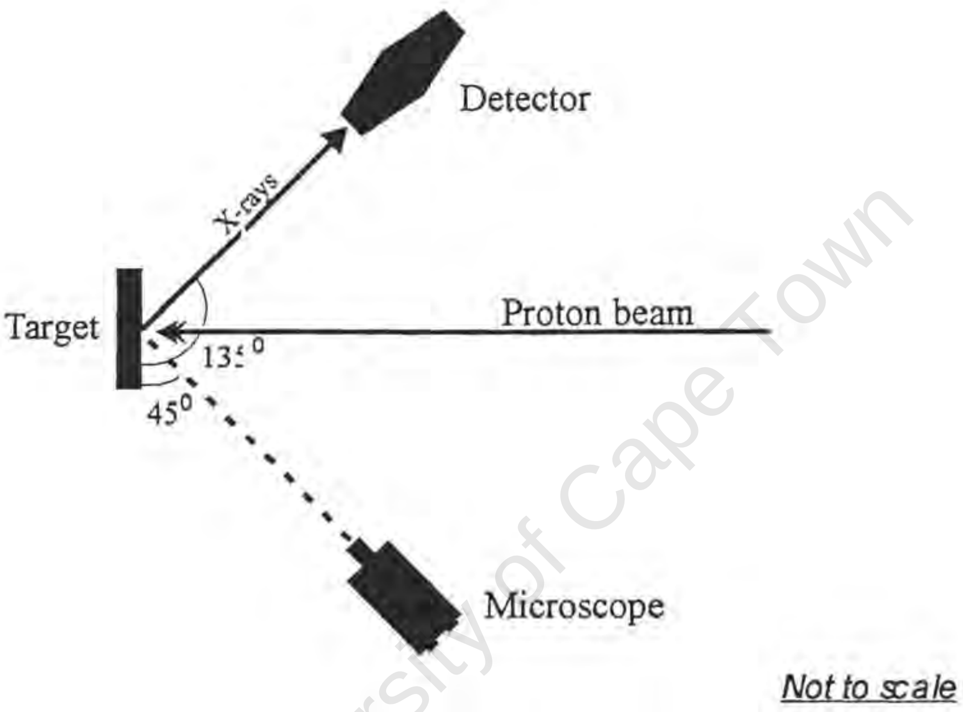

Fig. B.2. A schematic illustration of the geometry of the proton beam, binocular microscope, X-ray detector and target specimen in most Oxford instruments, including the NAC PMP. The detector is placed at 135^0, the microscope is placed at 45^0 and the incident proton beam is normal to the sample surface.

The beam strikes the sample at a normal angle to the sample surface. The X-rays emitted by the sample leave the surface at an angle towards a Si(Li) X-ray detector placed at 135^0 to the sample surface (Fig. B.2). Signals from the detector are fed to the electronic units for amplification and digitisation. The interpretation of the PIXE spectra at NAC, for trace element determination, is done using the GeoPIXE software package (Ryan *et al.*, 1990, Ryan and Jamieson, 1993). This software package allows analyses of thick and thin specimen X-ray spectra, with complete thick target corrections for beam stopping, X-ray attenuation and secondary fluorescence. In addition, the software has an ability of doing on-line dynamic analysis of X-ray spectra and on-line elemental mapping, which is very useful in quick identification of microscopic inclusions and element domains within areas to be analysed.

The PMP, like any vertically mounted instrument, has large beam instabilities related to vertical movement of the beam as a result of the vertical acceleration of the proton beam. These instabilities lead to the movement or pulsation of the beam on the target surface, which manifests itself in high dead times for relatively low count rates. This prompted the design of an on-demand beam deflection system, consisting of a set of two symmetric plates, which are charged in such a way that they deflect the beam from the target (Prozesky *et al.*, 1995). The deflection of the beam gives the amplifier time to process each signal without interferences from the next signals. The successful elimination of problems associated with excessive dead times by the on-demand beam deflection system has led to the routine usage of the system at the NAC proton microprobe facility for trace element analysis.

B3. The DTM ion microprobe

The DTM ion microprobe is a Cameca IMS-6F instrument. Its primary ion optics consists of two ion sources (Fig. B.3), a magnetic sector and a group of electrostatic optical lenses. The two ion sources are a duoplasmatron, capable of producing positive and negative ions, and a surface thermo-ionization Cs Microbeam Source, capable of producing Cs^+ ions. Whether the duoplasmatron supplies positive or negative ions is controlled by the polarity of the extraction potential. In the Cs Microbeam Source Cs^+ ions are produced by the vaporisation of a caesium chromate (Cs_2CrO_4) tablet.

Between the ion sources and the primary optics is a primary beam mass filter, which is a symmetrical prismatic magnet. The mass filter and the ion sources are positioned in an Y-shaped geometry such that the facility has the two ion sources available at all times

(Fig. B.3), allowing a simple switchover from one source to the other, without breaking the vacuum.

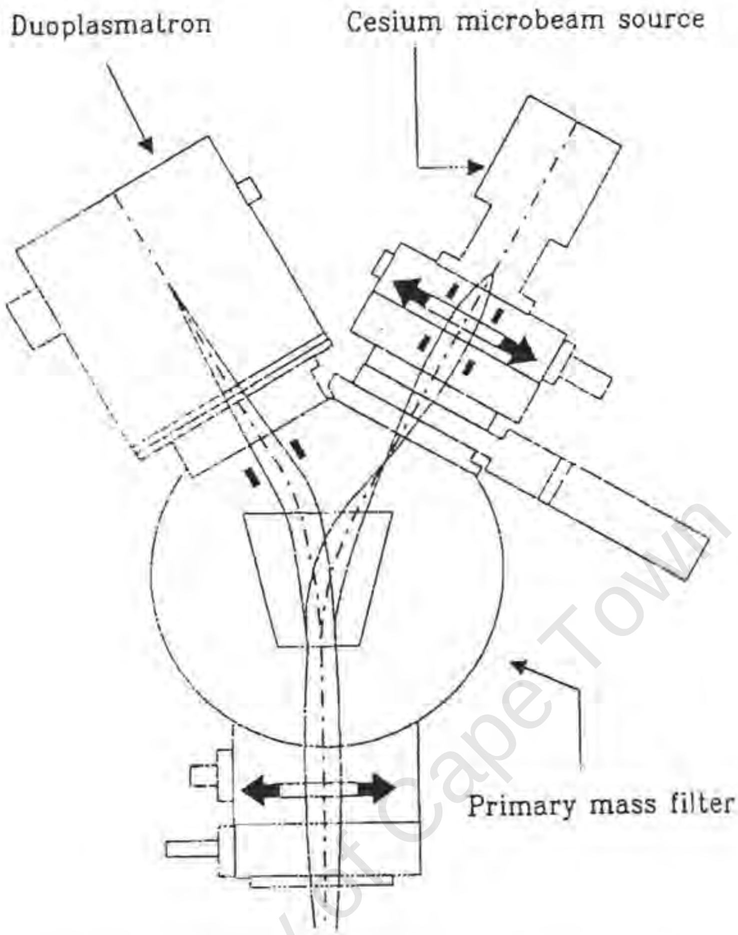

Fig. B.3. The Y-shaped geometry of the ion sources and the primary mass filter at the DTM IMP facility. Taken from the *IMS6-F/IMS1270 Users' Guide*.

From the primary beam mass filter the beam goes through a series of electrostatic lenses and deflectors for focusing, centering and rastering the beam onto the target specimen. Just before the final aperture in front of the target surface there is a ring-shaped Faraday cup for the measurement of the primary beam intensity.

The ionised secondary ions produced by sputtering of a sample surface are accelerated from the sample surface by the electrostatic field between the sample (polarised at high voltage) and the extraction electrode (at ground potential). These ions are then focused to the entrance slit of the mass spectrometer by electrostatic lenses. The main components of the secondary ion beam optics are electrostatic lenses and slits, the mass spectrometer, and ion detectors.

The ion microprobe is equipped with a double focusing mass spectrometer to achieve high resolutions. The mass spectrometer is designed in a Nier-Johanson configuration (Shimizu, 1997; Fig. B.4), which combines a 90^0 electrostatic sector with a 90^0 magnetic sector. In this type of configuration, the electrostatic analyser rejects ions whose energies lie outside a predetermined range.

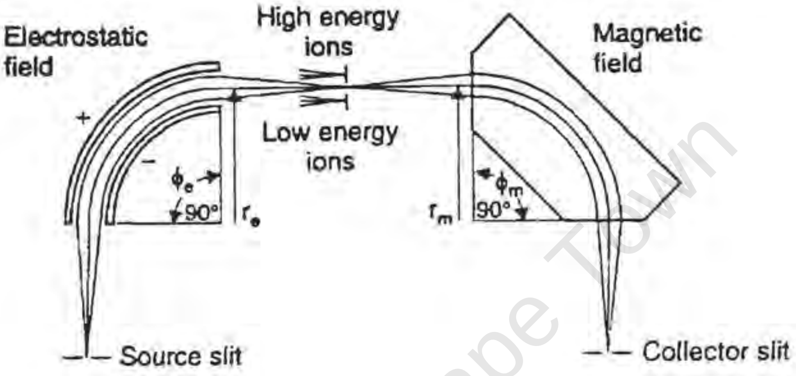

Fig. B.4. The Nier-Johnson geometry of a double-focussing mass spectrometer; ϕ_e and ϕ_m represent angles of ion trajectories in the electrostatic and magnetic fields respectively, r_e and r_m are the radii of curvature in the electrostatic and magnetic fields respectively. Taken from Shimizu (1997). This is the geometry of the mass spectrometer at the DTM ion microprobe facility.

From the mass spectrometer the mass filtered secondary ion beam goes through the exit slit and enters a system of lenses. The beam is then focused onto a direct image ion detector. The image ion detector is a microchannel plate (MCP) device coupled to a fluorescent screen. The fluorescent screen image is acquired by means of a [1]CCD camera and displayed on a computer screen. The MCP is an assembly of small channels, each being a hollow glass tube with an inner emissive or conductive layer. The surface of this layer emits secondary electrons when struck by secondary ions. The number of secondary electrons emitted per secondary ion (the gain or counts) is directly proportional to the potential applied across the detector, and inversely proportional to the mass of the secondary ions.

---

[1] CCD = Charge Coupled Device

To provide a very high dynamic range for the secondary intensity measurements the IMS 6F is equipped with a combination of a Faraday cup and an electron multiplier (EM) ion detector for the measurement of count rates (counts per second). The Faraday cup is a hollow cylinder with a large length/diameter ratio. The EM is made of twenty-one stages of Cu/Be [2]dynodes and works in a direct pulse mode.

B4. The UCT LA-ICP-MS

The ICP-MS at UCT is a Perkin-Elmer SCIEX *Elan 6000* instrument utilising a single autolens ion optic system and a quadrupole mass spectrometer. The instrument is fully automated.

The laser component is a *CETAC LSX-100 laser* equipped with a Nd:YAG ultraviolet laser, frequency-quadrupled to a wavelength of 266 nm and operating at an energy output of 3 mJ. The system has a high resolution CCD camera, and a continuously variable magnification zoom lens. The sample and the laser firing process are viewed on a TV monitor which is integrated with a targeting image from the crosshair generator.

---

[2] A dynode is an additional electrode in a photomultiplier tube, which undergoes secondary emission upon bombardment, thus effects amplification.

Appendix C.1

Trace element data for the peridotite garnets, analysed by PIXE, SIMS and LA-ICP-MS.

n = number of analyses for PIXE and Laser, and = number of blocks of data for one analysis for SIMS (except Ni for which n = number of analyses).

c = core

r = rim

errors are 2σ errors

blanks in the tables = where data are not available

		J117		JJG1710		JJG1716		JJG1728		JJG1729		JJG1733		JJG1757		JJG1761	
		n	Mean	n	Mean	n	Mean	n	Mean	n	Mean	n	Mean	n	Mean	n	Mean
PIXE	Ni	6	85 ± 2	6	102 ± 4	6	16.4 ± 1.3	6	35 ± 3	12	94 ± 3	12	14.1 ± 1.1	6	57 ± 3	6	35 ± 1
	Zn	6	12.0 ± 1.8	6	10.6 ± 0.5	6	8.3 ± 0.6	6	8.3 ± 0.9	12	16.1 ± 1.0	12	6.5 ± 0.4	6	8.4 ± 1.0	6	7.2 ± 0.5
	Ga	6	10.0 ± 1.4	6	9.2 ± 0.8	6	3.8 ± 0.8	6	2.1 ± 0.9	12	13.2 ± 0.9	12	2.1 ± 0.4	6	2.6 ± 1.0	6	2.1 ± 0.7
	Y	6	12.2 ± 0.9	6	13.6 ± 1.2	6	17.8 ± 1.4	6	6.4 ± 2.0	12	20 ± 2	12	9.0 ± 1.5	6	<4ppm	6	4.4 ± 0.8
	Zr	6	32 ± 1	6	33 ± 2	6	34 ± 2	6	70 ± 8	12	50 ± 6	12	14.7 ± 1.2	6	23 ± 1	6	58 ± 2
LAICPMS	Sc	6	76 ± 6	4	107 ± 5	6	97 ± 4	2	124 ; 127	5	79 ± 4			2	125 ; 113	8	166 ± 8
	V	6	226 ± 14	4	259 ± 12	6	98 ± 6	2	166 ; 170	5	211 ± 8			2	221 ; 213	8	193 ± 3
	Ni	6	112 ± 10	4	96 ± 14	6	17.9 ± 3.6	2	34 ; 34	5	78 ± 5			2	62 ; 53	8	45 ± 2
	Ga	6	16.5 ± 3.1	4	8.1 ± 0.7	6	4.0 ± 1.5	2	1.34 ; 1.2	5	10.5 ± 0.8			2	2.3 ; 2.6	8	2.8 ± 0.2
	Y	6	20 ± 1	4	13.1 ± 0.6	6	15.9 ± 0.8	2	18 ; 23	5	21 ± 2			2	2.0 ; 1.8	8	4.3 ± 0.3
	Zr	6	52 ± 3	4	31 ± 2	6	33 ± 3	2	159 ; 177	5	50 ± 5			2	26 ; 27	8	58.5 ± 2.8
	Yb	6	2.5 ± 0.1	4	1.4 ± 0.1	6	1.6 ± 0.1	2	0.31 ; 0.45	5	2.5 ± 0.1			2	0.24 ; 0.12	8	0.22 ± 0.02
SIMS	Sc	4	66 ± 1	4	91 ± 1									4	108 ± 1		
	Ni	2	95 ± 0.3			2	17.7 ± 0.4							2	69 ± 0.3	2	36 ± 0.2
	Sr	4	1.2 ± 0.2	4	1.1 ± 0.1									4	1.3 ± 0.2		
	Y	4	19 ± 1	4	16.1 ± 0.5									4	1.8 ± 0.1		
	Zr	4	57 ± 2	4	38 ± 1									4	29 ± 1		
	Yb	4	2.2 ± 0.1	4	1.7 ± 0.1									4	0.22 ± 0.01		

		JJG864		JJH1		JJH10		JJH23		JJH28		JJH29		JJH32		JJH35	
		n	Mean	n	Mean	n	Mean	n	Mean	n	Mean	n	Mean	n	Mean	n	Mean
PIXE	**Ni**	6	26 ± 5	6	63 ± 3	6	100 ± 5	6	73 ± 5	6	77 ± 5	6	92 ± 2	12	99 ± 2	6	71 ± 3
	Zn	6	12.1 ± 3.2	6	10.3 ± 1.2	6	13.6 ± 0.8	6	11.1 ± 1.6	6	12.1 ± 0.9	6	10.7 ± 1.1	12	10.4 ± 0.7	6	11.0 ± 1.0
	Ga	6	2.8 ± 0.7	6	8.6 ± 0.9	6	11.1 ± 1.6	6	7.0 ± 0.9	6	9.9 ± 0.5	6	4.7 ± 0.5	12	8.3 ± 0.6	6	7.4 ± 0.7
	Y	6	12.8 ± 3.7	6	4.2 ± 1.3	6	18.1 ± 1.2	6	<4ppm	6	13.7 ± 1.2	6	4.8 ± 0.8	12	14.8 ± 0.7		<4ppm
	Zr	6	85 ± 9	6	14.7 ± 5.6	6	41 ± 5	6	35 ± 4	6	18.7 ± 1.5	6	79 ± 8	12	43 ± 5	6	8.2 ± 1.1
LA ICPMS	**Sc**	4	110 ± 5	5	97 ± 7	6	96 ± 4			12	95 ± 3	7	164 ± 11	9	103 ± 4		
	V	4	136 ± 10	5	298 ± 14	6	245 ± 18			12	277 ± 11	7	281 ± 37	9	279 ± 20		
	Ni	4	26 ± 3	5	72 ± 5	6	86 ± 2			12	72 ± 3	7	88 ± 7	9	100 ± 10		
	Ga	4	2.1 ± 0.1	5	9.7 ± 0.4	6	10.1 ± 0.8			12	8.9 ± 0.6	7	3.9 ± 0.6	9	8.9 ± 1.1		
	Y	4	9.5 ± 4.6	5	4.2 ± 0.6	6	17.8 ± 1.1			12	12.7 ± 0.5	7	6.2 ± 4.0	9	13.3 ± 0.4		
	Zr	4	67 ± 3	5	13.6 ± 9.0	6	36 ± 5			12	16.7 ± 0.4	7	73 ± 26	9	32 ± 2		
	Yb			5	0.56 ± 0.05	6	2.1 ± 0.2			12	1.7 ± 0.1	7	0.59 ± 0.19	9	1.6 ± 0.1		
SIMS	**Sc**	4	97 ± 1	4	98 ± 1											4	134 ± 1
	Ni	2	32 ± 0.2	2	89 ± 0.2	2	100 ± 0.3			2	77 ± 0.3			2	88 ± 0.3		
	Sr	4	0.82 ± 0.20	4	1.0 ± 0.1											4	0.82 ± 0.12
	Y	4	9.9 ± 0.4	4	4.9 ± 0.1											4	2.8 ± 0.1
	Zr	4	84 ± 3	4	18.4 ± 0.8											4	11.3 ± 0.2
	Yb	4	0.80 ± 0.02	4	0.68 ± 0.04											4	0.52 ± 0.02

		JJH6		JJH7		JJH8		JJH9		LBM10		LBM16C		LBM16R		LBM17	
		n	**Mean**	**n**	**Mean**	**n**	**Mean**	**n**	**Mean**	**n**	**Mean**	**n**	**Mean**	**n**	**Mean**	**n**	**Mean**
PIXE	**Ni**	3	77 ± 7	12	101 ± 4	6	99 ± 3	6	77 ± 5	6	41 ± 3	3	45 ± 12	3	49 ± 4	6	46 ± 3
	Zn	3	11.1 ± 3.9	12	12.8 ± 0.7	6	11.5 ± 1.0	6	11.1 ± 1.1	6	8.5 ± 0.7	3	8.4 ± 4.0	3	7.6 ± 1.9	6	8.2 ± 1.4
	Ga	3	5.2 ± 2.5	12	9.7 ± 1.0	6	7.5 ± 0.6	6	7.1 ± 1.2	6	2.6 ± 0.4	3	3.4 ± 0.9	3	3.2 ± 0.8	6	3.0 ± 0.5
	Y		<4ppm	12	17.2 ± 3.0	6	10.3 ± 1.6	6	<4ppm	6	4.2 ± 1.1	3	22 ± 5	3	31 ± 12	6	4.9 ± 2.8
	Zr	3	18.1 ± 3.2	12	70 ± 6	6	50 ± 3	6	<3.5ppm	6	47 ± 5	3	110 ± 20	3	142 ± 23	6	57 ± 6
LA ICPMS	**Sc**	3	233 ± 15			1	138	3	206 ± 7	4	103 ± 9	4	120 ± 10	2	86 ; 98	4	90 ± 3
	V	3	575 ± 86			1	303	3	459 ± 40	4	252 ± 46	4	128 ± 6	2	103 ; 119	4	203 ± 23
	Ni	3	81 ± 8			1	100	3	75 ± 19	4	45 ± 3	4	40 ± 3	2	32 ; 40	4	47 ± 11
	Ga	3	4.4 ± 1.5			1	6.4	3	6.6 ± 2.9	4	2.9 ± 0.3	4	2.7 ± 0.4	2	2.3 ; 3.3	4	2.8 ± 0.8
	Y	3	1.9 ± 0.1			1	6.6	3	1.3 ± 0.5	4	5.8 ± 2.3	4	25 ± 4	2	16.6 ; 14.6	4	3.5 ± 2.1
	Zr	3	15.4 ± 1.1			1	49	3	1.1 ± 0.3	4	64 ± 8	4	123 ± 12	2	88 ; 81	4	52 ± 10
	Yb	3	0.28 ± 0.08			1	0.76	3	0.36 ± 0.03			4	2.3 ± 0.7	2	1.5 ; 1.1	4	0.27 ± 0.13
SIMS	**Sc**			4	101 ± 1	4	149 ± 2			4	94 ± 1	4	119 ± 1			4	74 ± 1
	Ni			2	108 ± 0.3		113 ± 0.3			2	57 ± 0.2					2	52 ± 0.3
	Sr			4	1.4 ± 0.2	4	1.7 ± 0.2			4	0.89 ± 0.14	4	0.85 ± 0.16			4	0.81 ± 0.12
	Y			4	11.3 ± 0.4	4	10.2 ± 0.4			4	9.2 ± 0.4	4	29 ± 1			4	2.3 ± 0.1
	Zr			4	61 ± 2	4	64 ± 2			4	9.1 ± 0.4	4	154 ± 4			4	59.6 ± 1.3
	Yb			4	1.3 ± 0.1	4	1.1 ± 0.1			4	0.67 ± 0.05	4	2.7 ± 0.1			4	0.30 ± 0.01

		LBM3		LBM30		LBM32		LBM36-2		LBM36-3		LBM6		LBM8C		LBM8R		LBM9	
		n	Mean	n	Mean	n	Mean	n	Mean	n	Mean	n	Mean	n	Mean	n	Mean	n	Mean
PIXE	Ni	9	46 ± 2	3	48 ± 8	9	35 ± 2	9	48 ± 2	6	54 ± 4	6	56 ± 3	6	44 ± 3	6	42 ± 4	6	43 ± 2
	Zn	9	10.0 ± 1.3	3	11.2 ± 2.3	9	11.3 ± 0.5	9	14.9 ± 0.9	6	13.0 ± 1.4	6	11.8 ± 1.5	6	7.6 ± 1.7	6	7.6 ± 1.2	6	8.6 ± 1.7
	Ga	9	6.5 ± 2.9	3	11.4 ± 2.6	9	6.7 ± 0.6	9	6.7 ± 1.0	6	8.8 ± 1.2	6	8.8 ± 1.4	6	2.6 ± 0.5	6	2.1 ± 1.1	6	4.9 ± 1.0
	Y	9	<4ppm	3	33 ± 6	9	40 ± 6	9	24 ± 3	6	25 ± 1	6	10.0 ± 1.6	6	5.6 ± 2.5	6	22 ± 7	6	6.0 ± 1.2
	Zr	9	33 ± 4	3	138 ± 15	9	109 ± 15	9	70 ± 4	6	73 ± 5	6	28 ± 3	6	49 ± 13	6	124 ± 13	6	55 ± 10
LAICPMS	Sc									3	135 ± 9	4	127 ± 7	6	106 ± 3	2	108 ; 109	5	98 ± 7
	V									3	210 ± 79	4	264 ± 8	6	245 ± 20	2	202 ; 208	5	231 ± 23
	Ni									3	53 ± 5	4	53 ± 4	6	41 ± 5	2	46 ; 46	5	39 ± 2
	Ga									3	9 ± 2	4	8.3 ± 0.5	6	2.1 ± 0.2	2	2.0 ; 2.0	5	4.2 ± 0.3
	Y									3	19 ± 6	4	9.7 ± 0.6	6	2.7 ± 0.3	2	11.7 ; 29	5	2.9 ± 0.6
	Zr									3	61 ± 22	4	27 ± 2	6	37 ± 6	2	99 ; 152	5	35 ± 3
	Yb									3	2.5 ± 0.5	4	1.5 ± 0.2	6	0.34 ± 0.04	2	0.70 ; 2.5	5	0.46 ± 0.10
SIMS	Sc					4	114 ± 1	4	137 ± 1	4	126 ± 2			4	109 ± 1			4	97 ± 0.5
	Ni		48 ± 0.2			2	50 ± 0.2	2	62 ± 0.2	2	58 ± 0.2			2	55 ± 0.2			2	53 ± 0.3
	Sr					4	1.4 ± 0.2	4	1.1 ± 0.2	4	0.9 ± 0.2			4	1.4 ± 0.2			4	1.2 ± 0.2
	Y					4	31 ± 0.5	4	18.3 ± 0.8	4	23 ± 1			4	18.1 ± 0.8			4	12.0 ± 0.3
	Zr					4	113 ± 2	4	70 ± 3	4	83 ± 4			4	135 ± 5			4	102 ± 3
	Yb					4	3.0 ± 0.1	4	2.3 ± 0.1	4	2.9 ± 0.2			4	1.5 ± 0.1			4	1.2 ± 0.1

Appendix C.2

Major (wt%) and trace (ppm) data determined by PIXE for the garnet megacrysts from which garnet secondary standards were selected.

	SiO_2	TiO_2	Al_2O_3	Cr_2O_3	FeO	MnO	MgO	CaO	Total	Ni(ppm)	Zn(ppm)	Ga(ppm)	Y(ppm)	Zr(ppm)
FSM40	42.45	0.86	21.49	1.71	8.96	0.26	20.70	4.22	100.64	121 ± 6	27 ± 2	12.5 ± 1.5	28 ± 2	84 ± 2
FSM41	42.25	1.27	21.14	1.44	9.68	0.25	19.89	5.00	100.92	121 ± 5	29 ± 2	16.6 ± 2.0	28 ± 2	120 ± 3
FSM42	42.10	1.12	21.27	0.90	10.11	0.31	19.86	4.77	100.44	87 ± 4	28 ± 3	16.5 ± 1.3	33 ± 2	108 ± 3
FSM43	42.42	1.11	21.46	0.94	9.86	0.20	20.05	4.73	100.79	90 ± 4	28 ± 2	18.0 ± 1.7	32 ± 2	113 ± 3
FSM44	41.78	0.86	21.83	0.80	10.22	0.20	19.95	4.24	99.87	74 ± 4	28 ± 2	16.5 ± 1.5	29 ± 2	82 ± 4
FSM45	42.32	0.92	21.83	0.66	10.92	0.27	19.73	4.23	100.87	68 ± 5	31 ± 2	16.3 ± 1.3	28 ± 2	82 ± 3
FSM46	42.37	0.83	22.11	1.10	9.11	0.21	20.48	4.30	100.52	103 ± 5	27 ± 2	14.0 ± 1.6	27 ± 2	75 ± 2
FSM47	41.71	0.98	21.87	0.57	10.97	0.28	19.33	4.67	100.39	95 ± 5	30 ± 2	18.3 ± 1.4	38 ± 2	106 ± 3
FSM48	42.09	0.96	21.43	1.39	9.27	0.27	20.61	4.55	100.58	131 ± 6	27 ± 2	13.8 ± 1.5	29 ± 3	84 ± 3
FSM49	42.05	0.99	22.12	0.35	11.77	0.31	19.29	4.26	101.13	51 ± 4	31 ± 2	19.1 ± 1.7	25 ± 2	82 ± 3
FSM50	41.33	0.91	20.96	1.74	8.91	0.22	20.60	4.48	99.16	112 ± 5	24 ± 2	13.3 ± 1.5	27 ± 2	87 ± 3
LCR1	41.74	1.02	22.30	0.55	11.27	0.24	19.63	4.63	101.37	87 ± 5	32 ± 2	18.9 ± 1.7	35 ± 2	95 ± 3
LCR2	41.83	1.06	21.69	0.64	11.07	0.28	19.52	4.69	100.79	99 ± 5	28 ± 2	19.9 ± 1.5	36 ± 3	113 ± 3
MON29	41.97	0.58	21.50	2.22	7.37	0.27	20.99	4.86	99.76	114 ± 5	21 ± 1	10.6 ± 1.0	23 ± 1	71 ± 2
MON30	42.02	1.18	21.68	0.52	10.85	0.24	19.13	4.67	100.30	92 ± 5	34 ± 2	18.4 ± 1.4	41 ± 2	111 ± 3
MON31	42.69	0.87	21.47	1.66	8.69	0.21	20.85	4.63	101.07	121 ± 5	26 ± 2	13.9 ± 1.5	31 ± 2	86 ± 3
MON32*	41.72	1.10	21.92	0.27	11.58	0.31	18.72	4.54	100.17	65 ± 4	37 ± 2	21.1 ± 1.4	42 ± 2	122 ± 3
MON33	41.60	0.63	22.47	0.01	14.27	0.42	17.32	4.53	101.24	100 ± 5	30 ± 2	19.1 ± 1.4	36 ± 2	110 ± 3
MON34*	41.95	1.13	21.51	0.79	9.85	0.24	20.15	4.64	100.25	136 ± 7	34 ± 2	15.5 ± 1.4	43 ± 2	115 ± 4
MON35	42.09	1.12	21.56	0.67	10.03	0.22	19.81	4.78	100.27	124 ± 6	33 ± 2	15.6 ± 1.6	40 ± 2	122 ± 3
ROM33*	41.63	1.17	21.75	0.13	12.21	0.34	18.48	4.62	100.34	52 ± 4	35 ± 2	20.7 ± 1.6	46 ± 2	152 ± 3

The errors are 1σ errors. * denotes sample selected for making standards.

Appendix C.3

Major element (wt%) compositions of garnets, olivines, ortho- and clinopyroxenes analysed by electron microprobe

Abbreviations used:

(Fe is reported as total Fe in the tables and in the formulae involving Fe)

<LOD = less than detection limit

$$Fo = atomic\frac{Mg}{Mg+Fe}$$

$$Fa = atomic\frac{Fe}{Fe+Mg}$$

$$Ca = atomic\frac{Ca}{Ca+Mg+Fe}$$

$$Mg = atomic\frac{Mg}{Mg+Ca+Fe}$$

$$Fe = atomic\frac{Fe}{Ca+Mg+Fe}$$

$$Ca\# = atomic\frac{Ca}{Ca+Mg}$$

$$Mg\# = atomic\frac{Mg}{Fe+Mg}$$

Garnet Compositions - Jagersfontein

	J117	JJG1710	JJG1716	JJG1728	JJG1729	JJG1733	JJG1757	JJG1761	JJG864	JJH1	JJH10	JJH23	JJH28	JJH29	JJH32
SiO_2	42.46	42.23	41.88	41.96	41.63	41.60	42.04	41.99	41.96	41.17	41.87	40.34	42.62	41.36	41.76
TiO_2	0.70	0.34	0.07	0.04	0.61	<LOD	0.10	0.04	0.04	0.13	0.54	0.14	0.30	0.32	0.31
Al_2O_3	21.97	19.64	21.18	20.88	22.01	20.89	19.42	18.33	20.49	18.85	21.37	14.32	21.87	16.17	20.52
Cr_2O_3	1.58	5.27	2.87	5.49	1.64	2.55	7.21	7.61	4.38	6.18	2.92	11.39	3.18	9.65	3.81
FeO	7.87	6.33	7.95	6.15	8.38	8.68	5.59	5.21	7.32	7.43	7.52	6.76	7.10	6.48	6.63
MnO	0.25	0.21	0.52	0.34	0.29	0.49	0.35	0.26	0.42	0.34	0.30	0.34	0.33	0.35	0.24
MgO	20.38	21.45	19.82	21.20	20.27	19.65	23.55	21.82	20.52	19.90	21.47	18.23	20.49	21.12	21.51
CaO	4.23	5.19	5.12	4.69	4.38	5.19	2.23	4.11	5.02	5.91	4.74	7.73	4.93	4.77	4.87
Total	99.43	100.67	99.40	100.78	99.30	99.05	100.49	99.38	100.15	99.91	100.73	99.26	100.82	100.20	99.65
Atomic Proportions Based On Selected Number Of Oxygens															
Oxygens	12	12	12	12	12	12	12	12	12	12	12	12	12	12	12
Si	3.026	2.999	3.013	2.971	2.988	3.013	2.975	3.018	3.000	2.982	2.966	3.004	3.006	2.998	2.986
Ti	0.038	0.018	0.004	0.002	0.033	<LOD	0.005	0.002	0.002	0.007	0.029	0.008	0.016	0.017	0.017
Al	1.845	1.644	1.795	1.742	1.862	1.783	1.620	1.552	1.726	1.609	1.784	1.257	1.818	1.381	1.729
Cr	0.089	0.296	0.163	0.307	0.093	0.146	0.403	0.432	0.248	0.354	0.164	0.671	0.177	0.553	0.215
Fe	0.469	0.376	0.478	0.364	0.503	0.526	0.331	0.313	0.438	0.450	0.445	0.421	0.419	0.393	0.396
Mn	0.015	0.013	0.031	0.020	0.018	0.030	0.021	0.016	0.025	0.021	0.018	0.022	0.020	0.021	0.015
Mg	2.165	2.271	2.125	2.238	2.169	2.122	2.484	2.338	2.187	2.149	2.267	2.025	2.154	2.282	2.293
Ca	0.323	0.395	0.395	0.356	0.337	0.403	0.169	0.316	0.385	0.459	0.360	0.617	0.372	0.370	0.373
Sum	7.970	8.013	8.005	8.002	8.002	8.022	8.008	7.988	8.011	8.030	8.032	8.024	7.981	8.017	8.025
CA	10.92	12.98	13.16	12.03	11.19	13.20	5.67	10.66	12.79	15.00	11.71	20.14	12.65	12.16	12.18
MG	73.22	74.66	70.88	75.66	72.09	69.55	83.25	78.78	72.67	70.28	73.79	66.11	73.14	74.94	74.87
FE	15.86	12.36	15.95	12.31	16.72	17.24	11.08	10.55	14.55	14.72	14.50	13.75	14.21	12.90	12.94

Garnet Compositions - Jagersfontein

	JJH35	JJH6	JJH7	JJH8	JJH9
SiO_2	41.40	41.04	42.27	41.13	40.44
TiO_2	0.09	0.10	0.37	0.81	0.02
Al_2O_3	18.88	15.73	20.18	18.52	15.73
Cr_2O_3	6.38	11.36	5.43	6.09	10.32
FeO	6.84	6.73	6.91	7.57	7.29
MnO	0.31	0.32	0.25	0.34	0.31
MgO	20.07	16.96	20.14	20.60	18.21
CaO	6.09	8.24	5.22	5.43	7.79
Total	100.05	100.48	100.78	100.50	100.10

Atomic Proportions Based On Selected Number Of Oxyger

	JJH35	JJH6	JJH7	JJH8	JJH9
Oxygens	12	12	12	12	12
Si	2.987	3.012	3.005	2.963	2.981
Ti	0.005	0.006	0.020	0.044	0.001
Al	1.606	1.360	1.691	1.572	1.366
Cr	0.364	0.659	0.305	0.347	0.601
Fe	0.413	0.413	0.411	0.456	0.449
Mn	0.019	0.020	0.015	0.021	0.019
Mg	2.159	1.856	2.134	2.212	2.001
Ca	0.471	0.648	0.398	0.419	0.615
Sum	8.023	7.973	7.978	8.034	8.034
CA	15.47	22.21	13.51	13.57	20.07
MG	70.96	63.62	72.53	71.66	65.28
FE	13.56	14.16	13.96	14.77	14.66

Garnet Compositions - Matsoku

	LBM10	LBM16	LBM17	LBM30	LBM32	LBM36-2	LBM36-3	LBM3	LBM8	LBM9	LBM6	LBM20	LBM22
SiO_2	41.38	41.42	42.65	42.00	41.22	41.20	41.84	42.58	41.67	42.14	41.30	40.88	42.06
TiO_2	0.11	0.34	0.04	0.50	0.31	0.20	0.18	0.04	0.09	0.08	0.30	0.50	0.43
Al_2O_3	20.11	20.78	21.92	20.94	21.65	22.68	22.15	20.97	20.28	21.31	20.80	17.36	20.91
Cr_2O_3	4.87	4.17	3.62	3.64	2.63	1.88	2.18	5.00	5.28	3.99	4.14	6.71	3.30
FeO	6.69	6.60	6.28	7.62	9.10	10.37	10.46	6.86	6.31	7.06	8.73	8.98	7.94
MnO	0.32	0.32	0.30	0.38	0.36	0.42	0.43	0.32	0.32	0.34	0.41	0.48	0.36
MgO	20.62	21.86	20.97	20.72	19.89	19.07	19.12	19.82	20.82	20.97	18.01	18.44	20.63
CaO	5.33	4.50	4.86	4.76	4.20	4.56	4.70	5.78	5.51	5.00	5.37	5.98	4.46
Total	99.44	99.99	100.64	100.56	99.36	100.38	101.05	101.36	100.28	100.88	99.05	99.34	100.08
Atomic Proportions Based On Selected Number Of Oxygens													
Oxygens	12	12	12	12	12	12	12	12	12	12	12	12	12
Si	2.981	2.955	3.004	2.986	2.973	2.954	2.982	3.006	2.975	2.981	3.004	3.010	3.002
Ti	0.006	0.018	0.002	0.027	0.017	0.011	0.010	0.002	0.005	0.004	0.016	0.028	0.023
Al	1.707	1.747	1.819	1.755	1.840	1.916	1.861	1.745	1.706	1.777	1.783	1.506	1.759
Cr	0.277	0.235	0.202	0.205	0.150	0.107	0.123	0.279	0.298	0.223	0.238	0.390	0.186
Fe	0.403	0.394	0.370	0.453	0.549	0.622	0.623	0.405	0.377	0.418	0.531	0.553	0.474
Mn	0.020	0.019	0.018	0.023	0.022	0.026	0.026	0.019	0.019	0.020	0.025	0.030	0.022
Mg	2.215	2.325	2.202	2.196	2.139	2.038	2.032	2.086	2.216	2.212	1.953	2.024	2.195
Ca	0.411	0.344	0.367	0.363	0.325	0.350	0.359	0.437	0.421	0.379	0.418	0.472	0.341
Sum	8.020	8.036	7.983	8.007	8.015	8.024	8.016	7.980	8.018	8.014	7.969	8.014	8.002
CA	13.58	11.23	12.48	12.04	10.77	11.64	11.91	14.93	13.98	12.60	14.42	15.48	11.34
MG	73.11	75.91	74.93	72.92	71.00	67.71	67.41	71.24	73.52	73.52	67.29	66.38	72.91
FE	13.31	12.86	12.59	15.04	18.22	20.65	20.68	13.83	12.50	13.88	18.29	18.14	15.75

Olivine Compositions - Jagersfontein

	J117	JJG1710	JJG1716	JJG1728	JJG1729	JJG1733	JJG1757	JJG1761	JJG864	JJH1	JJH10	JJH23	JJH28	JJH29	JJH32
SiO2	41.33	41.08	40.17	41.04	40.32	39.92	41.79	41.04	40.36	40.32	40.03	40.14	41.09	40.86	41.17
TiO2	<LOD	<LOD	<LOD	<LOD	0.03	<LOD	<LOD	<LOD	<LOD	<LOD	<LOD	<LOD	<LOD	<LOD	<LOD
Al2O3	<LOD	0.04	<LOD	<LOD	<LOD	<LOD	<LOD	0.03	0.03	<LOD	<LOD	<LOD	0.03	<LOD	<LOD
Cr2O3	<LOD	0.07	<LOD	<LOD	0.03	<LOD	0.07	<LOD	<LOD	<LOD	0.04	<LOD	<LOD	0.08	0.04
FeO	9.94	7.64	7.46	6.59	9.93	7.28	6.58	5.56	7.34	9.06	9.07	8.73	8.78	7.68	7.97
MnO	0.10	0.14	0.13	0.10	0.11	0.08	0.09	0.10	0.11	0.11	0.11	0.07	0.10	0.05	0.07
MgO	48.90	51.17	51.50	51.44	49.98	51.54	52.08	51.97	51.46	49.92	50.25	50.60	50.30	51.21	50.95
CaO	0.08	0.08	<LOD	<LOD	0.07	<LOD	<LOD	<LOD	<LOD	0.07	0.06	<LOD	0.06	0.04	0.05
NiO	0.3640	0.3805	0.4060	0.3678	0.3792	0.4060	0.3372	0.3271	0.4327	0.3920	0.3996	0.3920	0.3818	0.3780	0.3894
Total	100.73	100.62	99.70	99.58	100.89	99.28	100.98	99.08	99.75	99.88	100	99.95	100.77	100.35	100.69

Atomic Proportions Based On Selected Number Of Oxygens

	J117	JJG1710	JJG1716	JJG1728	JJG1729	JJG1733	JJG1757	JJG1761	JJG864	JJH1	JJH10	JJH23	JJH28	JJH29	JJH32
Oxygens	4	4	4	4	4	4	4	4	4	4	4	4	4	4	4
Si	1.006	0.993	0.981	0.997	0.983	0.978	1.000	0.997	0.984	0.989	0.982	0.982	0.996	0.990	0.995
Ti	<LOD	<LOD	<LOD	<LOD	0.001	<LOD	<LOD	<LOD	<LOD	<LOD	<LOD	<LOD	<LOD	<LOD	<LOD
Al	<LOD	0.001	<LOD	<LOD	<LOD	<LOD	<LOD	0.001	0.001	<LOD	<LOD	<LOD	0.001	<LOD	<LOD
Cr	<LOD	0.001	<LOD	<LOD	0.001	<LOD	0.001	<LOD	<LOD	<LOD	0.001	<LOD	<LOD	0.002	0.001
Fe	0.202	0.154	0.152	0.134	0.202	0.149	0.132	0.113	0.150	0.186	0.186	0.179	0.178	0.156	0.161
Mn	0.002	0.003	0.003	0.002	0.002	0.002	0.002	0.002	0.002	0.002	0.002	0.001	0.002	0.001	0.001
Mg	1.774	1.843	1.874	1.863	1.817	1.883	1.857	1.882	1.870	1.825	1.837	1.846	1.817	1.850	1.836
Ca	0.002	0.002	<LOD	<LOD	0.002	<LOD	<LOD	<LOD	<LOD	0.002	0.002	<LOD	0.002	0.001	0.001
Ni	0.007	0.007	0.008	0.007	0.007	0.008	0.006	0.006	0.008	0.008	0.008	0.008	0.007	0.007	0.008
Sum	2.994	3.006	3.019	3.003	3.016	3.021	2.999	3.002	3.015	3.011	3.018	3.017	3.003	3.008	3.004
Fo	89.77	92.27	92.48	93.30	89.97	92.66	93.38	94.34	92.60	90.76	90.81	91.17	91.09	92.24	91.93
Fa	10.23	7.73	7.52	6.70	10.03	7.34	6.62	5.66	7.40	9.24	9.19	8.83	8.91	7.76	8.07

Olivine Compositions - Jagersfontein

	JJH35	JJH6	JJH7	JJH8	JJH9
SiO2	40.66	40.98	41.33	39.78	40.33
TiO2	<LOD	0.03	0.04	<LOD	<LOD
Al2O3	<LOD	<LOD	<LOD	0.07	0.03
Cr2O3	<LOD	0.04	0.07	0.05	0.05
FeO	8.54	8.41	8.60	8.96	8.70
MnO	0.11	0.05	0.10	0.16	0.06
MgO	50.90	50.18	50.17	50.75	50.44
CaO	0.04	0.07	0.07	0.07	0.07
NiO	0.3665	0.3945	0.3500	0.3869	0.3881
Total	100.68	100.16	100.73	100.21	100.09

Atomic Proportions Based On Selected Number Of Oxygen

	JJH35	JJH6	JJH7	JJH8	JJH9
Oxygens	4	4	4	4	4
Si	0.987	0.998	1.000	0.974	0.986
Ti	<LOD	0.001	0.001	<LOD	<LOD
Al	<LOD	<LOD	<LOD	0.002	0.001
Cr	<LOD	0.001	0.001	0.001	0.001
Fe	0.173	0.171	0.174	0.183	0.178
Mn	0.002	0.001	0.002	0.003	0.001
Mg	1.841	1.821	1.810	1.852	1.838
Ca	0.001	0.002	0.002	0.002	0.002
Ni	0.007	0.008	0.007	0.008	0.008
Sum	3.013	3.002	2.998	3.025	3.014
Fo	91.40	91.41	91.23	90.99	91.18
Fa	8.60	8.59	8.77	9.01	8.82

Olivine Composition - Matsoku Peridotites

	LBM10	LBM16	LBM17	LBM20	LBM22	LBM3	LBM30	LBM32	LBM36-2	LBM36-3	LBM6	LBM8	LBM9
SiO2	40.85	41.73	41.34	39.79	39.58	40.91	41.36	40.71	39.64	40.49	40.97	41.82	41.18
TiO2	<LOD	0.03	<LOD	<LOD	0.06	<LOD	<LOD	<LOD	0.03	<LOD	<LOD	<LOD	<LOD
Al2O3	<LOD	0.04	<LOD	0.03	<LOD	0.02	<LOD	<LOD	<LOD	<LOD	<LOD	<LOD	0.03
Cr2O3	0.04	<LOD	0.03	<LOD	<LOD	0.04	<LOD	<LOD	<LOD	<LOD	0.05	0.04	<LOD
FeO	7.65	7.43	6.92	10.21	8.94	7.4	8.81	10.21	12.22	12.36	10.39	6.97	7.67
MnO	0.07	0.08	0.11	0.12	0.10	0.04	0.09	0.11	0.11	0.10	0.07	0.12	0.12
MgO	50.93	50.99	51.47	49.72	51.41	51.51	50.21	48.30	47.49	46.55	48.44	51.06	50.07
CaO	<LOD	0.04	0.03	<LOD	0.03	<LOD	<LOD	0.03	<LOD	0.03	0.03	0.03	0.03
NiO	0.4378	0.4199	0.4072	0.3894	0.3487	0.4301	0.3207	0.3576	0.4670	0.4556	0.4110	0.4314	0.4530
Total	100.02	100.80	100.31	100.25	100.49	100.36	100.85	99.77	100	100.01	100.38	100.47	99.58
Atomic Proportions Based On Selected Number Of Oxygens													
Oxygens	4	4	4	4	4	4	4	4	4	4	4	4	4
Si	0.993	1.004	0.998	0.978	0.966	0.990	1.001	1.002	0.986	1.005	1.003	1.007	1.004
Ti	<LOD	0.001	<LOD	<LOD	0.001	<LOD	<LOD	<LOD	0.001	<LOD	<LOD	<LOD	<LOD
Al	<LOD	0.001	<LOD	0.001	<LOD	0.001	<LOD	<LOD	<LOD	<LOD	<LOD	<LOD	0.001
Cr	0.001	<LOD	0.001	<LOD	<LOD	0.001	<LOD	<LOD	<LOD	<LOD	0.001	0.001	<LOD
Fe	0.156	0.150	0.140	0.210	0.183	0.150	0.178	0.210	0.254	0.256	0.213	0.140	0.156
Mn	0.001	0.002	0.002	0.003	0.002	0.001	0.002	0.002	0.002	0.002	0.002	0.002	0.002
Mg	1.846	1.828	1.852	1.822	1.871	1.858	1.811	1.773	1.761	1.722	1.768	1.833	1.821
Ca	<LOD	0.001	0.001	<LOD	0.001	<LOD	<LOD	0.001	<LOD	0.001	0.001	0.001	0.001
Ni	0.009	0.008	0.008	0.008	0.007	0.008	0.006	0.007	0.009	0.009	0.008	0.008	0.009
Sum	3.006	2.995	3.002	3.021	3.032	3.009	2.999	2.997	3.014	2.995	2.996	2.993	2.995
Fo	92.23	92.44	92.99	89.67	91.11	92.54	91.04	89.40	87.39	87.04	89.26	92.89	92.09
Fa	7.77	7.56	7.01	10.33	8.89	7.46	8.96	10.60	12.61	12.96	10.74	7.11	7.91

Orthopyroxene Compositions - Jagersfontein

	J117	JJG1710	JJG1716	JJG1728	JJG1729[§]	JJG1733	JJG1757	JJG1761	JJG864	JJH1	JJH10	JJH28	JJH29	JJH32	JJH35
SiO2	59.27	57.26	56.86	57.83	57.45	57.65	58.06	57.82	57.02	56.86	55.86	58.38	56.60	58.64	57.19
TiO2	0.16	0.07	0.03	<LOD	0.10	<LOD	<LOD	<LOD	<LOD	<LOD	0.21	0.09	0.10	0.10	0.03
Al2O3	1.05	0.93	0.68	1.28	0.85	0.68	0.81	0.84	0.71	0.76	0.98	0.80	0.87	0.94	0.63
Cr2O3	0.18	0.35	0.20	0.27	0.57	0.15	0.51	0.54	0.01	0.41	0.24	0.27	0.60	0.29	0.33
FeO	5.84	4.72	4.81	3.97	4.35	4.65	3.79	3.44	4.53	5.58	5.57	5.10	4.73	4.86	5.10
MnO	0.13	0.10	0.11	0.12	0.12	0.08	0.07	0.08	0.09	0.17	0.10	0.07	0.14	0.11	0.19
MgO	32.60	34.77	36.32	37.04	34.81	35.99	36.14	36.66	36.76	34.82	34.88	34.97	35.48	34.41	35.39
CaO	1.15	1.03	0.19	0.28	0.72	0.16	0.27	0.35	0.01	0.86	0.98	0.82	0.72	1.05	0.85
Na2O	0.33	0.26	0.04	0.15	0.24	0.03	0.07	0.16	0.09	0.15	0.32	0.15	0.29	0.26	0.12
Total	100.7	99.49	99.24	100.94	99.4	99.43	99.75	99.89	99.22	99.63	99.15	100.65	99.54	100.67	99.86
Atomic Proportions Based On Selected Number Of Oxygens															
Oxygens	6	6	6	6	6	6	6	6	6	6	6	6	6	6	6
Si	2.021	1.976	1.964	1.957	1.983	1.982	1.983	1.972	1.965	1.968	1.947	1.989	1.956	1.996	1.970
Ti	0.004	0.002	0.001	<LOD	0.003	<LOD	<LOD	<LOD	<LOD	<LOD	0.006	0.002	0.003	0.003	0.001
Al	0.042	0.038	0.028	0.051	0.035	0.027	0.033	0.034	0.029	0.031	0.040	0.032	0.035	0.038	0.026
Cr	0.005	0.010	0.005	0.007	0.016	0.004	0.014	0.015	0.000	0.011	0.007	0.007	0.016	0.008	0.009
Fe	0.166	0.136	0.139	0.112	0.126	0.134	0.108	0.098	0.130	0.162	0.162	0.145	0.137	0.138	0.147
Mn	0.004	0.003	0.003	0.003	0.004	0.002	0.002	0.002	0.003	0.005	0.003	0.002	0.004	0.003	0.006
Mg	1.657	1.788	1.870	1.868	1.791	1.845	1.840	1.864	1.889	1.797	1.812	1.776	1.828	1.746	1.818
Ca	0.042	0.038	0.007	0.010	0.027	0.006	0.010	0.013	0.000	0.032	0.037	0.030	0.027	0.038	0.031
Na	0.022	0.017	0.003	0.010	0.016	0.002	0.005	0.011	0.006	0.010	0.022	0.010	0.019	0.017	0.008
Sum	3.963	4.008	4.0204	4.019	3.998	4.0029	3.996	4.009	4.0232	4.016	4.035	3.994	4.026	3.987	4.016
Mg#	90.87	92.92	93.09	94.33	93.45	93.24	94.44	95.00	93.54	91.75	91.78	92.44	93.04	92.66	92.52
Ca#	2.47	2.08	0.38	0.54	1.46	0.32	0.53	0.68	0.02	1.74	1.98	1.66	1.44	2.15	1.70

[§] Analyses taken from Hops (1989)

Orthopyroxene Compositions - Matsoku

	LBM10	LBM16	LBM17	LBM30	LBM32	LBM36-2	LBM36-3	LBM3	LBM8	LBM9	LBM6	LBM22
SiO2	56.79	58.79	59.18	58.77	59.31	56.85	58.84	59.26	59.49	59.10	57.88	56.24
TiO2	0.06	0.12	<LOD	0.17	0.14	0.05	0.08	<LOD	<LOD	<LOD	0.07	0.18
Al2O3	0.76	0.88	0.78	0.84	0.87	0.70	0.79	0.73	0.82	0.84	0.69	0.81
Cr2O3	0.29	0.32	0.29	0.30	0.27	0.14	0.12	0.28	0.39	0.26	0.22	0.27
FeO	4.54	4.39	4.22	5.29	6.36	7.34	7.27	4.47	4.30	4.69	6.23	5.35
MnO	0.10	0.08	0.09	0.16	0.16	0.12	0.14	0.14	0.10	0.07	0.15	0.13
MgO	36.38	35.02	34.82	33.70	32.78	33.25	32.62	34.19	34.95	35.54	34.21	35.88
CaO	0.53	0.43	0.47	0.49	0.44	0.49	0.54	0.44	0.46	0.46	0.58	0.52
Na2O	<LOD	0.18	0.14	0.20	0.18	0.13	0.15	0.16	0.15	0.14	0.13	0.17
Total	99.59	100.22	100.01	99.94	100.51	99.08	100.54	99.7	100.67	101.13	100.17	99.55
						Atomic Proportions Based On Selected Number Of Oxygens						
Oxygens	6	6	6	6	6	6	6	6	6	6	6	6
Si	1.958	2.001	2.015	2.013	2.026	1.987	2.019	2.025	2.013	1.997	1.991	1.947
Ti	0.002	0.003	<LOD	0.004	0.004	0.001	0.002	<LOD	<LOD	<LOD	0.002	0.005
Al	0.031	0.035	0.031	0.034	0.035	0.029	0.032	0.029	0.033	0.033	0.028	0.033
Cr	0.008	0.009	0.008	0.008	0.007	0.004	0.003	0.008	0.010	0.007	0.006	0.007
Fe	0.131	0.125	0.120	0.152	0.182	0.215	0.209	0.128	0.122	0.132	0.179	0.155
Mn	0.003	0.002	0.003	0.005	0.005	0.004	0.004	0.004	0.003	0.002	0.004	0.004
Mg	1.870	1.777	1.767	1.721	1.669	1.733	1.668	1.741	1.763	1.790	1.754	1.852
Ca	0.020	0.016	0.017	0.018	0.016	0.018	0.020	0.016	0.017	0.017	0.021	0.019
Na	<LOD	0.012	0.009	0.013	0.012	0.009	0.010	0.011	0.010	0.009	0.009	0.011
Sum	4.021	3.980	3.970	3.968	3.955	4.000	3.967	3.962	3.970	3.988	3.995	4.034
Mg#	93.46	93.43	93.63	91.91	90.19	88.98	88.89	93.17	93.54	93.11	90.73	92.29
Ca#	1.04	0.87	0.96	1.03	0.96	1.05	1.18	0.92	0.94	0.92	1.20	1.03

Orthopyroxene Compositions - Matsoku

	JJH6	JJH7	JJH8	JJH9
SiO2	57.71	57.67	56.96	57.17
TiO2	<LOD	0.19	0.16	<LOD
Al2O3	0.54	1.12	0.89	0.59
Cr2O3	0.32	0.38	0.42	0.34
FeO	5.07	5.19	5.46	5.51
MnO	0.12	0.17	0.11	0.15
MgO	34.70	34.12	34.54	35.23
CaO	0.94	1.09	0.92	0.90
Na2O	0.01	0.42	0.32	0.05
Total	99.43	100.36	99.79	99.96
		Atomic Proportions Based On Selected Number Of Oxygens		
Oxygens	6	6	6	6
Si	1.992	1.977	1.968	1.970
Ti	<LOD	0.005	0.004	<LOD
Al	0.022	0.045	0.036	0.024
Cr	0.009	0.010	0.011	0.009
Fe	0.146	0.149	0.158	0.159
Mn	0.004	0.005	0.003	0.004
Mg	1.785	1.744	1.779	1.810
Ca	0.035	0.040	0.034	0.033
Na	0.001	0.028	0.021	0.003
Sum	3.993	4.004	4.015	4.014
Mg#	92.43	92.14	91.86	91.94
Ca#	1.91	2.24	1.88	1.80

Clinopyroxene Compositions - Jagersfontein Peridotites

	J117[5]	JJG1710	JJG1729	JJG1733	JJG864	JJI110	JJI128[5]	JJI132	JJI135	JJI17[5]	JJI18
SiO2	55.39	54.81	54.32	54.68	54.71	53.56	55.20	54.84	54.52	55.35	53.49
TiO2	0.28	0.09	0.25	<LOD	0.03	0.39	0.13	0.11	<LOD	0.44	0.26
Al2O3	2.79	1.92	2.74	1.80	2.74	2.43	1.91	1.91	1.00	2.82	2.17
Cr2O3	0.59	1.26	0.76	1.53	2.56	0.90	1.03	1.09	0.93	1.43	1.65
FeO	4.26	2.83	3.95	1.16	1.87	3.42	2.85	2.84	2.68	3.56	3.37
MnO	0.13	0.11	0.03	0.06	0.07	0.06	0.10	0.09	0.11	0.12	0.11
MgO	19.09	19.97	18.81	16.57	15.81	19.19	18.31	19.48	19.58	19.12	19.37
CaO	15.36	17.54	17.10	22.95	19.41	16.87	18.74	17.57	20.33	14.99	16.55
Na2O	1.77	1.56	2.22	1.21	2.61	2.07	1.34	1.56	0.76	2.31	2.09
K2O	<LOD	0.03	0.04	<LOD	<LOD	0.26	<LOD	0.05	0.04	<LOD	0.03
Total	99.67	100.11	100.22	99.96	99.84	99.14	99.62	99.53	99.96	100.15	99.1

Atomic Proportions Based On Selected Number Of Oxygens

Oxygens	6	6	6	6	6	6	6	6	6	6	6
Si	1.988	1.967	1.956	1.978	1.979	1.950	1.991	1.978	1.971	1.978	1.948
Ti	0.008	0.002	0.007	<LOD	0.001	0.011	0.004	0.003	<LOD	0.012	0.007
Al	0.118	0.081	0.116	0.077	0.117	0.104	0.081	0.081	0.043	0.119	0.093
Cr	0.017	0.036	0.022	0.044	0.073	0.026	0.029	0.031	0.027	0.040	0.048
Fe	0.128	0.085	0.119	0.035	0.057	0.104	0.086	0.086	0.081	0.106	0.103
Mn	0.004	0.003	0.001	0.002	0.002	0.002	0.003	0.003	0.003	0.004	0.003
Mg	1.022	1.068	1.010	0.894	0.852	1.041	0.985	1.047	1.055	1.018	1.052
Ca	0.591	0.674	0.660	0.889	0.752	0.658	0.724	0.679	0.787	0.574	0.646
Na	0.123	0.109	0.155	0.085	0.183	0.146	0.094	0.109	0.053	0.160	0.148
K	<LOD	0.001	0.002	<LOD	<LOD	0.012	<LOD	0.002	0.002	<LOD	0.001
Sum	3.998	4.027	4.047	4.004	4.017	4.054	3.997	4.019	4.022	4.011	4.049
Mg#	88.88	92.64	89.46	96.22	93.77	90.91	91.97	92.44	92.87	90.54	91.11
Ca#	36.64	38.69	39.51	49.88	46.87	38.72	42.38	39.33	42.73	36.04	38.04

[5] Analyses taken from Hops (1989)

Clinopyroxene Compositions - Matsoku

	LBM10	LBM16	LBM3	LBM30	LBM32	LBM36-2	LBM36-3	LBM6	LBM9
SiO2	54.98	55.47	55.36	55.69	55.35	55.53	54.81	54.47	55.83
TiO2	0.13	0.37	0.09	0.35	0.40	0.14	0.14	0.15	0.04
Al2O3	2.37	3.36	2.89	3.09	3.48	2.31	2.44	1.90	2.54
Cr2O3	1.80	2.38	2.25	1.80	1.99	0.78	0.77	1.00	1.59
FeO	2.21	2.45	2.29	2.82	3.31	3.58	3.64	3.02	2.29
MnO	0.06	0.11	0.04	0.10	0.10	0.13	0.14	0.09	0.11
MgO	17.02	16.23	16.25	16.47	15.78	16.71	16.13	17.83	17.49
CaO	18.50	16.90	18.60	17.79	17.26	19.01	19.26	19.96	19.13
Na2O	2.47	3.44	2.57	3.10	3.34	2.07	1.79	1.72	2.21
K2O	0.03	0.02	0.03	0.02	0.03	0.02	<LOD	<LOD	<LOD
Total	99.57	100.73	100.37	101.22	101.05	100.29	99.13	100.15	101.22

Atomic Proportions Based On Selected Number Of Oxygens

	LBM10	LBM16	LBM3	LBM30	LBM32	LBM36-2	LBM36-3	LBM6	LBM9
Oxygens	6	6	6	6	6	6	6	6	6
Si	1.987	1.980	1.986	1.982	1.978	1.999	1.998	1.969	1.984
Ti	0.004	0.010	0.002	0.009	0.011	0.004	0.004	0.004	0.001
Al	0.101	0.141	0.122	0.130	0.147	0.098	0.105	0.081	0.106
Cr	0.051	0.067	0.064	0.051	0.056	0.022	0.022	0.029	0.045
Fe	0.067	0.073	0.069	0.084	0.099	0.108	0.111	0.091	0.068
Mn	0.002	0.003	0.001	0.003	0.003	0.004	0.004	0.003	0.003
Mg	0.917	0.864	0.869	0.874	0.840	0.897	0.876	0.961	0.927
Ca	0.716	0.646	0.715	0.678	0.661	0.733	0.752	0.773	0.728
Na	0.173	0.238	0.179	0.214	0.231	0.144	0.126	0.121	0.152
K	0.001	0.001	0.001	0.001	0.001	0.001	<LOD	<LOD	<LOD
Sum	4.020	4.025	4.009	4.026	4.027	4.010	3.998	4.032	4.016
Mg#	93.21	92.19	92.67	91.24	89.47	89.27	88.76	91.32	93.16
Ca#	43.86	42.80	45.13	43.70	44.01	44.98	46.18	44.58	44.01

Appendix C.4

Trace element data for garnets determined by SIMS, including trace elements not used in this study

	JJH7		JJG1716		J117		JJG1757		JJH1		JJH8		JJG864		JJH35	
	PPM	RSD%	PPM	RSD%	PPM	RSD%	PPM	RSD%	PPM	RSD%	PPM	RSD%	PPM	RSD%	PPM	RSD%
Li	0.27	19.40	0.08	12.14	0.21	5.23	0.06	25.38	0.05	7.18	0.17	11.62	0.11	36.89	0.05	8.01
Be	0.40	8.96	0.45	10.06	0.58	8.05	0.58	7.09	0.45	6.10	0.34	8.26	1.08	3.99	0.90	7.43
Sc	101.17	1.07	90.60	0.77	65.71	1.21	107.74	0.87	98.34	0.60	148.59	1.22	96.64	1.36	133.69	0.88
Sr	1.40	11.93	1.06	12.26	1.23	13.92	1.30	13.46	1.02	13.35	1.70	9.72	0.82	24.49	0.82	14.53
Y	11.26	3.67	16.09	3.35	19.20	3.01	1.81	4.05	4.91	2.83	10.21	3.86	9.88	4.06	2.81	3.08
Zr	60.85	3.37	37.59	3.32	56.65	3.31	28.93	3.09	18.41	4.16	63.67	3.20	83.84	3.11	11.27	1.97
Nb	1.83	2.23	0.97	2.22	0.74	2.97	1.96	6.57	2.64	3.12	2.47	2.09	1.60	5.33	2.64	2.74
Ba	0.14	36.71	0.14	47.28	0.05	45.00	0.08	52.49	0.05	54.73	0.07	52.72	0.10	75.93	0.07	66.99
La	0.06	14.34	0.04	7.12	0.04	6.72	0.06	10.91	0.05	12.04	0.06	6.24	0.06	12.62	0.06	3.39
Ce	0.47	3.85	0.26	10.27	0.32	7.73	0.57	6.30	0.45	7.93	0.44	7.53	0.55	4.85	0.43	6.18
Nd	1.75	4.22	1.94	4.57	1.19	5.77	1.49	7.68	1.35	4.06	1.58	6.89	2.79	6.66	1.20	6.12
Sm	1.18	9.23	1.56	4.63	0.81	3.70	0.49	8.00	0.54	10.93	0.94	9.33	2.51	6.09	0.40	8.05
Eu	0.42	6.35	0.70	3.85	0.35	5.73	0.14	8.21	0.19	4.76	0.39	6.48	0.99	7.40	0.11	5.85
Gd	1.41	4.76	1.92	7.33	1.34	5.49	0.50	6.10	0.57	8.27	1.22	7.29	2.49	5.92	0.38	4.99
Dy	1.93	5.78	2.71	4.07	2.85	7.34	0.35	7.35	0.73	7.86	1.78	5.60	2.75	4.98	0.40	3.81
Er	1.20	4.30	1.62	6.09	2.18	6.89	0.15	13.42	0.53	7.61	1.00	5.36	0.71	5.80	0.33	9.38
Yb	1.30	5.59	1.72	6.24	2.20	5.30	0.22	6.37	0.68	5.24	1.11	6.18	0.80	2.69	0.52	4.74
Hf			0.76	4.45	1.44	4.18	0.44	11.78	0.36	7.79	1.37	8.29	1.21	5.74	0.23	10.24

	LBM36-3		LBM36-2		LBM9		LBM8		LBM32		LBM16		LBM10		LBM17	
	PPM	RSD%	PPM	RSD%	PPM	RSD%	PPM	RSD%	PPM	RSD%	PPM	RSD%	PPM	RSD%	PPM	RSD%
Li	0.12	8.50	0.15	6.69	0.09	20.16	0.16	36.35	0.18	9.12	0.18	3.52	0.11	25.11	0.04	14.66
Be	0.60	7.92	0.80	2.51	0.83	5.36	0.70	12.36	0.65	16.92	1.12	8.25	0.93	4.20	0.83	3.14
Sc	126.36	1.31	136.63	0.91	97.18	0.51	108.83	0.99	113.59	1.27	119.04	0.56	94.32	1.22	73.75	0.71
Sr	0.89	25.95	1.09	18.26	1.21	19.48	1.44	15.79	1.42	17.43	0.85	19.30	0.89	15.75	0.81	14.92
Y	22.58	4.80	18.27	4.18	11.96	2.44	18.06	4.65	30.57	1.48	29.33	3.00	9.20	4.69	2.29	3.50
Zr	83.36	4.28	70.23	3.89	101.61	3.09	135.33	3.99	112.81	1.96	154.29	2.67	9.14	4.16	59.63	2.14
Nb	0.77	3.59	0.86	7.24	1.89	3.80	2.55	3.28	1.88	3.39	1.35	5.32	1.50	4.24	1.17	3.84
Ba	0.14	62.88	0.16	42.66	0.09	58.34	0.14	50.39	0.13	59.75	0.25	63.37	0.08	52.41	0.06	50.59
La	0.02	23.97	0.03	14.25	0.04	8.16	0.05	14.16	0.02	26.16	0.02	11.35	0.04	5.92	0.04	10.78
Ce	0.23	6.86	0.21	7.83	0.40	2.02	0.45	5.07	0.24	5.91	0.20	2.12	0.36	6.64	0.51	6.29
Nd	1.40	5.86	1.47	3.15	2.34	5.60	2.78	5.17	1.77	4.76	1.47	5.67	2.34	4.26	2.61	4.67
Sm	1.20	8.87	1.13	3.55	1.70	3.28	2.16	8.40	1.54	4.88	1.38	3.32	1.70	9.60	1.37	6.26
Eu	0.54	8.97	0.48	4.13	0.69	1.54	0.91	4.74	0.69	5.09	0.66	3.78	0.61	6.42	0.46	5.10
Gd	1.84	5.48	1.52	3.93	2.00	4.88	2.65	4.56	2.32	4.48	2.29	3.48	1.68	5.59	1.17	4.37
Dy	3.62	6.22	2.74	6.34	2.56	4.86	3.64	5.99	4.84	3.78	4.78	3.54	1.96	5.64	0.73	5.74
Er	2.57	7.22	2.04	6.27	1.07	5.70	1.69	6.53	3.14	3.42	2.94	4.55	0.73	5.57	0.16	10.78
Yb	2.88	7.16	2.31	3.17	1.16	7.42	1.53	7.27	2.98	2.89	2.71	3.69	0.67	7.24	0.30	2.64
Hf	1.47	5.49	1.25	5.06	1.36	4.41	2.05	3.69	2.53	2.35	2.63	3.93	1.28	7.98	0.60	5.73

RSD = Relative standard deviation